UNIVERSITY OF BELGRADE
SCHOOL OF ELECTRICAL ENGINEERING

Milana S. Lalović

RADIATION EFFECTS IN SILICON PHOTONICS OPTICAL LINKS

Doctoral Dissertation

Belgrade, 2024

UNIVERZITET U BEOGRADU

ELEKTROTEHNIČKI FAKULTET

Milana S. Lalović

UTICAJI ZRAČENJA NA OPTIČKE LINKOVE REALIZOVANE U SILICIJUMSKOJ FOTONICI

doktorska disertacija

Beograd, 2024

Mentor:

dr Peđa Mihailović, redovni profesor
Univerzitet u Beogradu, Elektrotehnički fakultet

Članovi komisije:

dr Slobodan Petričevič, redovni profesor
Univerzitet u Beogradu, Elektrotehnički fakultet

dr Miloš Vujisić, vanredni profesor
Univerzitet u Beogradu, Elektrotehnički fakultet

dr Nebojša Romčević, naučni savetnik
Univerzitet u Beogradu, Institut za fiziku

dr Jasna Crnjanski, vanredni profesor
Univerzitet u Beogradu, Elektrotehnički fakultet

dr Marko Krstić, vanredni profesor
Univerzitet u Beogradu, Elektrotehnički fakultet

Datum odbrane: _____

Acknowledgements

First and foremost, I express my sincere gratitude to my supervisor, Dr Peđa Mihailović, for leading me through my PhD journey, for introducing me to CERN and presenting me the opportunity to apply for the Doctoral Student programme there.

I would like to thank the Opto team of the EP-ESE-BE section at CERN led by Dr Jan Troska and all present and past team members for all the coffee breaks and discussions during my years at CERN. A special acknowledgement goes to Dr Carmelo Scarcella for his invaluable assistance during my first days in the team and for all the discussions during the many irradiation tests we did together.

To Ana and Teodora, who have been true companions since our first day at University, I am deeply grateful for their unselfish friendship and support. Special thanks go to my best friend, Petar, for all the projects we did together during our Bachelor's and Master's studies and with whom I shared all the PhD student problems.

I would like to thank my small group of friends at CERN, Peđa, Amar, Nikolina, and Ivan, who were there for many trips we did together and for all the birthdays and other occasions that we celebrated with each other. You were there to make my life a little bit easier in the most challenging moments.

Želim da se zahvalim svojoj porodici, mami, tati i Marku, na svoj prodršci i ljubavi koje su mi pružili, što su bili uz mene svih ovih 10 godina studiranja i što su vjerovali da ću jednog dana završiti.

Last but certainly not least, my greatest gratitude goes to Miloš, for his love and presence by my side through every single step. You have been my rock, walking hand in hand through every joy, every tear, every triumph, and every failure over the past four years – and hopefully, countless more lie ahead. *Još malo i uspjeli smo.*

Doctoral dissertation title: Radiation effects in silicon photonics optical links

Abstract

The optical links currently installed in CERN's detectors will not be able to support the radiation levels as well as the amount of data expected with the next upgrades of the Large Hadron Collider, specifically during the high luminosity phase. During this phase, it is expected that the luminosity levels will increase five to seven times compared to the current ones. This will increase the number of collisions and, consequently, the amount of data needed to be transmitted and processed. Therefore, it is necessary to find alternative solutions for current optical links that can transmit data at a speed of 10 Gb/s and are resistant to 1 MGy of total ionising dose and neutron fluence of 1×10^{15} n/cm^2. Silicon photonics stands out as a technology that currently promises improvements in data transmission capacity, with speeds of 50 Gb/s per wavelength.

The goal of this thesis is an experimental examination of the radiation hardness of various silicon photonic components, including Mach-Zehnder and ring modulators, as well as waveguides and germanium photodiode, to radiation levels predicted for the high-luminosity phase. For the first time, ring modulators were tested to study the ionisation effects of X-rays and non-ionising effects of neutrons of ultra-high doses, 11 MGy and 3×10^{16} n/cm^2, respectively. The effects of different geometric parameters of the modulator as well as of the doping concentration on radiation hardness, were analysed. Design optimisation of the ring modulator for maximum radiation hardness is proposed based on the obtained results. Comparative analysis has shown the superiority of ring modulators compared to Mach-Zehnder modulators, where the operating temperature is highlighted as a key factor due to the thermal annealing effect. Additionally, the influence of radiation on waveguides and photodiodes is shown to be minimal, regardless of the type of radiation.

Keywords: high-energy physics, CERN, silicon photonic, Mach-Zehnder modulators, ring modulators, ionising radiation damage, non-ionising radiation damage

Scientific field: Physical Electronics

Scientific subfield: Nanoelectronics and Photonics

Naziv doktorske disertacije: Uticaji zračenja na optičke linkove realizovane u silicijumskoj fotonici

Sažetak

Optički linkovi koji su trenutno instalirani u CERN-ovim detektorima neće moći da podrže nivoe zračenja kao ni količine podataka koje se očekuju unapređenjem Velikog Hadronskog Sudarača, tačnije prilikom faze visoke luminoznosti. U toku ove faze se očekuje da nivoi luminoznosti porastu pet do sedam puta u odnosu na trenutne, što sa sobom donosi prenos i obradu veće količine podataka koje će biti proizvedene usled većeg broja sudara. Stoga, potrebno je da se nađu alternativna rešenja za trenutno optičke linkove koji mogu da prenesu podatke brzinom od 10 Gb/s i otporni su na 1 MGy of totalne jonizujuće doze i fluks neutrona od 1×10^{15} n/cm^2. Silicijumska fotonika se ističe kao oblast optike koja trenutno obećava napredak u pogledu kapaciteta prenosa podataka, sa brzinama od 50 Gb/s po talasnoj dužini.

Cilj ove teze je eksperimentalno ispitivanje otpornosti različitih optičkih komponenti, uključujući Mach-Zehnder i prstenaste modulatore, kao i germanijumske fotodiode i talasovode, na predviđene nivoe zračenja tokom faze visoke luminoznosti. Po prvi put su testirani prstenasti modulatori na uticaje jonizujućih efekata X-zraka i nejonizujućih efekata neutrona ultra visokih doza, 11 MGy i 3×10^{16} n/cm^2, respektivno. Analizirani su uticaji različitih geometrijskih parametara modulatora kao i koncentracije dopiranosti na otpornost na zračenje. Na osnovu dobijenih rezultata predložena je optimizacija dizajna prstenastog modulatora za maksimalnu otpornost na zračenje. Uporedna analiza je pokazala superiornost prstenastih modulatora u poređenju sa Mach-Zehnder modulatorima, pri čemu se kao ključni faktor ističe temperatura radnog okruženja zbog efekta termalnog oporavka. Takođe, pokazano je da je uticaj zračenja na fotodiode i talasovode minimalan, bez obzira na vrstu zračenja.

Ključne reči: fizika visokih energrija, CERN, silicijumska fotonika, Mach-Zehnder modulatori, prstenasti modulatori, oštećenje usled jonizujućeg zračenja, oštećenje usled nejonizujućeg zračenja

Naučna oblast: Fizička elektronika

Uža naučna oblast: Nanoelektronika i Fotonika

Contents

List of Figures

List of Tables

List of Abbreviations

ALICE A Large Ion Collider Experiment

ASIC Application-Specific Integrated Circuits

ATLAS A Toroidal LHC ApparatuS

BE Back-End

BOX Buried Oxide

CERN European Organisation for Nuclear Research

CMOS Complementary Metal-Oxide-Semiconductor

CMS Compact Muon Solenoid

COTS Commercial Off-The-Shelf

CRC Cyclotron Resource Center

DAQ Data Acquisition

DUT Device Under Test

ECAL Electromagnetic Calorimeter

EEL Edge-Emitting Laser

e-h electron-hole

ER Extinction Ratio

ESE Electronics Systems for Experiments

FPGA Field-Programmable Gate Arrays

FSR Free Spectral Range

FWHM Full-Width at Half-Maximum

GBT GigaBit Transceiver

GBTIA GigaBit Transimpedance Amplifier

Ge Germanium

HBD Hardening By Design

HCAL Hadron Calorimeter

HEP High Energy Physics

HL-LHC High Luminosity LHC

HLT High-Level Trigger

I2C Inter-Integrated Circuit

IC Integrated Circuit

IL Insertion Loss

L1T Level-1 Trigger

LDD Laser Diode Drivers

LHC Large Hadron Collider

LHCb Large Hadron Collider beauty

LIDAR Light Detection and Ranging

LINAC4 LINear ACcelerator 4

lpGBT low-power GigaBit Transceiver

LPIN Lateral p-i-n

LS Long Shutdown

LS2 Long Shutdown 2

MOSFET Metal-Oxide-Semiconductor Field- Effect Transistor

MPW Multi-Project Wafer

MTD Minimum-ionising-particle precision Timing Detector

MZI Mach-Zehnder interferometer

MZM Mach-Zehnder Modulator

NIEL Non-Ionising Energy Loss

NIF Neutron Irradiation Facility

OMA Optical Modulation Amplitude

OPM Optical Power Meter

OSA Optical Spectrum Analyser

OSETs Optical Single-Event Transients

PCB Printed Circuit Board

PD Photodiode

PIC Photonic Integrated Circuit/Chip

PKA Primary Knock-on Atom

PS Proton Synchrotron

PSB Proton Synchrotron Booster

RF Radio-Frequency

RM Ring Modulator

Rx Receiver

SEE Single Event Effects

Si Silicon

SiPh Silicon photonics

SLED Superluminescent diode

SM Single-Mode

SOI Silicon-on-Insulator

SPS Super Proton Synchrotron

TE Transversal Electric

TID Total Ionising Dose

TM Transversal Magnetic

TRx Transceiver

TTC Trigger, Timing and Control

Tx Transmitter

VCSEL Vertical-Cavity Surface Emitting Lasers

VL Versatile Link

VL$^+$ Versatile Link PLUS

VPIN Vertical p-i-n

VTRx Versatile Transceiver

WDM Wavelength Division Multiplexing

YETS Year-End Technical Stop

Chapter 1

Introduction

The European Organisation for Nuclear Research (CERN - *Conseil Européen pour la Recherche Nucléaire*) [1] is the biggest High Energy Physics (HEP) laboratory in Europe, located on the Swiss-French border near Geneva, Switzerland. The world's largest accelerator, the Large Hadron Collider (LHC) [2], [3] is located at CERN. It is a 26.7 km long ring of Radio-Frequency (RF) cavities that accelerate particle beams and superconducting electromagnets that focus and bend the trajectories of the beam. The superconducting electromagnets require being carefully cooled down to a temperature colder than outer space, 1.9 K, to keep the coils in the superconducting state. Inside the accelerator, two beams of particles (mainly protons or occasionally heavy ions) are propagating in opposite directions through two parallel pipes. The beam pipes cross at several points along the LHC, and at those cross-sections, collisions occur.

1.1 The LHC Experiments at CERN

Before the protons reach the LHC, they are created and pre-accelerated in the system of smaller linear and circular accelerators: the LINear ACcelerator 4 (LINAC 4) [4], the Proton Synchrotron Booster (PSB) [5], the Proton Synchrotron (PS) [6] and the Super Proton Synchrotron (SPS) [7] as schematically displayed in Figure 1.1. The negative hydrogen ions are initially produced from a hydrogen gas source and accelerated to 160 MeV in LINAC 4, and afterwards prepared for injection into the PSB. During injection, the ions are stripped of the two electrons and only protons are left, which are further accelerated to 2 GeV for injection into the PS. The PS is used to accelerate protons to an energy of 26 GeV, while the SPS is used to further accelerate the protons to an energy of 450 GeV. This pre-acceleration process takes place over a period of several hours, during which the protons are accelerated and focused into a tight beam using electric and magnetic fields. Afterwards, they are injected into the LHC where they are further accelerated to very high energies, up to 6.5 TeV per beam, and then made to collide at the interaction points, called Experiments. At LHC, there are four major experiments: ALICE (A Large Ion Collider Experiment), ATLAS (A Toroidal LHC ApparatuS), CMS (Compact Muon Solenoid) and LHCb (Large Hadron Collider beauty). The biggest ones, CMS and ATLAS, use general-purpose detectors which made a simultaneous discovery of the Higgs boson in 2012 [8] [9]. ALICE and LHCb are specialised detectors focused on heavy-ion physics and the slight differences between matter and antimatter, respectively.

The working principle of the LHC detectors will be explained on the example of the CMS detector. In Figure 1.2a, the 3D model of the CMS detector is shown. With the frequency of 40 MHz (every 25 ns), two bunches of protons collide in the centre of the detector (centre of the Figure 1.2a).

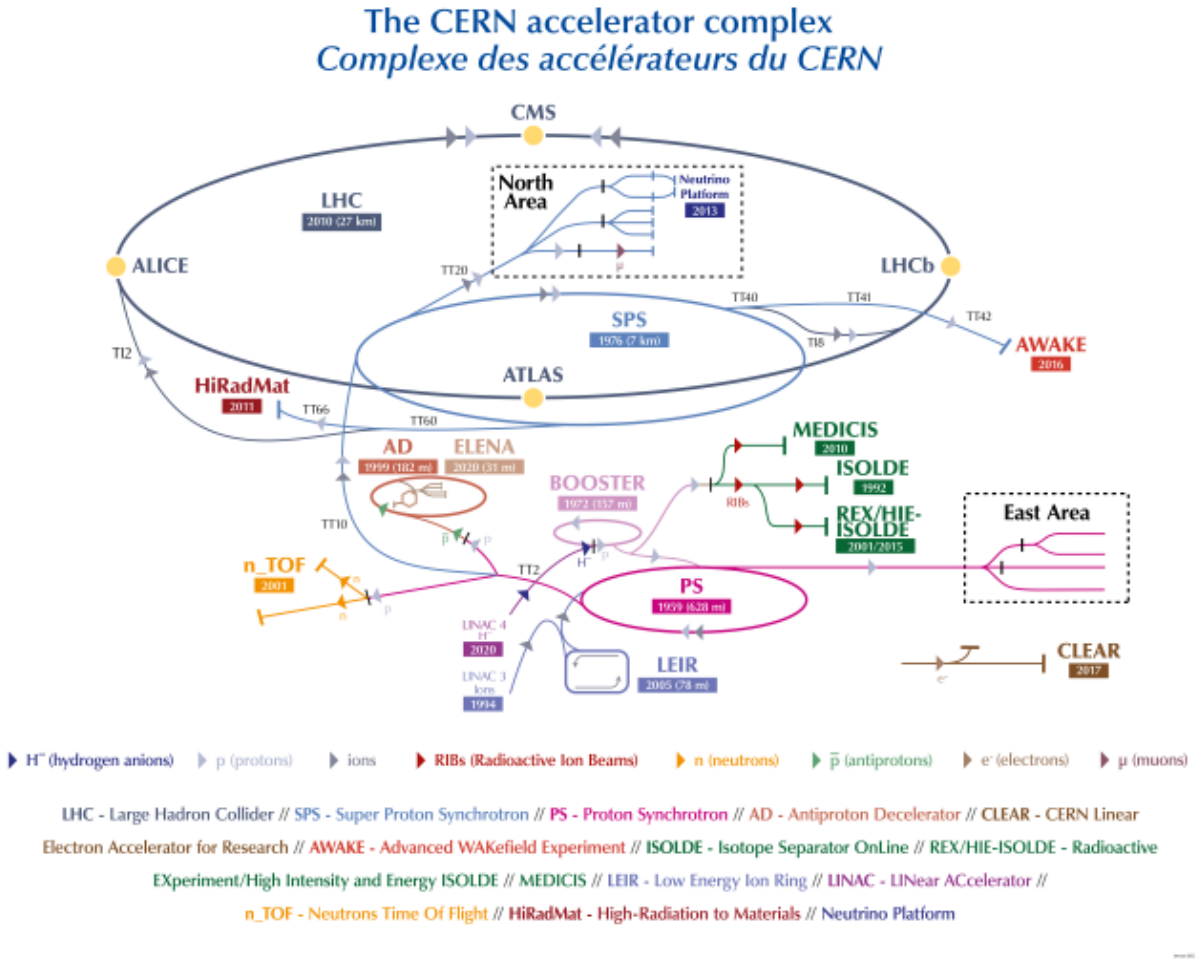

Figure 1.1: The CERN accelerator complex includes the chain of accelerators that sends protons into the LHC ring with the collision points at the four experiments: ALICE, ATLAS, CMS, and LHCb [10].

Approximately 100 billion protons are squeezed into one bunch, down to 64 μm in the beam's cross-section at the interaction point. When two bunches interact, most protons miss each other, and only around 20 collisions happen per crossing [11]. Since the bunches interact every 25 ns, there are approximately 800 million collisions per second, which produce a vast amount of data to be acquired and processed. Figure 1.2b shows a transverse slice of the CMS detector from the collision point to the outer layers. Listed from the collision point, the sub-detectors are in the following order: the Silicon Tracker, the Electromagnetic Calorimeter (ECAL), the Hadron Calorimeter (HCAL), and the Muon Chambers. The Superconducting Solenoid is located between the HCAL and the muon chambers. The solenoid allows measurement of the momentum of the charged particles, with its nominal magnetic field of 4 T. The red outer part of the detector is the iron return yoke, which is necessary for confining the magnetic field. The other important role of the return yoke is that it acts as a muon filter and it stops all other particles.

The first sub-detector in the CMS experiment, closest to the interaction point and beam pipe, is the Silicon Tracker. It consists of multiple layers of concentric silicon sensors, which accurately determine the trajectory of charged particles while leaving neutral particles undetected. The pixel detectors occupy the innermost portion of the tracker, located within 15 cm of the beam pipe, while the remaining volume of the tracker is populated by silicon microstrip modules. Subsequently, the ECAL measures the energy, position and timing of incoming electromagnetic particles, such as elec-

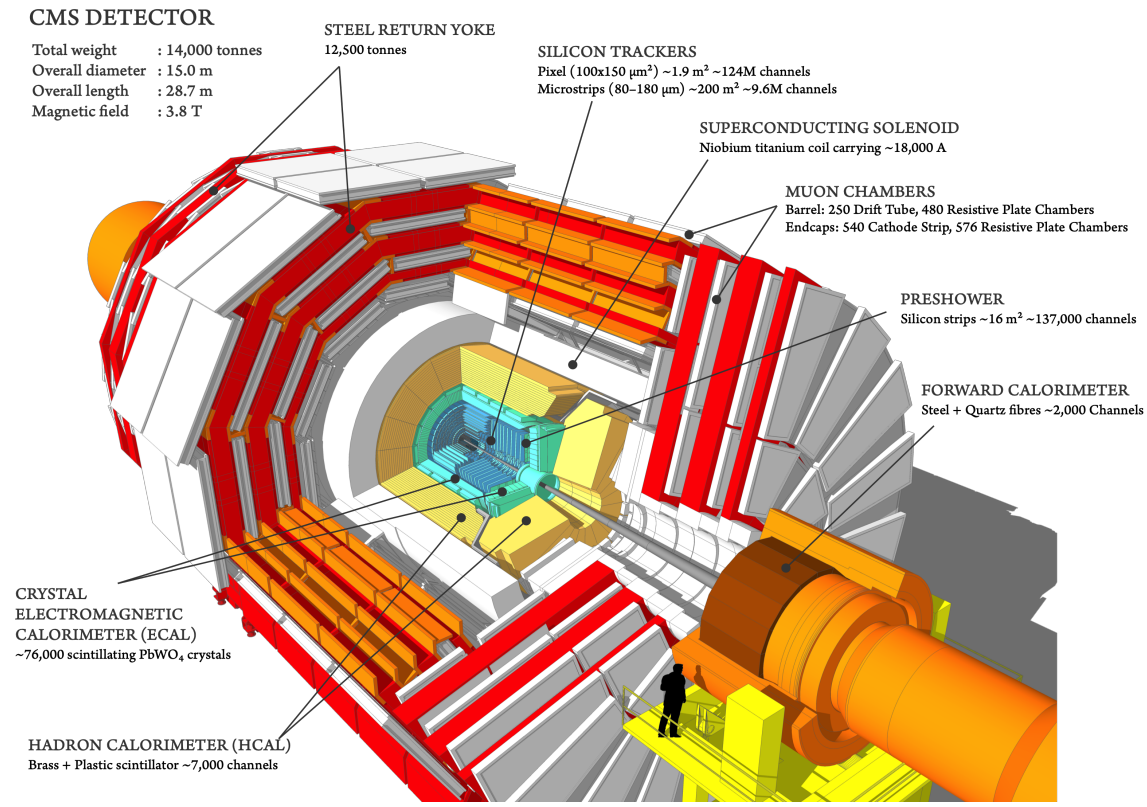

(a)

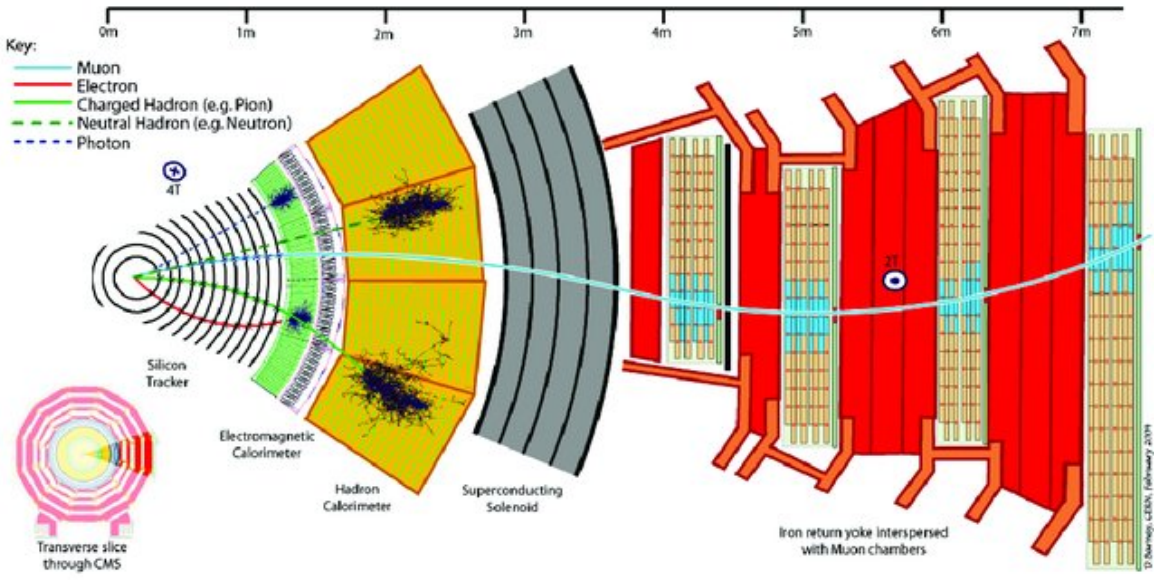

(b)

Figure 1.2: (a) 3D model of CMS detector [12]. (b) A transverse slice of the CMS detector showing how different particles interact with different sub-detectors [13].

trons, positrons, and photons. Following the ECAL is the HCAL, which is responsible for measuring the energy, position and timing of hadrons. Finally, the muon chambers system, positioned after the semiconductor magnet, detects and characterises muons. Particles such as neutrinos are not detectable in any sub-detector, but their presence can be indirectly observed in the form of missing energy.

Across all CMS sub-detectors, there are approximately 75 million sensors [11]. These sensors generate around 1 MB of data for every bunch-crossing [11]. Given the overwhelming volume of data produced, it is infeasible to collect data from all events. Moreover, many of these interactions may not yield meaningful discoveries. Hence, it is necessary to employ a "trigger" mechanism to identify events that hold the greatest potential for scientific significance. The trigger system of CMS consists of two levels: a hardware Level-1 Trigger (L1T) and a software trigger High-Level Trigger (HLT). The first one acquires information measured by ECAL, HCAL and muon chambers. The L1T then combines this data and determines whether or not to keep the event. The L1T reduces the incoming average data rate to a maximum of 100 kHz [11]. If the event is flagged as interesting, data of this event from all sub-detectors is sent to the HLT to be selected further (data rates lowered to 100 Hz [14]), after which they are saved in permanent storage and analysed.

1.2 Optical links in HEP Experiments

The utilisation of optical data transmission plays a crucial role within the LHC. The approach of using optical data transmission over classical copper cables is adopted to reduce the material budget and facilitate the transfer of data at high speeds. For example, the loss over copper cable for a data rate of 10 Gb/s is 0.2 dB/cm [15], while for the single-mode optical fibre at 1550 nm is 0.2 dB/km [16]. The bandwidth provided by fibre optic systems is generally able to support the high demands of LHC applications. The optical fibre links are employed for data acquisition (DAQ), trigger, timing and control (TTC) signals and slow control signals. Previously, separate optical links were required for each type of signal due to the different target applications and technological constraints. However, with the advancement of optoelectronic and CMOS technologies, a general-purpose optical link that can handle all transmission applications is now feasible.

The Versatile Link (VL) project [17], [18] is developed at CERN for the LHC experiments, and it was integrated into the experiments during the Long Shutdown 2 (LS2) period from 2019 to 2022. It is a bi-directional link, where the information is sent in two directions, from the counting room to the detector and vice versa. The counting room is located approximately 100 m away from the detector. Two versions of devices exist that operate on 850 nm and 1310 nm wavelengths, as a multi-mode or a single-mode version, respectively. The VL data transmission rates go up to 5 Gb/s. The Versatile Link scheme is shown in Figure 1.3, and it consists of three parts: the front-end (on-detector) Versatile Transceiver (VTRx), passive optical components (optical fibres and connectors) and back-end (off-detector) components. The VTRx is a radiation-hard module which can withstand a Total Ionising Dose (TID) of 10 kGy and the 20 MeV-equivalent neutron fluence of 5×10^{14} n/cm^2 [19] and a strong magnetic field of 4 T [20].

The transmitter part of the VTRx consists of a laser driver and a laser diode for the electro-optic conversion. The VTRx has two options for the laser diode: the Edge-Emitting Laser (EEL) for the 1310 nm version and the Vertical-Cavity Surface Emitting Lasers (VCSELs) for the 850 nm version [21]. The receiver part is a photodiode and a GigaBit Transimpedance Amplifier (GBTIA) for performing the conversion of the optical signal back to an electrical one. A set of passive components (the optical fibre and connectors) connect the VTRx to the off-detector electronics

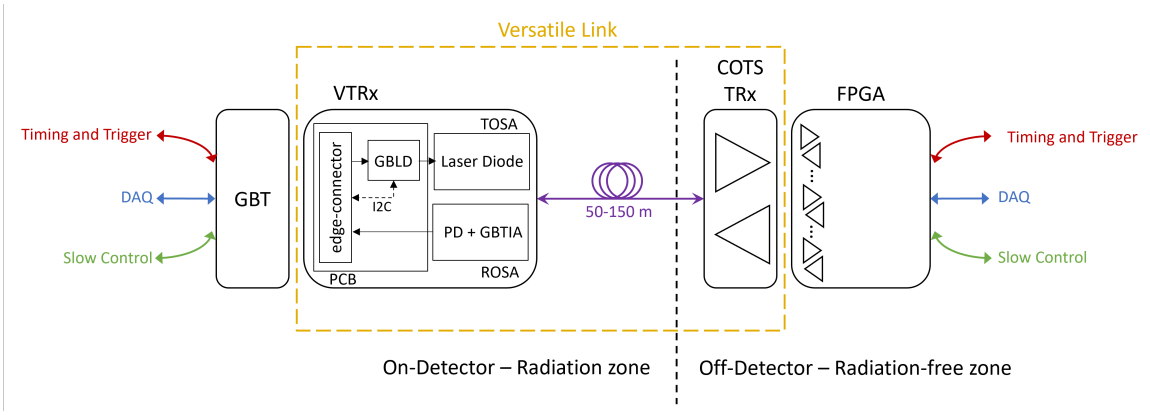

Figure 1.3: Versatile Optical Link Scheme (after [18]).

where Commercial Off-The-Shelf (COTS) optical transceivers (TRx) will provide the data to Field-Programmable Gate Arrays (FPGAs) - uplink. Similarly, data is sent from FPGAa, over COTS TRx to on-detector components - downlink. On the other side of VTRx, there is GigaBit Transceiver (GBT) [22] for increasing the bandwidth available for data transmission between the front-end and the back-end. GBT architecture provides support for the transmission of three types of data: Timing Trigger and Control, Data Acquisition, and Slow Control signals.

1.3 The High Luminosity LHC upgrade

Luminosity is a crucial measure to determine the amount of particle collisions in a particle accelerator. Instantaneous luminosity is a measure of the number of particle collisions per unit of time and unit of cross-sectional area, and it is expressed in $\mathrm{cm}^{-2}\mathrm{s}^{-1}$, while the integrated luminosity is the cumulative measure of the total number of collisions over a period of time and it is expressed in fb^{-1} [1]. The nominal luminosity in LHC is $10^{34}\,\mathrm{cm}^{-2}\mathrm{s}^{-1}$. The High Luminosity LHC (HL-LHC) is an upgrade of the LHC where much higher instantaneous luminosity levels will be achieved compared to nominal levels during the LHC phase. After the extensive upgrades of its components, the LHC will result in a significant increase of its instantaneous luminosity up to $5 \times 10^{34}\,\mathrm{cm}^{-2}\mathrm{s}^{-1}$. In the peak configuration, the maximum luminosity expected to be $7.5 \times 10^{34}\,\mathrm{cm}^{-2}\mathrm{s}^{-1}$ raising the average number of proton-proton collisions per bunch-crossing to approximately 200 and the integrated luminosity to $450\,\mathrm{fb}^{-1}$ per year. The HL-LHC is planned to commence after the third Long Shutdown (LS3), from 2029 (see Figure 1.4).

To maintain its performance, the CMS detector underwent an initial series of upgrades in the period from LS1 through LS2, also known as the CMS Phase-I Upgrade [24]–[27]. By 2025, the quadrupoles that focus the beams at the ATLAS and CMS collision regions are expected to be close to the end of their lives due to radiation exposure [28], therefore, there will be another long shutdown, LS3 or Phase-II Upgrade. During this upgrade, the entire silicon tracking system, presently consisting of pixel and strip detectors, will be replaced [29], as well as electromagnetic and hadronic endcap calorimeters [30]. A new minimum-ionising-particle precision timing detector (MTD) [31] and a new luminosity detector will be installed [32]. During LS4, no upgrade of the CMS is scheduled; nevertheless, ALICE and LHCb detectors will be upgraded [33]. The next and last upgrade of the LHC, LS5, will include further replacements necessary for the satisfactory operation of the CMS.

[1] $1\,\mathrm{fb}^{-1} = 10^{39}\,\mathrm{cm}^{-2}$

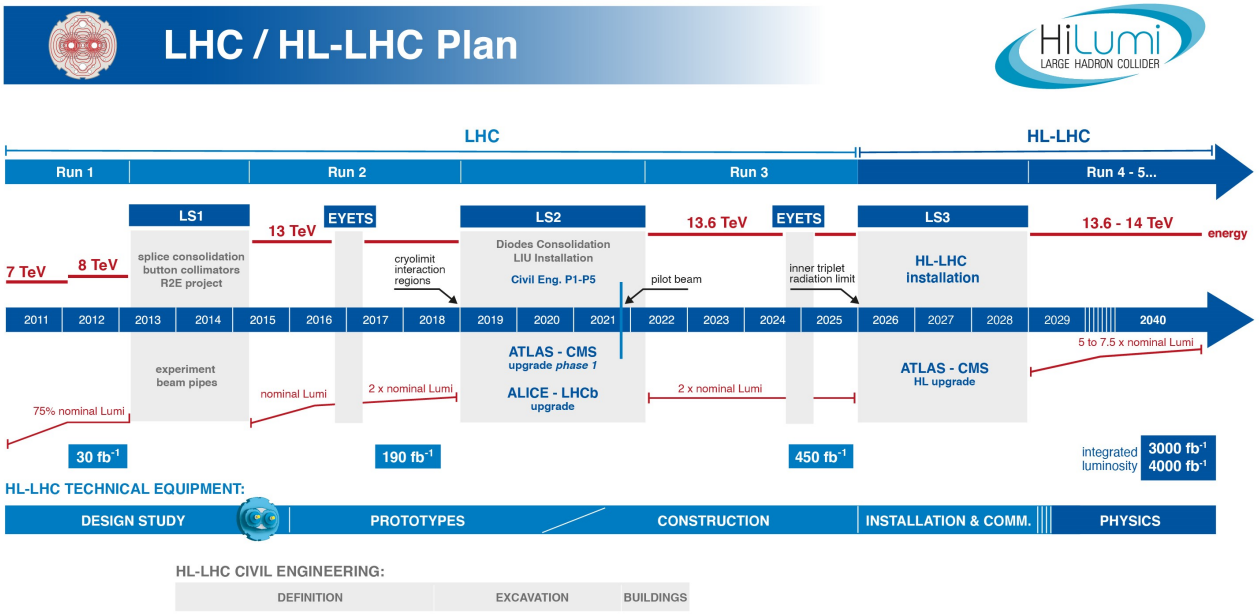

Figure 1.4: LHC and High Luminosity LHC schedule until 2041 [23].

1.3.1 The radiation environment in the HL-LHC

The main concern of the initial design of the CMS was to maintain the detector's performance in harsh environmental conditions, such as a high magnetic field, a wide range of temperatures or a high radiation dose. Given that the yearly dose delivered to the detector during the HL-LHC era will be proportional to the accumulated dose of all LHC operations prior to the start of the LS3, the significance of the issue is evident. The primary source of radiation are the proton-proton collisions, from which various other particles originates. The charged particles cause ionisation as they traverse through the detectors.

The distributions of the radiation levels in CMS simulated with the FLUKA Monte Carlo code [34], [35] are presented in Figure 1.5. Figure 1.5a shows the longitudinal cross-section of the CMS with the simulation of the TID across the different parts of the detector for the 7 TeV protons collisions after 3000 fb^{-1} of integrated luminosity after 10 years of operation. The maximum dose is expected closest to the collision point at (0,0), and decreases as the distance from the centre increases. In Figure 1.5b, the same estimation for the 1 MeV-equivalent neutron fluence is presented.

As it can be noticed from Figure 1.5, radiation levels vary from one sub-detector to another. The pixel part of the silicon tracker is the closest to the beam pipe and the collision point, thus, the strongest requirements are necessary for this part of the CMS. After the pixel tracker, the strip tracker and the endcap calorimeter are the most challenging. All devices that are placed in these sub-detectors need to endure TIDs of up to 10 MGy and fluences as high as 10^{16} particles/cm^2.

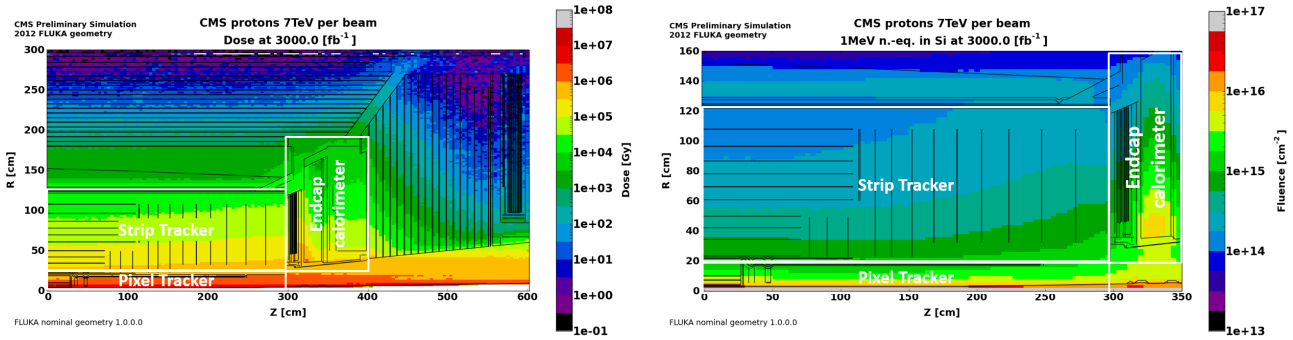

(a) **(b)**

Figure 1.5: (a) Monte Carlo estimation of the absorbed dose at CMS during proton-proton collisions with an energy of 7 TeV per beam after an integrated luminosity of 3000 fb^{-1} (b) Monte Carlo estimation of the 1 MeV-equivalent neutron fluence at CMS during proton-proton collisions with an energy of 7 TeV per beam after an integrated luminosity of 3000 fb^{-1}. R is the transverse distance from the beam pipe, and Z is the distance along the beam pipe from the interaction point at Z=0 [36].

1.3.2 Optical links for HL-LHC

Since the HL-LHC era will impose even more stringent demands on the optical links from the point of view of performance and radiation tolerance, an upgrade of Versatile Link was necessary. In addition to radiation levels, the amount of data produced in the experiments will increase by an order of magnitude, therefore, the link will need to operate on higher data rates. The Versatile Link PLUS project (VL^+) [37] targets the Phase-II upgrades of the CMS and ATLAS experiments, which will be conducted during LS3. During the expected lifetime, the on-detector components will have to withstand higher radiation levels compared to the levels that were required during the Phase-I upgrades. Particularly, they will need to endure 1 MGy of TID and neutron fluence of 1×10^{15} n/cm^2.

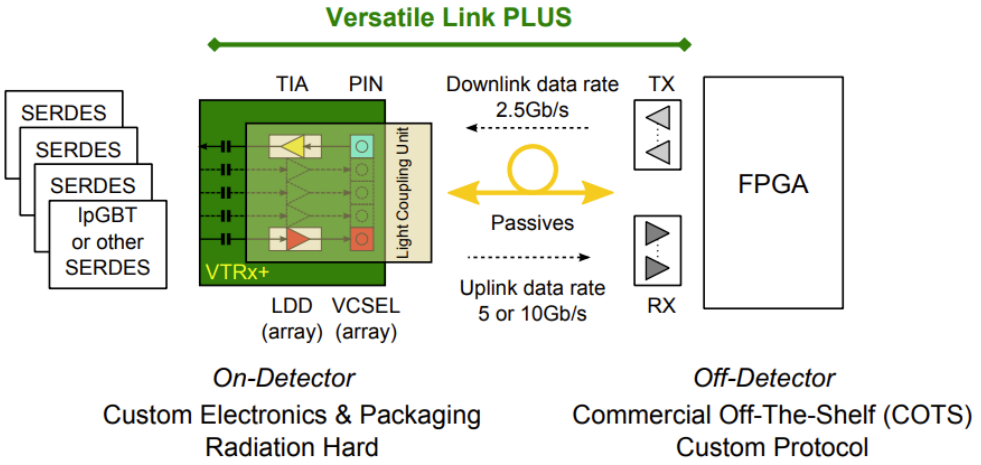

Figure 1.6: The Versatile Link PLUS architecture [38].

The architecture of the VL^+ is, in principle, similar to the VL. The major difference between the two is that the VL^+ has the multi-channel front-end module, the $VTRx^+$ module, which has an array of lasers (VCSELs) instead of just one laser diode [39]. The link is a bi-directional multimode link, operating on a central wavelength of 850 nm. There is a possibility of having different configurations

since it contains four transmitters (Tx) and one receiver (Rx). Depending on the experiment's needs, it can be used in the configuration with one to four transmitters, and with one or no receivers. For the manipulation of four laser diodes, there is an array of four laser diode drivers (LDD). The Rx channels operate at data rates of 5 Gb/s or 10 Gb/s in the uplink direction, for signals propagating from the front-end to the back-end. The Tx channels operate nominally at 2.5 Gb/s in the downlink direction. The VL+ is developed to operate together with the low-power GigaBit Transceiver (lpGBT) [40] or the other Serializer/Deserializer on the front-end side. In the back-end, all modules are commercial off-the-shelf devices compliant with 10 Gb/s standards. The operation of the Versatile Link PLUS is planned for the first part of the HL-LHC phase [41].

Silicon Photonics optical links

As the HL-LHC continues to operate, the integrated luminosity will consequently increase. This increased luminosity, however, presents a challenge for the components in the inner parts of the detectors, particularly the front-end elements of the optical links. These components are expected to degrade over time and may not be able to withstand the full duration of the HL-LHC program. As a result, alternative solutions for the optical transceiver must be investigated to ensure the durability and stability of the HL-LHC during its final run of operation (Run 6). Most detectors will still deploy optical links based on the VTRx+ that uses VCSELs and pin photodiodes. However, it has been determined that VCSEL-based links will not be suitable for use in the extreme radiation environment of the innermost parts of the detectors. The radiation levels in the CMS inner tracker during the Run 6 will be 10 MGy of total ionising dose and 1.6×10^{16} n(1 MeV)/cm^2 of neutron fluence [42].

High radiation levels are not the only difficulty of the new upgrades. Increased luminosity also brings a larger amount of data produced due to more collisions. The optical links will need to carry data from the detector to the counting room with data rates exceeding 10 Gb/s. The ability to multiplex more data on a single link would represent a significant advantage in terms of reducing the amount of required space and materials.

Given its established reliability and remarkable radiation hardness, silicon has been selected as the preferred material for particle detectors [43]–[45]. As a result, Silicon Photonics (SiPh) has been considered a viable replacement technology for optical links. Additional benefits of SiPh are lower costs due to the availability and affordability of silicon as a material [46], small size due to high-density integration [47], [48], and improved performance characterised by higher bandwidth, faster data rates, and lower power consumption [49]. Furthermore, its compatibility with Complementary Metal-Oxide-Semiconductor (CMOS) production processes [50], [51] makes it a highly attractive option for more compact and efficient systems.

Figure 1.7 shows the proposed concept of the optical link beyond the Phase-II upgrade. Specifically, this design is proposed for an upgrade that will be done during the Long Shutdown 5 (LS5). Similarly to the previously explained links, these links contain front-end (on-detector) components, back-end (off-detector) components and passive components (optical fibres and connectors) that connect the first two. In the front-end part, the data generated by the particle sensors will be concentrated in multi-Gb/s data streams using electronic aggregators, and afterwards, data is transformed into light using Silicon Photonics modulators integrated within a Photonic Integrated Circuit (PIC). SiPh modulators serve as on-detector transmitters, and the data is transmitted over an approximate distance of 100 meters through optical fibres to the back-end receivers. In the context of the downlink signal, a COTS transmitter in the off-detector section is connected via fibre to an integrated photodiode within the PIC, serving as an on-detector receiver. It is noteworthy that all

components in the front-end section will be custom-made and designed to withstand radiation, while the back-end transceivers will consist of commercially available off-the-shelf components.

Furthermore, a significant difference from the current optical links at CERN involves relocating the optical source (lasers) to the back-end. This move facilitates the use of commercial optical sources, eliminating the need for expensive radiation-hard components. A third optical fibre between the front-end and back-end will be required for such a design. However, the deployment of one more optical fibre per link does not result in increased bulkiness, given the feasibility of Wavelength Division Multiplexing (WDM) in SiPh modulators. The proposed optical link will utilise four distinct wavelengths for data transmission within the same fibre. Each wavelength will be capable of carrying 50 Gb/s of data, resulting in a 200 Gb/s uplink. The operational wavelength of either 1310 nm (O-band) or 1550 nm (C-band) will be possible based on the design specifications of modulators and photodiodes on the PIC, as well as the characteristics of the COTS lasers in the back-end.

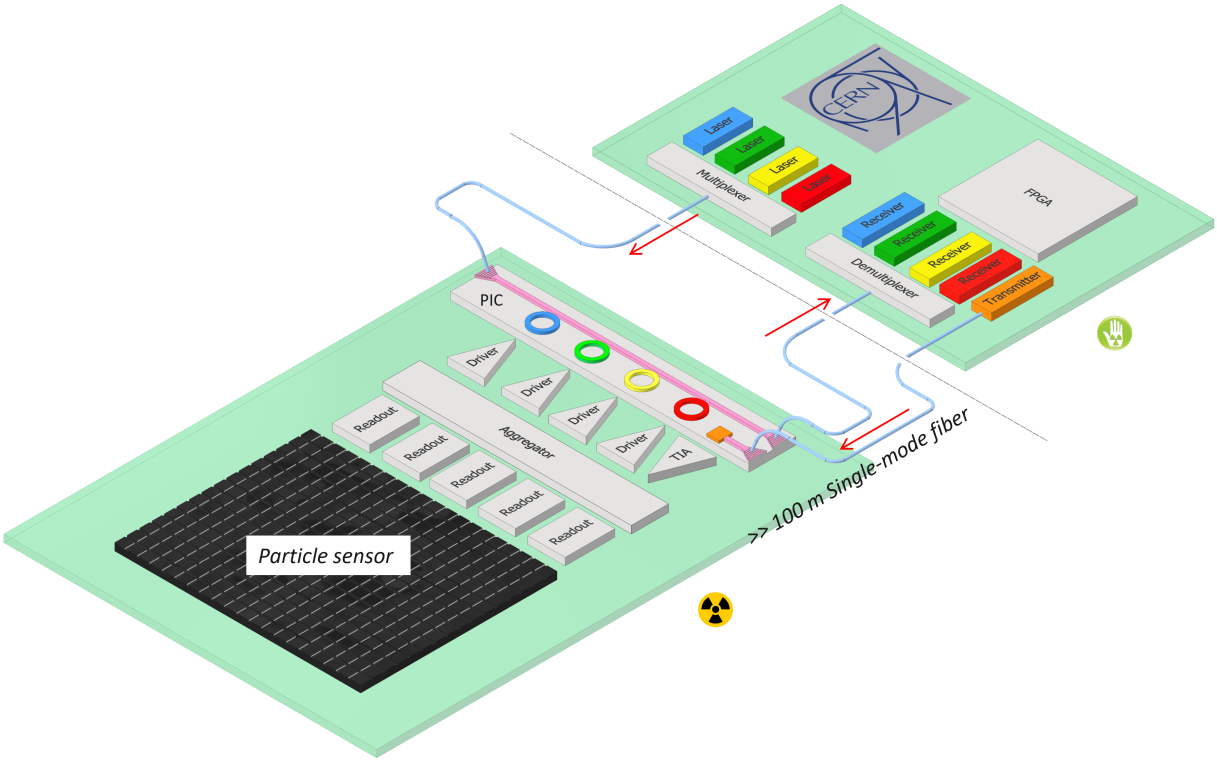

Figure 1.7: Silicon Photonics Optical Link Scheme planned for the later stage of HL-LHC [52].

1.4 Scope of the thesis

The focus of this thesis is the development of radiation-hard high-speed optoelectronic components based on Silicon Photonics for utilisation in data transmission in HL-LHC. In particular, this thesis concentrates on the radiation effects on these components, understanding those effects, and the proposal of the design for the more radiation-tolerant components.

This thesis is structured into six chapters with the following emphases.

In Chapter 1, LHC experiments at CERN are introduced, focusing on the CMS detector. The chapter explains the detector's operational principles, provides an overview of current optical links,

discusses the latest detector upgrade, and outlines radiation conditions. Additionally, it explains the motivation for selecting SiPh as the technology for new links.

Chapter 2 focuses on the fundamentals of Silicon Photonics, starting from Si waveguides and grating couplers, and extending to electro-optical effects in doped waveguides. It explains the basic principles of Mach-Zehnder and ring modulators, defining fundamental qualitative and quantitative characteristics. Two main types of Germanium (Ge) photodiodes are introduced, and their figures of merit are defined.

In Chapter 3, the fundamentals of the TID-induced degradation mechanisms in SiPh devices are explained while focusing on the generation and transport of charge in SiO_2. The creation of displacement damage associated with non-ionising radiation is studied and the non-ionising energy loss scaling hypothesis is discussed. The concept of the equivalent fluence and its calculation are defined.

In Chapter 4, the functionality of the Silicon Photonics chip is confirmed. The layout of the PICv2 is described and parameters of all devices relevant to the thesis are given. The characterisation of the ring modulators' micro-heaters is conducted and the initial pre-irradiation characterisations of SiPh modulators and photodiodes are presented.

The evaluation of the ionising radiation damage in SiPh devices is given in Chapter 5. Results from three separate X-ray tests are presented. The different setups and conditions used for each test are described. The results of the modulation efficiency measurements of the ring and Mach-Zehnder modulators with different design parameters as a function of TID are shown. The response of ring modulators to different operating temperatures while irradiated is presented. The annealing effect in SiPh ring modulators at different temperatures is investigated. The influence of different dose rates on modulation efficiencies is studied.

Results from the neutron irradiation tests on Ring Modulators and Mach-Zehnder Modulators as well as Ge photodiodes are presented in Chapter 6. The experimental setups and irradiation facility used in these tests are described. The modulation efficiencies as a function of neutron fluence at different operational temperatures of ring modulators are given, as well as the efficiencies for Mach-Zehnder modulators. The influence of neutron irradiation on dark currents and responsivities of Ge photodiodes is analysed.

Finally, Chapter 7 draws conclusions and offers an outlook on potential future work arising from this research.

Chapter 2

Silicon Photonics

Silicon photonics is a cutting-edge technology that uses a Silicon-on-Insulator (SOI) platform to facilitate the detection and manipulation of light. SOI is also a widely adopted and studied substrate in the electronic industry [53], [54]. The first proposal and preliminary demonstration of SiPh technology occurred in the mid-1980s [55]. SiPh finds diverse applications, with its most notable use in high-speed fibre-optic communication systems [56]–[58], particularly in long-distance transmission networks. Additionally, SiPh can be employed to interconnect servers and other components within data centres [59], [60] or to construct photonic quantum circuits for quantum computing [61], [62]. It is also a compelling choice for sensing and imaging applications, including medical imaging, environmental monitoring, and security systems, given its ability to offer superior sensitivity and resolution in comparison to traditional sensing and imaging technologies [63]–[69]. Finally, it has the potential to revolutionise Light Detection and Ranging (LiDAR) systems [70], [71], which are critical for autonomous vehicles, mapping, and remote sensing.

In this chapter, the outline of the basic SiPh structures required for one optical link and their working principle will be presented.

2.1 Waveguides

The basic structure of any Silicon Photonic device is a waveguide. Light is guided in the core of the waveguide thanks to total internal reflection as illustrated in Figure 2.1a. Proper guidance of the light requires the core's refractive index (n_1) to be higher than that of the cladding (n_2) surrounding it, and the angle θ to exceed the critical angle specified by Snell's law [72]:

$$\theta > \arcsin\frac{n_2}{n_1}. \tag{2.1}$$

In SiPh, a waveguide of Silicon (Si) is surrounded with the cladding of Silicon dioxide (SiO_2), as shown in Figure 2.1b. Typical SOI wafers, commonly used in SiPh, consist of a silicon substrate under 2 μm of oxide, also called buried oxide (BOX). On the top of the BOX is a 220 nm layer of crystalline silicon with a layer of oxide over it. At standard telecommunication wavelength, 1550 nm, Si has a refractive index of ≈ 3.48, while the refractive index of SiO_2 is ≈ 1.44. [73] The high contrast between the two enables easy guidance of light through the Si.

There are two types of waveguides that are commonly used in SiPh, strip and rib waveguides. The strip waveguide is a fully etched planar waveguide, as illustrated in Figure 2.2a, and it is usually used for routing. On the other hand, a partially etched rib waveguide, as shown in Figure 2.2b,

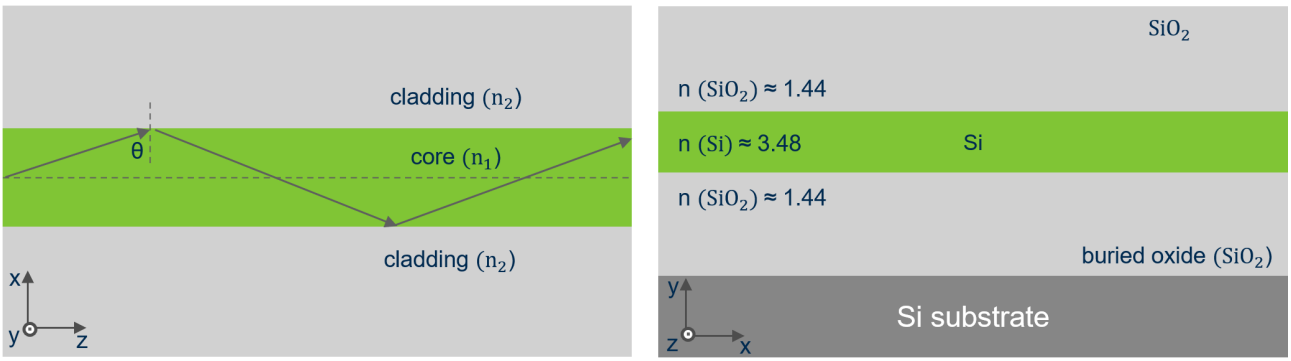

(a) **(b)**

Figure 2.1: (a) Principle of total internal reflection, necessary for the propagation of the light through the waveguide. (b) SOI planar slab waveguide.

is generally used for modulators. The rib waveguide has both shallow and deep etch variants, depending on the desired etch depth.

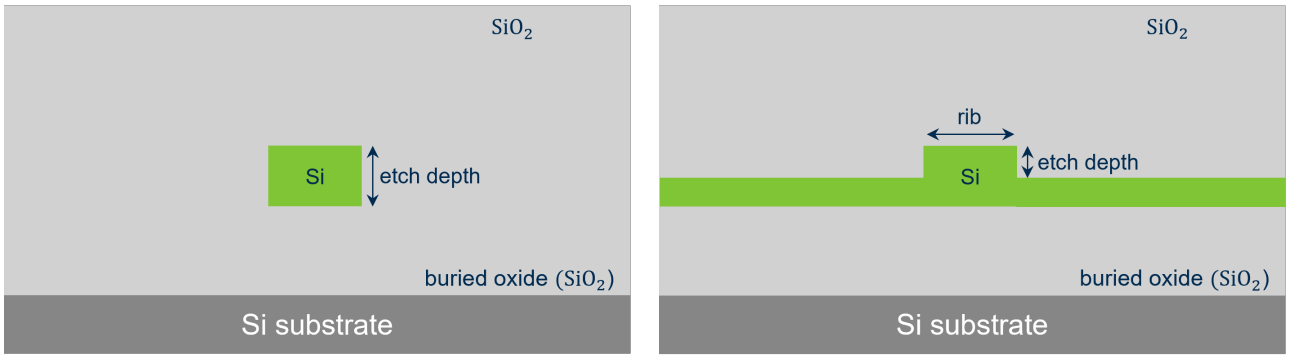

(a) **(b)**

Figure 2.2: Common waveguide types in silicon photonics. (a) Strip waveguide. (b) Rib waveguide.

Since light is an electromagnetic wave, its propagation in the waveguide can be described with Maxwell's equations:

$$\begin{aligned} \nabla \times \mathbf{E} + \frac{\partial \mathbf{B}}{\partial t} &= 0, \\ \nabla \times \mathbf{H} - \frac{\partial \mathbf{D}}{\partial t} &= \mathbf{J}, \\ \nabla \cdot \mathbf{D} &= \rho, \\ \nabla \cdot \mathbf{B} &= 0. \end{aligned} \tag{2.2}$$

where **E** and **H** represent vectors of electric and magnetic field, respectively. **B** is magnetic flux density, **D** is vector of the electric displacement field, **J** electric current density and ρ charge density. An optical mode [74] or a guided mode, is a specific pattern of electromagnetic fields that can propagate within an optical waveguide. It describes how light waves are confined and guided within a given structure. Modes are characterised by the distribution of electric and magnetic fields, polarisation, and propagation constants. The number of allowed optical modes depends on the geometry, effective refractive index, and other properties of the waveguide. For the single-mode

operation of the strip waveguide on 1550 nm, a width of around 500 nm is required for the height of 220 nm. Two types of modes can typically be found in strip and rib waveguides, Transversal Electric (TE) and Transversal Magnetic (TM) modes. Simulation results of a normalised electric field for TE and TM modes in a strip waveguide are presented in Figure 2.3. It can be noticed that only TE mode is guided in the structure of these dimensions, and TM mode is not supported. This confirms the single-mode operation of such a waveguide.

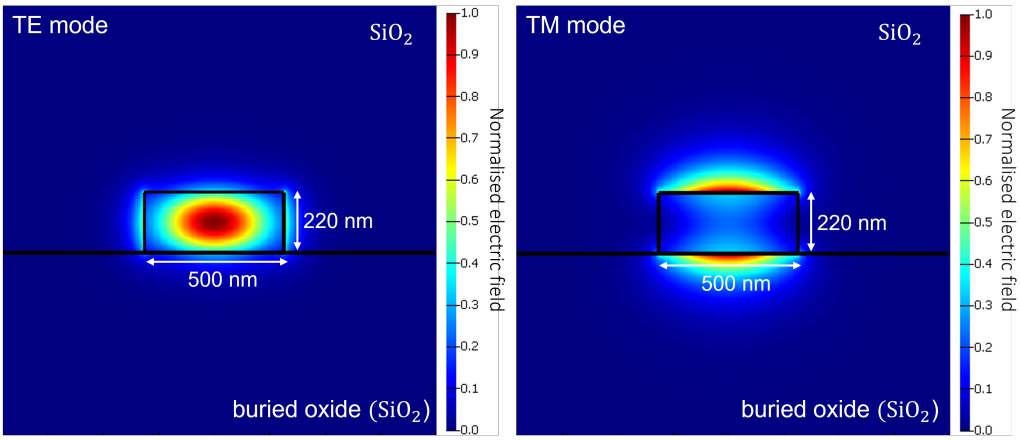

Figure 2.3: Distribution of the normalised electric field of Transversal Electric and Transversal Magnetic modes in silicon strip waveguide at 1550 nm.

The amount of loss in a waveguide is conditional to the extent to which the mode is confined within the waveguide. When the optical fields interact intensely with the waveguide walls, it can result in a significant amount of loss. Propagation loss in SiPh waveguides can be reduced with some optimisations. Having smooth sidewalls [75] is one of the requirements for a small loss, but it is not always feasible to control that due to complicated fabrication processes. The easier process of optimisation is by changing geometry parameters [76], [77] of the waveguide, which can reduce losses to solely 0.5 dB/cm. In SiPh, it is also possible to make sharp waveguide bends, down to a few microns, with very strong confinement and small losses. [78] This feature is used for routing waveguides through the chip, but also for the modulators as Ring Modulators.

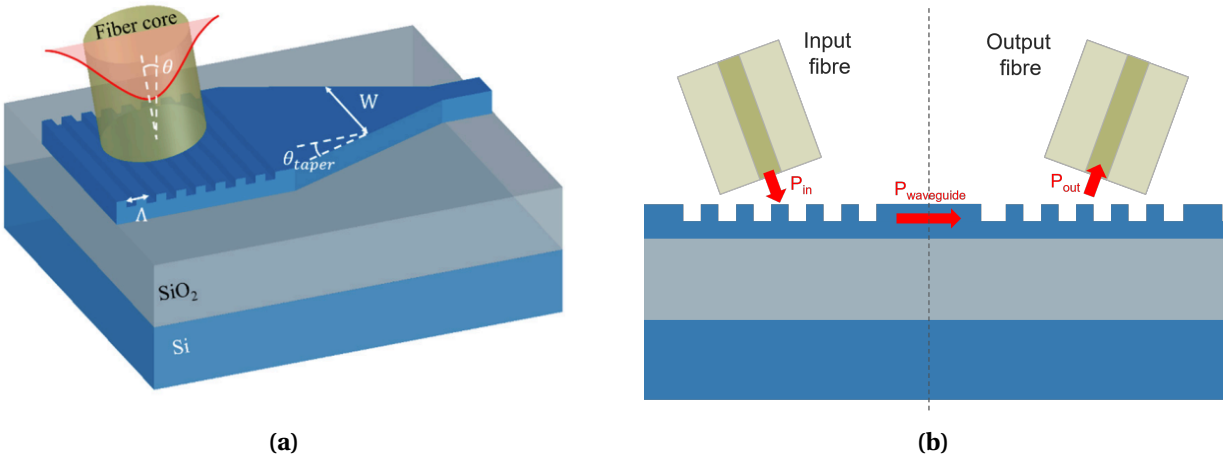

(a) **(b)**

Figure 2.4: Schematic structure of 1D grating coupler [79]. (a) 3D view. (b) cross-section view.

Grating couplers [79], [80], shown in Figure 2.4, are components on the SiPh chip necessary for coupling light into the chip by changing the direction of the light propagation. They are utilised for

coupling light from single-mode optical fibre to an integrated waveguide. The optical fibre is placed above the diffraction grating structure, almost orthogonally to the plane of the waveguide. Light is diffracted off the grating, and it will constructively interfere with the same plane as the waveguide (see Figure 2.4b). Likewise, light propagating through the waveguide can be coupled out with the same grating coupler structure.

When combined, the grating couplers, straight waveguides and bends are enabling routing light on one SiPh chip. In Figure 2.5, a simple scheme of the photonic integrated chip is shown. Two grating couplers are necessary for coupling light into the chip and out of the chip. In between the two, the light is guided through a network of straight and bend waveguides.

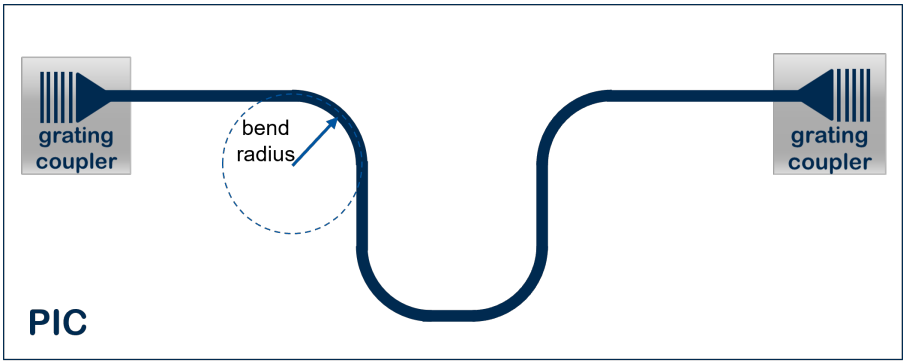

Figure 2.5: Simple scheme of the photonic integrated chip with two grating couplers, straight waveguides, and waveguide bends.

2.1.1 Phase shifter

Waveguides made of semiconductors, such as Si, can be doped, which means inserting impurities into a semiconductor crystal lattice. Depending on the type of impurity, there are n-doped and p-doped Si. N-doped silicon is usually doped with Phosphorus (P) or some other pentavalent atom as a donor, and p-doped Si is doped with Boron (B) or some other trivalent atom as an acceptor. The phase shifter is a combination of the p-doped, n-doped, and undoped Si between two contact electrodes. Control of the free carriers in a phase shifter is possible in three ways, by injection, accumulation or depletion of the carriers. A cross-section of the depletion phase shifter based on pn-junction and slab waveguide is shown in Figure 2.6. The change in the phase of light is happening due to changes in the medium where light is propagating. There are several ways to

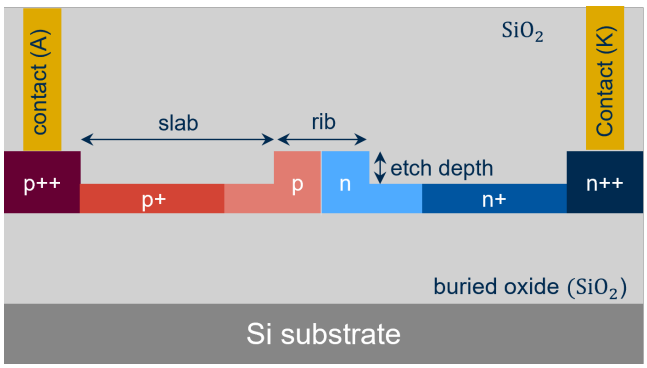

Figure 2.6: Cross-section of the typical phase shifter based on lateral pn-junction.

manipulate the light in the waveguide, induced by charge, field or temperature changes. Effects relevant to this work will be explained in the following.

2.1.1.1 The electro-refraction effect

The electro-refraction effects are the effects where the applied electric field induces a change in the refractive index of a material. The change in the refractive index is given by

$$n = n_0 + aE + bE^2 + \cdots, \tag{2.3}$$

where n_0 is the refractive index of the material without an applied electric field E. The second term in the equation 2.3 describes the Pockels effect, while the third term is the Kerr effect. However, since the Pockels effect exists only in noncentrosymmetric crystals, it is not present in crystalline silicon. The Kerr effect is present in silicon, and its strength is estimated in [81] by the anharmonic oscillator model:

$$\Delta n = -3e^2\left(n_0^2 - 1\right)\frac{E^2}{2n_0M^2\omega_0^2x^2} \tag{2.4}$$

where e is the elementary charge, M the effective mass, ω_0 the oscillator resonance frequency, and x is the average oscillator displacement. The predicted change in the effective index by the Kerr effect is equal to 10^{-4} for an electric field of $E = 10^6$ V/cm. This leads to the conclusion that it is fairly small for it to be used in integrated silicon photonics.

2.1.1.2 The electro-absorption effect

The electro-absorption effect is the effect where with the applied electric field, a change in the absorption of the material is induced. Light absorption in semiconductors occurs when the energy of the incident photon is equal to band gap energy. The absorption threshold is shifted towards lower energies with a strong electric field applied. The applied electric field bends conductive and valence bands, which enables photon-assisted tunnelling of the electrons between the bands. This effect is known as the Franz-Keldysh effect, and it is strong in direct band gap semiconductors and a little weaker in indirect band gap semiconductors such as Si.

The Franz-Keldysh effect has the peak for the band gap of 1.16 eV, which corresponds with a wavelength of about 1.07 μm. [82] At the wavelengths of interest in silicon photonics, 1.3 μm and 1.55 μm, even though it is stronger than the Kerr effect, this electro-absorption effect still has a quite small outcome.

2.1.1.3 The thermo-refraction effect

The thermo-optics effect is associated with the expansion or contraction of the crystal lattice of the material with the change in temperature, as well as the temperature-dependent carrier concentration and the temperature-induced reduction of the band gap. All mentioned effects have an impact on the change of the refractive index of the material, and the measure of the impact is named the thermo-optical coefficient.

The thermo-optical coefficient for crystalline Si at 20°C and $\lambda = 1.55\mu m$ [83] is:

$$\Delta n/\Delta T(Si) = 1.84 \times 10^{-4}\,\mathrm{K}^{-1} \tag{2.5}$$

Silicon also has a large thermal conductivity of 1.4×10^5 W/K [84]. Having this in mind, it is possible to have modulators based on the thermo-refraction effect [85], [86]. However, the temperature has a relatively low response speed, so it is not desirable for high-speed modulators. Nevertheless, this effect can be used for slow controls in the modulators, as it is the fine-tuning of the resonance wavelength (see Section 4.4).

2.1.1.4 The free-carrier plasma dispersion effect

The most important phenomenon for silicon photonics modulators is the free-carrier plasma dispersion effect. This effect is described by changes in the free-carrier concentrations, which also lead to changes in the refractive index and absorption coefficient of the material. It is used for silicon phase shifters and modulators where the concentration of carriers is varied either by injecting (injection type phase shifter) or removing carriers (depletion type phase shifter) from the device.

The change in refractive index (Δn) and absorption ($\Delta\alpha$) in the semiconductor due to the change in free electrons (ΔN_e) and free holes (ΔN_h) can be calculated by following equations [81]:

$$\Delta n = -\frac{e^2\lambda^2}{8\pi^2 c^2 \epsilon_0 n_0}\left[\frac{\Delta N_e}{m^*_{ce}} + \frac{\Delta N_h}{m^*_{ch}}\right] \tag{2.6}$$

$$\Delta\alpha = \frac{e^3\lambda^2}{4\pi^2 c^3 \epsilon_0 n_0}\left[\frac{\Delta N_e}{{m^*_{ce}}^2\mu_e} + \frac{\Delta N_h}{{m^*_{ch}}^2\mu_h}\right] \tag{2.7}$$

where c is the speed of light, ϵ_0 is the permittivity of the vacuum, m^*_{ce} and m^*_{ch} are the conductivity effective masses for electrons and holes, respectively, and μ_e and μ_h are the electron and hole mobility, respectively. In 1987, Soref and Bennet [81] analysed the plasma dispersion effect in the silicon for the telecommunications wavelengths. The result of their calculations is given by following semi-empirical equations:

$$\Delta n(\text{at } \lambda = 1.55\,\mu\text{m}) = \Delta n_e + \Delta n_h = -\left[8.8 \times 10^{-22}\Delta N_e + 8.5 \times 10^{-18}(\Delta N_h)^{0.8}\right] \tag{2.8}$$

$$\Delta\alpha(\text{at } \lambda = 1.55\,\mu\text{m}) = \Delta\alpha_e + \Delta\alpha_h = 8.5 \times 10^{-18}\Delta N_e + 6 \times 10^{-18}\Delta N_h \tag{2.9}$$

It is worth noting that the refractive index will decrease if the free carriers are injected into the material, and it will increase if the free carriers are depleted from the material. When it comes to the speed of the modulation in this way, the depletion mode offers a faster response time than the injection mode [87], [88].

The phase shifter presented in Figure 2.6 is based on lateral pn-junction. When the reverse bias voltage is applied to the contacts, the electrical field removes the free carriers from the depletion region and makes it wider. The width of the depletion region (W_d) is a function of the acceptor (electron) and donor (hole) concentrations (N_A and N_D, respectively) and applied bias voltage (V):

$$W_d = \sqrt{\frac{2\epsilon_0\epsilon_s(N_A + N_D)(V_{bi} - V)}{qN_AN_D}} \tag{2.10}$$

where ϵ_s is the relative permittivity and V_bi is the built-in potential given by

$$V_{bi} = \frac{k_B T}{q} \ln \frac{N_A N_D}{n_i^2}. \tag{2.11}$$

Here $k_B T/q$ is thermal voltage and n_i the intrinsic carrier concentration. With the change in the depletion width and carrier concentrations, the refractive index is also altered. The phase shift of the light in such a waveguide can be calculated by

$$\Delta\varphi = \frac{2\pi}{\lambda} \Delta n_{eff} L \tag{2.12}$$

where L is the optical path length, i.e. the length of the phase shifter. This leads to having relatively long waveguides in modulators to have enough phase shift for the light manipulation [89], [90].

2.2 Modulators

Silicon photonics modulators are devices that play a key role in the conversion of the electrical signal to an optical. Their working principle is based on modulating external light since the direct modulation of an internal light source integrated into the SiPh chip is not possible. More precisely, the information that was initially in the electrical domain will be encoded into the continuous wave (CW) light. Two primary types of SiPh modulators are the Mach-Zehnder Modulator (MZM) and Ring Modulator (RM). Their working principles will be described in the following.

2.2.1 Mach-Zehnder Modulators

The Mach-Zehnder modulators operate on the principle of the Mach-Zehnder interferometer (MZI). An MZI divides an incoming light beam into two equal parts through an ideal splitter. As the light propagates through the arms of the interferometer, the phase of the light changes, i.e. shifts. The interference and recombination of the two beams occur at the point where they merge. The phase of the light is a crucial factor for interference at the merging point. Constructive interference occurs when the phase difference between the two arms is $\Delta\phi = 2m\pi$, where m is an integer. On the other hand, destructive interference occurs when the phase difference is $(2m-1)\pi$. Therefore, the phase difference between the arms can be used to control the intensity of the output signal.

In the passive device as MZI, the phase difference can be induced by having one arm of the interferometer slightly longer. However, this approach is not modifiable. Once the MZI is manufactured, there is no possibility of further changing the phase difference between the arms. However, if at least one of the arms has an active element in it, where previously described electro-optical and/or thermo-optical effects can occur, the device is called a Mach-Zehnder modulator. In Figure 2.7, a scheme of MZM with phase shifters in both of the arms is shown. Phase shifters are based on previously explained pn-junction. The shift in one arm can be calculated using the equation 2.12, and it is directly proportional to the length of the phase shifter and effective refractive index n_{eff}. More precisely, the strength of the phase shift depends on the optical path length, $n_{eff}L$. If the electric field of the input beam is E_{in} and if the splitter is ideal, the electric field of the modes propagating in the arms just before the combiner can be calculated by

$$E_{out,1} = \frac{E_{in}}{\sqrt{2}} \sin(\omega t - \beta_1 L_1) \tag{2.13}$$

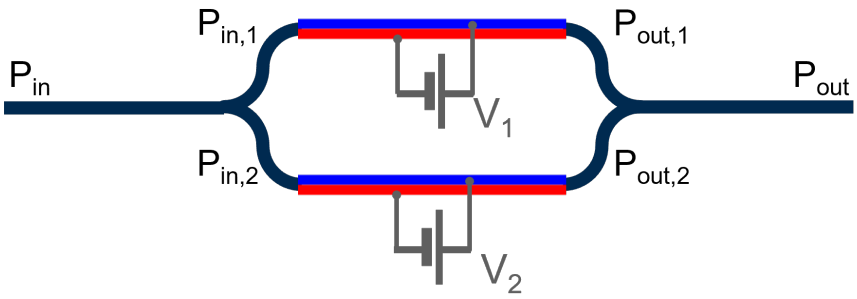

Figure 2.7: Schematic of the Mach-Zehnder modulator with the pn-junctions in both arms.

and

$$E_{out,2} = \frac{E_{in}}{\sqrt{2}} \sin(\omega t - \beta_2 L_2) \tag{2.14}$$

where $\beta = 2\pi\Delta n_{eff}/\lambda$. The total output optical power of the MZM can be given by

$$P_{out} = \frac{P_{in}}{2}(1 + \cos(\Delta\phi)). \tag{2.15}$$

Here, $\Delta\phi$ is the difference in phase between two arms. When the phase difference is zero, or it is a multiple of the 2π, the power on the output is equal to the input power if the absorption in the waveguide is neglected. If the voltage of V_π is applied to the phase shifter, the phase difference of π radians will be induced. In this case, the destructive interference will occur at the output, and the output optical power, in an ideal case, will be zero.

For the optimal operation of the MZM, the specific biasing conditions of the modulator where the two arms of the Mach-Zehnder interferometer are biased such that the phase difference between the two arms is $\pi/2$ radians is required. These conditions are satisfied at the quadrature point shown in Figure 2.8. The output of the modulator is highly sensitive to small changes in the input voltage, making this point an ideal operating point.

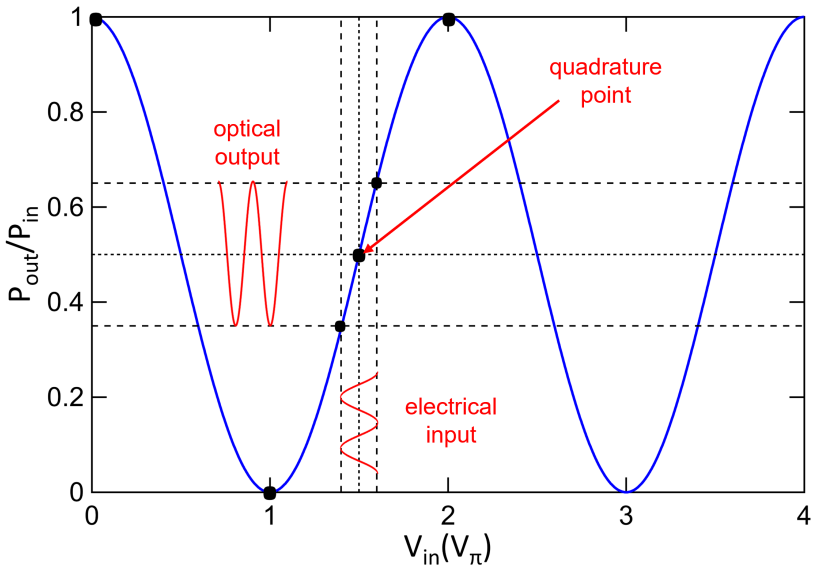

Figure 2.8: Transfer function of Mach-Zehnder modulator.

2.2.2 Ring Modulators

The second most common type of SiPh modulator is the Ring Modulator. It operates on the principle of the ring resonator. The basic structure of a ring modulator consists of a ring waveguide and a straight waveguide. The ring waveguide is a ring-shaped waveguide that is designed to trap light at certain wavelengths. The straight waveguide is placed close to the ring resonator and is used for input and output light signals.

In Figure 2.9, a model of the all-pass ring resonator is presented. When light is travelling through the upper waveguide, most of the wavelengths will pass through the through-port. If the resonance condition is fulfilled, the resonant wavelength will be coupled into the ring waveguide. The resonance condition is that the optical path length is equal to the product of the integer and the wavelength. More precisely, the resonance wavelength is given by the following equation:

$$\lambda_{res} = \frac{2\pi R n_{eff}}{m}. \tag{2.16}$$

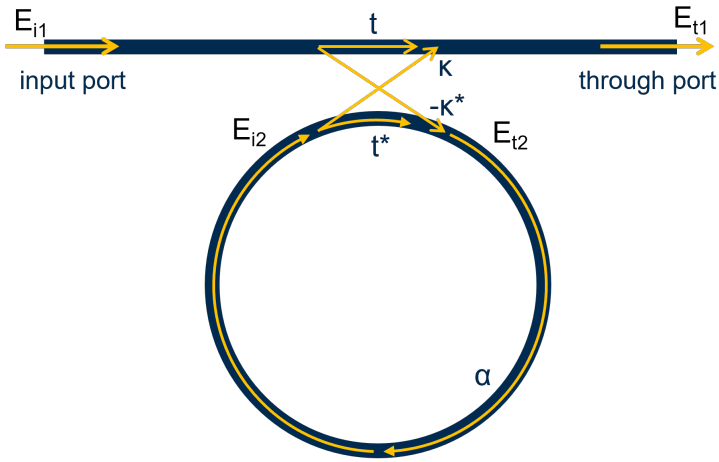

Figure 2.9: Model of a ring resonator with one input port and one through port.

where R is the radius of the ring, n_{eff} is the effective refractive index, and m is an integer. The principle of the light crossing from one waveguide to another is based on the evanescent field, i.e. the part of the field that is propagating outside the borders of the waveguide. The propagation of the light in the ring resonator can be written in the following matrix form [91]:

$$\begin{bmatrix} E_{t1} \\ E_{t2} \end{bmatrix} = \begin{bmatrix} t & \kappa \\ -\kappa^* & t^* \end{bmatrix} \begin{bmatrix} E_{i1} \\ E_{i2} \end{bmatrix} \tag{2.17}$$

where t and κ are coupling parameters(see Figure 2.9). E_{t1} is the transmitted electric field at the through-port, while E_{t2} is the electric field that is propagating through the ring waveguide. E_{i2} is the field after the one propagation in the ring, and it is given by

$$E_{i2} = \alpha e^{i\theta} E_{t2} \tag{2.18}$$

where α is the intrinsic loss of the ring waveguide and θ is the phase shift accumulated during the propagation through the ring:

$$\theta = 4\pi^2 n_{eff} \frac{R}{\lambda}. \tag{2.19}$$

If the phase shift induced by the coupler is ϕ_t and $t = |t|e^{\phi_t}$, the transmitted optical power according to [91] is

$$P_{t1} = |E_{t1}|^2 = \frac{\alpha^2 + |t|^2 - 2\alpha|t|\cos(\theta + \phi_t)}{1 + \alpha^2|t|^2 - 2\alpha|t|\cos(\theta + \phi_t)} \tag{2.20}$$

and the power after one round trip in the ring is

$$P_{i2} = |E_{i2}|^2 = \frac{\alpha^2(1 - |t|^2)}{1 + \alpha^2|t|^2 - 2\alpha|t|\cos(\theta + \phi_t)} \tag{2.21}$$

For simplification, the incident power E_{i1} is selected to be 1, and $|\kappa|^2 + |t|^2 = 1$. [91] When resonance is fulfilled, i.e. $(\theta + \phi_t) = 2\pi m$, the previous expressions can be simplified to

$$P_{t1} = |E_{t1}|^2 = \frac{(\alpha - |t|)^2}{(1 - \alpha|t|)^2} \tag{2.22}$$

and

$$P_{i2} = |E_{i2}|^2 = \frac{\alpha^2(1 - |t|)^2}{(1 - \alpha|t|)^2}. \tag{2.23}$$

The relation between the $|t|$ and α determines if the resonator is over-coupled, under-coupled or critically coupled (Figure 2.10b). The critical coupling occurs when the coupling coefficient $|t|$ is equal to the intrinsic loss of the ring resonator α. The output power on resonance, in this case, is equal to zero. The critical coupling condition is important in the design of silicon photonics ring modulators because it determines the extinction ratio and quality factor of the device. If $\alpha > |t|$, the ring resonator is over-coupled, and most of the input power is transmitted through the through-port without being coupled into the ring resonator. On the other hand, if $\alpha < |t|$, the ring resonator is under-coupled, and most of the input power is coupled into the ring without being transmitted through the through-port.

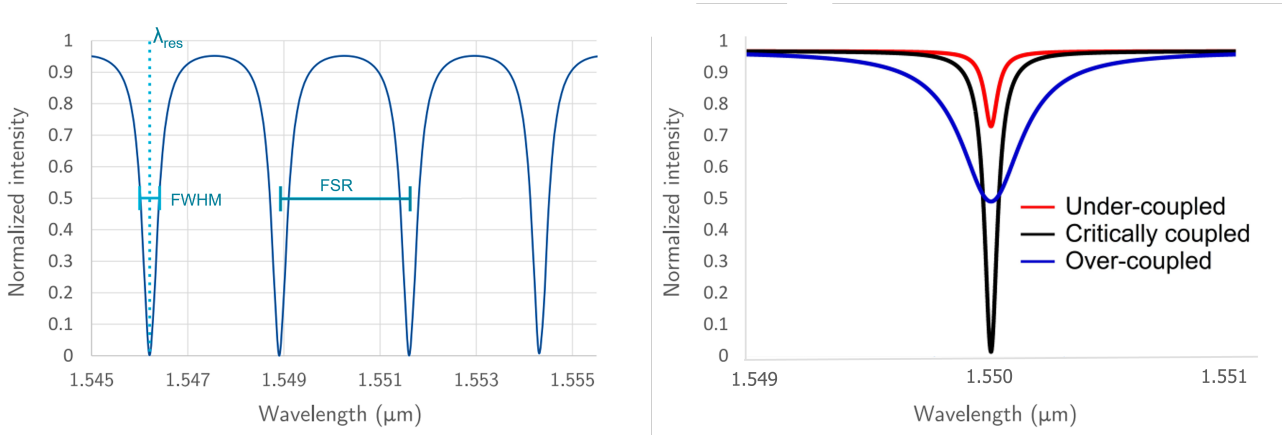

(a) **(b)**

Figure 2.10: (a) Optical spectrum on a through port of a ring resonator with annotated FWHM, FSR and λ_{res}. (b) Spectra of over-coupled, under-coupled, and critically coupled ring resonator (after [92]).

Some of the figures of merit that can describe the quality of the ring resonator are Free Spectral Range (FSR), Full-Width at Half-Maximum (FWHM), and Quality factor (Q) (see Figure 2.10a). Free spectral range describes the distance between the two consecutive resonance wavelengths. The FSR can be approximated by the following expression:

$$FSR = \lambda_{res}(m) - \lambda_{res}(m-1) \approx \frac{\lambda^2}{2\pi R n_{eff}} \tag{2.24}$$

The FWHM is the difference between the two points on the transmission curve where the transmitted power is half of the maximum value. The quality factor is a measure of the sharpness or selectivity of resonance in a ring resonator. It is defined as the ratio of the resonance wavelength to the FWHM of the resonance.

$$Q = \frac{\lambda_{res}}{FWHM} \tag{2.25}$$

The add/drop ring resonator is the configuration where the second straight waveguide is placed on the other side of the ring waveguide. This allows for partial transmission of the incident field from the first straight waveguide to the second straight waveguide. Moreover, if the ring waveguide is replaced by a doped ring waveguide, the configuration of the ring modulator shown in Figure 2.11 is obtained. In this configuration, when a voltage is applied to the phase shifter in the ring, the effective index of the ring waveguide is changed due to the free-carrier plasma dispersion effect. Thus, according to the equation 2.16, the resonant wavelength will accordingly be shifted. This is illustrated in Figure 2.12.

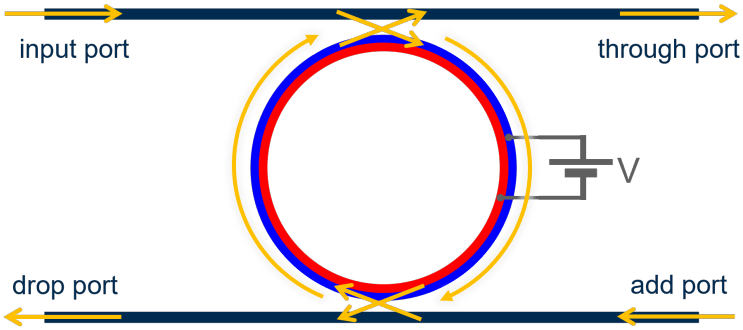

Figure 2.11: Schematic of the ring modulator in add/drop configuration with the pn-junctions in the ring waveguide.

Some figures of merit that can be used to characterise the performance of ring modulators are modulation efficiency, Insertion Loss (IL), Extinction Ratio (ER), and Optical Modulation Amplitude (OMA). Modulation efficiency is a key parameter that describes the effectiveness of the modulator, and it is defined as the shift in the resonance wavelength induced by the applied reverse bias voltage. In particular, modulation efficiency is the difference between the resonant wavelength when 0 V is applied and when 1 V reverse bias voltage is applied to the contacts of the phase shifter, as shown in Figure 2.12.

$$\text{modulation efficiency} = \lambda_{res}(V) - \lambda_{res}(0\,\text{V}) \tag{2.26}$$

Insertion loss is a loss in the output power when the modulating signal is present (logical 1), relative to the input power.

$$IL = 10\log\left(\frac{P_{in}}{P_1}\right) \tag{2.27}$$

Extinction ratio measures the ratio of the power in the state when the modulating signal is present (logical 1) to the power when the modulating signal is absent (logical 0). It is typically expressed in dB, and higher ER values indicate better performance.

$$ER = 10\log\left(\frac{P_1}{P_0}\right) \tag{2.28}$$

Optical modulation amplitude is a difference between the power when the modulating signal is present (logical 1) and the power when the modulating signal is absent (logical 0). It is typically expressed in mW.

$$OMA = P_1 - P_0 \tag{2.29}$$

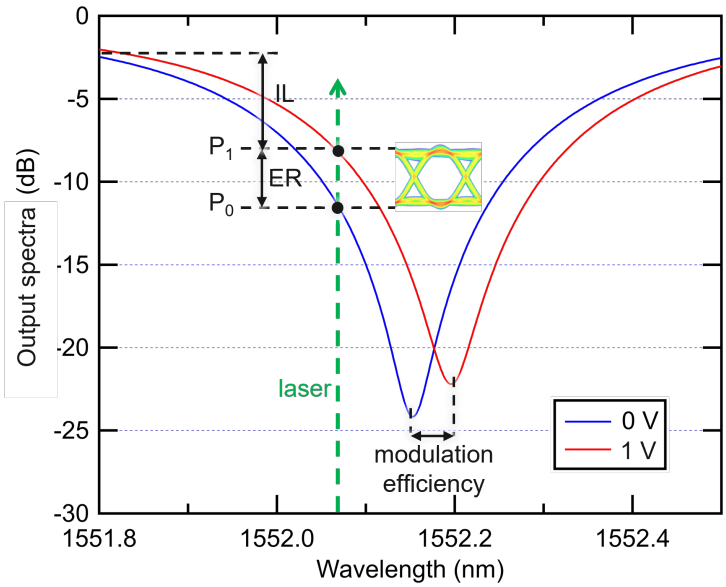

Figure 2.12: An example of the RM transmission spectra for 0 V and 1 V reverse bias. The modulation efficiency is the difference between the two resonance wavelengths.

2.3 Photodiodes

For the full operation of one optical link, it is necessary to convert the signals from the optical to the electrical domain. Optical-to-electrical signal conversion is achieved through the photodiodes, which are essential components in this process. Germanium is a material that has proven to be compatible with SiPh and CMOS manufacturing [93]–[95]. Germanium is an excellent choice for on-chip photodiodes in silicon photonics due to its ability to absorb a large amount of light in the telecommunication wavelengths[96], unlike silicon, which is transparent in those regions.

In SiPh, the most practical devices are integrated germanium-on-silicon (Ge-on-Si) p-i-n (PIN) photodiodes [97]–[99] where the opto-electrical conversion takes place in a depleted intrinsic (i) region between p-type and n-type regions. When the intrinsic layer is illuminated with light, photons are absorbed, and electron-hole pairs are created, which are swept by the built-in electric field. One of the benefits of this layer is that the capacitance of the junction is decreased, leading to an increase in the speed of the photodiode's response, which is necessary for high-speed links. PIN photodiodes can work in two bias conditions: forward bias and reverse bias. When operated in a forward bias state, the charge carriers from the p and n regions enter an intrinsic region, and

the width of the depletion region decreases. On the other hand, in a reverse bias state, the charge carriers are swept away from the intrinsic region and the width of the depletion region will increase.

There are two main types of Ge-on-Si PIN photodiodes: lateral and vertical PIN photodiodes. The lateral Ge PIN photodiode, shown in Figure 2.13a, consists of intrinsic Ge located between p-doped and n-doped silicon regions, which are in the same plane. The diode's cathode and anode contacts are located at the end of those doped Si regions. Figure 2.13b shows the vertical Ge PIN photodiode. It consists of intrinsic Ge located between p-doped and n-doped silicon, where n-doped Si is under the Ge and p-doped Si is above the Ge.

The main figures of merit for photodiodes that will be used in this thesis are photocurrent, dark current, and responsivity. The photocurrent is the electrical current generated in a material when exposed to light, and it is proportional to the intensity of the incident light. Responsivity is the ratio of the photodiode's output current (photocurrent) to the incident optical power. It is expressed in units of amperes per watt (A/W). Dark current is the current that flows through the photodiode in the absence of light. Both currents will be measured when photodiodes are reverse biased with 1 V.

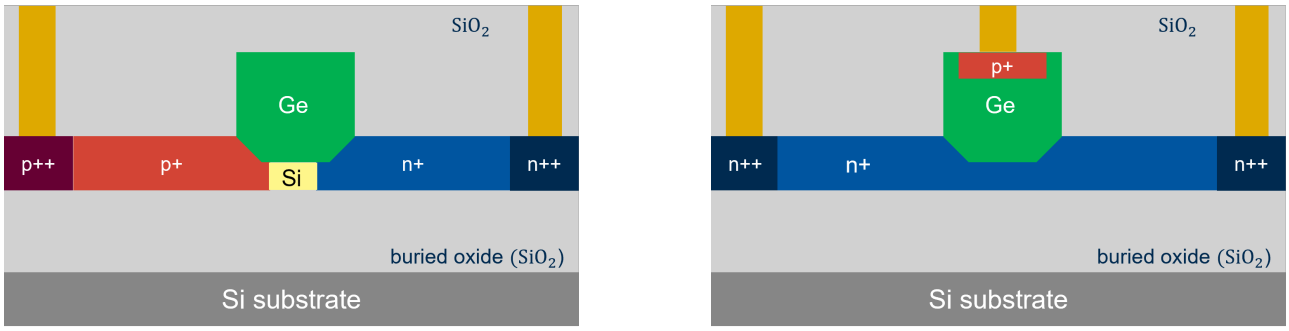

(a) **(b)**

Figure 2.13: (a) Cross-section of the Si-doped lateral Ge PIN photodiode. (b) Cross-section of the Si-doped vertical Ge PIN photodiode.

Chapter 3

Radiation Effects in SiPh devices

The LHC is known to produce a vast amount of particles as a result of its proton-proton collisions. Among these particles, both charged and uncharged particles exist, each capable of impacting the components installed within the detectors. Silicon photonics devices, as well as all other components, are not immune to such effects, and may therefore experience radiation-induced damage. Radiation damage effects can be classified into two main categories: damage from ionisation events (i.e. from ionising energy losses) and displacement damage from non-ionising energy losses [100].

The first type of damage is caused by ionising particles (including photons) that deposit energy in the insulator and semiconductor materials. This leads to various effects in semiconductor-based devices. This type of damage is surface damage, leaving defects close to the surface or at the interfaces between regions of different materials. On the other hand, displacement damage occurs when a heavy particle, such as a neutron, proton, or heavy ion, interacts with an atom in the material, transferring kinetic energy to the atom and causing it to collide with other atoms, leading to the displacement of atoms from their lattice sites. This type of damage is classified as bulk damage. Both effects are cumulative, meaning their influence accumulates over time.

A special type of effect caused by a single ionising particle rather than by accumulated radiation are Single Event Effects (SEEs) [101]–[103]. They typically occur in electronic Integrated Circuits (ICs), however, there are reports of SEEs occurring in SiPh ICs [104]–[106]. SEEs are usually caused by the interaction of high-energy particles with ICs, and they can cause temporary or permanent changes in the device's performance, such as bit flips in digital circuits. SEEs are typically an isolated occurrence rather than a cumulative effect, and they can occur even with any level of radiation exposure. In SiPh circuits, SEEs are not investigated well enough as SEEs in electronic circuits.

In general, the effects of radiation depend on a variety of factors, including the type and energy of the radiation, the type of material, and the specific device design. In this thesis, only ionisation damage and displacement damage from non-ionising energy loss will be discussed.

3.1 Damage from the total ionising dose

Ionisation damage occurs when energy is deposited in the material due to ionising particles, such as electrons, X-rays, and γ-rays. In SOI devices, when an ionising particle hits the material, it creates an electron-hole (e-h) pair. Different types of photon-matter interactions can occur depending on photon energy, as shown in Figure 3.1 [100]. At lower energies, if the photon has enough energy (1838.9 eV for Si [107]), it will eject an electron from the K-shell (the closest one to

the nucleus) and the photon is completely absorbed. The ejection of the K-shell electron amounts to the creation of an e-h pair. Each of these two particles (the electron and the hole) may produce additional e-h pairs in subsequent collisions while slowing down. At the medium photon energies, the Compton effect predominates. In this case, the photon is scattered off one of the loosely bound outer electrons, again creating an e-h pair. The photon itself propagates further along a new direction and with a lower energy. At high photon energies (above 1.022 MeV), the photon energy is fully absorbed and an electron-positron pair is created. To generate such a pair, the incident photon must have a minimum energy of 1.022 MeV, which corresponds to the rest energy of the electron and positron (511 keV each).

In this thesis, the energy of the X-ray beam mainly used for irradiating SiPh devices is 10 keV. Having that in mind, the dominant effect will be the photoelectric effect.

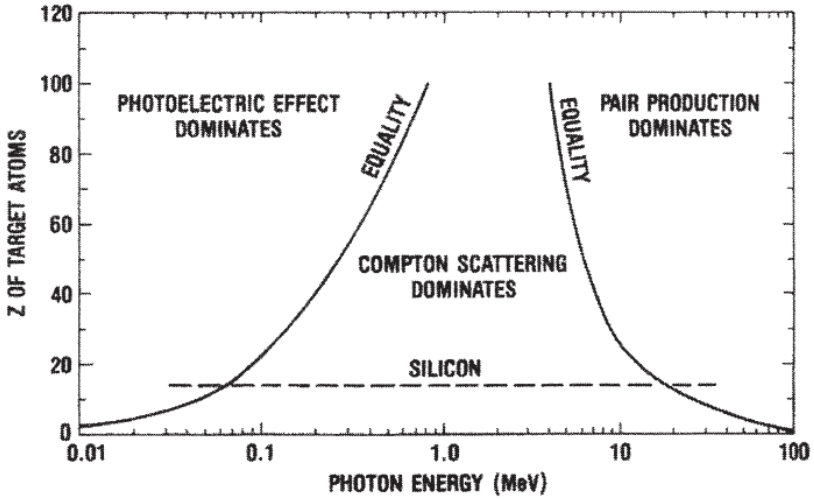

Figure 3.1: Different types of photon-matter interactions depending on photon energy and material. [100]

Ionisation damage can be quantified through Total Ionising Dose. TID represents the total amount of energy that is deposited in the material due to ionisation. One of the units used to measure TID is rad. One rad is defined as the dose necessary for the absorption of 100 erg [1] of energy per gram of material. TID can also be measured in Gy, where 1 Gy = 100 rad. Dose is always expressed for a specific material exposed to radiation, for example, in units of Gy(Si) or Gy(SiO_2) for silicon and silicon dioxide, respectively.

The principle of how different defects are created within the silicon dioxide on the example of a positively biased metal–oxide–semiconductor (MOS) structure is presented in Figure 3.2. When a high-energy photon interacts with the material, silicon dioxide, the electron-hole pairs will be created through ionisation processes. The amount of the e-h pair depends on the absorbed dose, and in SiO_2 is 8.1×10^{12} pairs/(cm^3rad) [108]. The mean energy necessary for the generation of the e-h pair is 17 eV [108]. Once created, the electron-hole pairs can interact with the surrounding environment in different ways. In general, there are three possible pathways for the electron-hole pairs. Primary, in the first picoseconds after the generation, one part of the e-h pairs will be recombined [109]. The remaining part of the electron-hole pairs that does not recombine is called charge yield and it depends on the electric field and the energy and type of the incident particle [110]. Furthermore, since radiation-generated electrons are far more mobile than holes, the electrons will be dragged out of the oxide and collected on one of the bias electrodes and only

[1] Unit of energy. 1 erg = 100 nJ

holes will remain in the oxide after the initial period of a few picoseconds. The third pathway is that the holes then migrate through the SiO_2 and towards the Si/SiO_2 interface by hopping from one defect to another (localised states) [111]. When holes are near the Si/SiO_2 interface, a part of them is captured in the pre-existing deep-trap zone, predominantly within 5 nm of the interface, and they become permanently trapped [112]. The amount of permanent traps is correlated with the production processes and purity of the oxide, i.e. a ratio of pre-existing defects. These defects are also known as border traps.

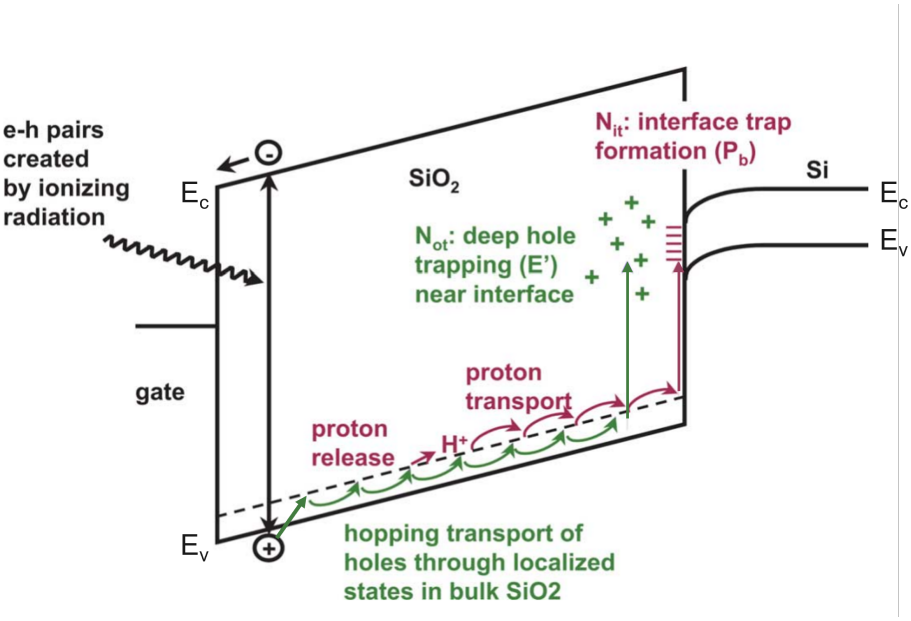

Figure 3.2: Main processes of radiation-induced creation of traps in SiO_2.[113]

The other type of traps formed as an outcome of moving holes are interface traps. Hydrogen (H) is one of the impurities present in SiO_2, since it is used in different manufacturing processes such as depositions, etchings or polishing [114]. Even though the presence of hydrogen in the device can be a benefit in some cases, in the case of radiation-hard devices, it is only a disadvantage. [115] The moving holes (h^+) can interact with defects containing hydrogen and in this process, the hydrogen ions (H^+) are released [116].

$$h^+ + H \rightarrow H^+ \tag{3.1}$$

These ions then can cause the formation of interface traps [117]. In production processes, hydrogen is employed for the purpose of passivating or saturating the unpaired electrons (dangling bonds) found on the surface of silicon, resulting in the formation of silicon-hydrogen (Si-H) bonds. This technique is used to enhance the quality of oxide layers grown on silicon. When hydrogen ions, induced by radiation, come into contact with pre-existing Si-H bonds near the Si/SiO_2 interface, they combine to form hydrogen gas (H_2), consequently causing the creation of new dangling silicon bonds [118].

$$H^+ + \text{Si-H} \rightarrow Si^+ + H_2 \tag{3.2}$$

Here, Si^+ represents dangling Si bond defects, where silicon is bonded to three other silicon atoms and one of the electrons at the Si/SiO_2 interface stays unpaired. Therefore, these defects are called interface traps. They are also named P_b centres. [119] Depending on the type of vacancy at the

Si/SiO_2 interface, there are three types of P_b centres, at (111) oriented Si/SiO_2 interface P_b defects are observed [120], and at (100) oriented Si/SiO_2 interface P_{b0} [121] and P_{b1} [122], [123] are present.

The buildup of the interface traps is dependent on the dose rate of incoming radiation [117]. As mentioned before, border traps are primarily formed by the movement of holes, while interface traps are induced by hydrogen ions (protons). The mobility of holes and protons differs, with holes being considerably more mobile than protons. In low dose rate scenarios, as in space environments, there is sufficient time for protons to be generated and then to reach the interface, interact with Si-H bonds and form the interface traps. For the high dose rates, the hole will reach the border region before the protons and form a vast amount of the border traps. As the quantity of traps increases, an electrostatic barrier is created near the interface. This barrier will prevent both holes and protons from reaching the interface and forming interface traps. (see Figure 3.3) Therefore, in high dose rate scenarios like those expected in the LHC and HL-LHC, the presence of interface traps in SOI devices is negligible.

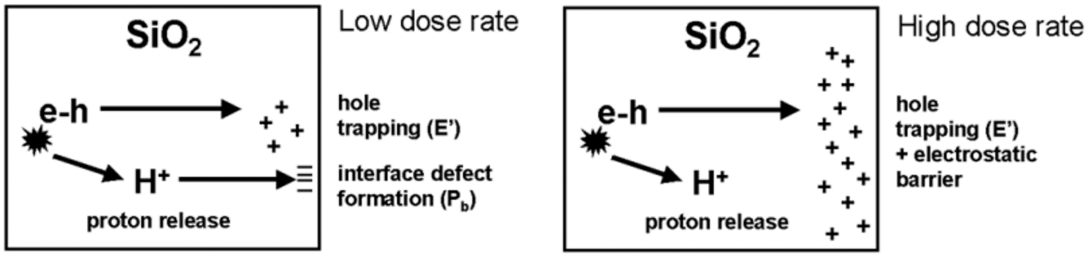

Figure 3.3: The buildup of interface traps at the Si/SiO_2 interface for low and high dose rates.[117]

A crystal containing radiation-induced defects tends to spontaneously revert to its stable state over time, if the temperature is over 0 K [124]. This process is called annealing [125], [126]. Based on how this process is assisted, in SOI devices, there are thermal annealing [127]–[129], bias annealing [130], [131], and laser annealing [132], [133]. The most commonly used method of annealing is thermal annealing. Thermal annealing involves heating the device to a high temperature to activate diffusion and repair the radiation-induced defects. The elevated temperature allows the free electrons and holes in the device to move and recombine, reducing the concentration of defects and improving device performance. In the bias and laser annealing, the current and the photons are used, respectively, for the activation of the annealing effect.

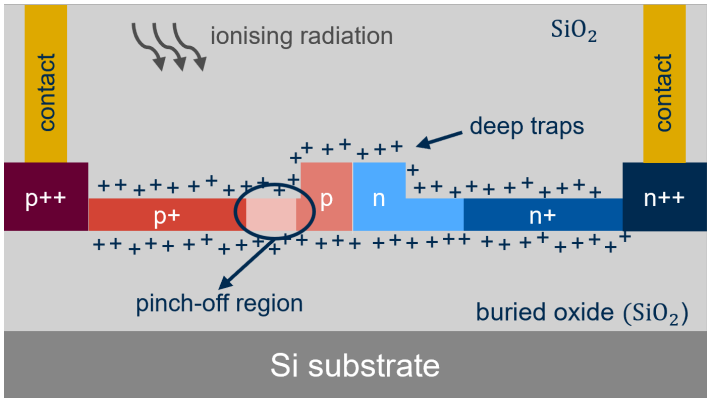

Figure 3.4: Illustration of the ionising radiation effects in SiPh phase shifter. The fixed positive charge is generated at the interface Si/SiO_2 by the incident ionisation. The pinch-off region is formed as a consequence of ionising radiation damage.

In Figure 3.4, a cross-sectional view of the SiPh phase shifter exposed to the ionising radiation is presented. As previously stated, when subjected to a sufficiently high dose rate, the formation of deep border traps near the Si/SiO_2 interface occurs. These deep traps are positively charged and immobile (fixed). On the opposite side of the interface, doped silicon is situated, consisting of both p-doped and n-doped regions. Due to the mobility of carriers in doped silicon, unlike the deep traps, a phenomenon known as hole ejection occurs when there is p-doped silicon adjacent to a fixed positive charge [134], which pushes the free holes in the p-doped slab away to the left and right, making the concentration of free holes in the slab even lower. The manifestation of hole ejection is more evident in regions with lower levels of p-doping, as a greater amount of fixed charge is required to remove all holes from highly doped p-regions. Once all free holes have been expelled from the p-doped Si, an electrical connection between the two contact electrodes is severed. The region where no free carriers are present is named the pinch-off region. In the absence of an electric field within the waveguide, the ability of the phase shifter to modulate light decreases. As a result, the phase shifter becomes non-functional.

3.2 Displacement damage from the non-ionising energy loss

Apart from the damage caused by ionising radiation, semiconductor devices located in the LHC are exposed to the damage associated with non-ionising radiation. The high-energy particles, such as neutrons, protons or heavy ions, engage in interactions with the atoms within the crystal lattice. The part of the energy that is transferred to the lattice is defined as a Non-Ionising Energy Loss (NIEL). When the energy of the particle is high enough, during an elastic or inelastic collision, the energy passed to the atom in the material can be sufficient to displace the atom from its initial position in the crystal lattice. The atom which is displaced is called a Primary Knock-on Atom (PKA) [135] and this kind of damage is therefore known as displacement damage. This effect can result in the creation of lattice defects also known as the Frenkel pair, which consists of the lattice vacancy, i.e. an unoccupied lattice site, and the interstitial atom, i.e. an atom occupying non-lattice positions. (see Figure 3.5) The majority of the PKA will be shortly recombined back in the vacancy. However, if the energy of the PKA is high enough, it can create a cascade effect and knock out further atoms. These atoms can then act as new PKAs until they recombine in the free vacancy or until they become permanently trapped in some of the preexisting defects.

The minimal energy to dislocate an atom from the lattice must be greater than the binding energy, and in silicon, it is approximately 25 eV. For initial PKA, to become a source of the secondary PKAs, that energy must be even higher. As an illustration, for a 1 MeV neutron, only about 60 – 70 keV of energy is transferred further to the silicon recoil atom. This can dislodge nearly 1000 additional atoms in a region of 0.1 μm in size [136].

In silicon, several effects are manifested as a result of displacement damage (Figure 3.6), primarily related to the introduction of new energy levels [100]:

- thermal generation of e-h pairs,
- recombination of e-h pairs,
- trapping carriers at radiation induces energy levels,
- change in donors and acceptors concentrations, and
- tunnelling carriers.

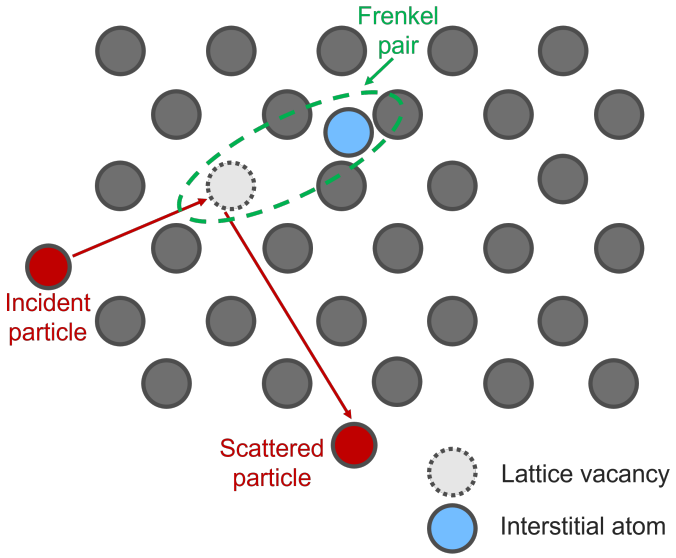

Figure 3.5: Illustration of creation of the displacement damage in the semiconductor crystal lattice. The incident particle dislocates the atom from the lattice, resulting in the creation of the Frenkel pair.

These effects generate degradation of the electrical and optical properties of the semiconductor. Due to the formation of the energy state near the middle of the band gap, generation and recombination of the e-h pairs are facilitated. When the energy states are formed close to the valence or conduction band, carriers can be trapped at these levels and emitted after some time. The third example in Figure 3.6 shows how the electron from the donor level can pass to the radiation-induced level and alter the carrier concentration. This type of damage can make n-doped and p-doped regions less doped and in the end intrinsic. In extreme cases, for high radiation doses, doped silicon can become inversely doped [136]. The last case is the tunnelling of the carriers through the barrier with the assistance of the intermediate state.

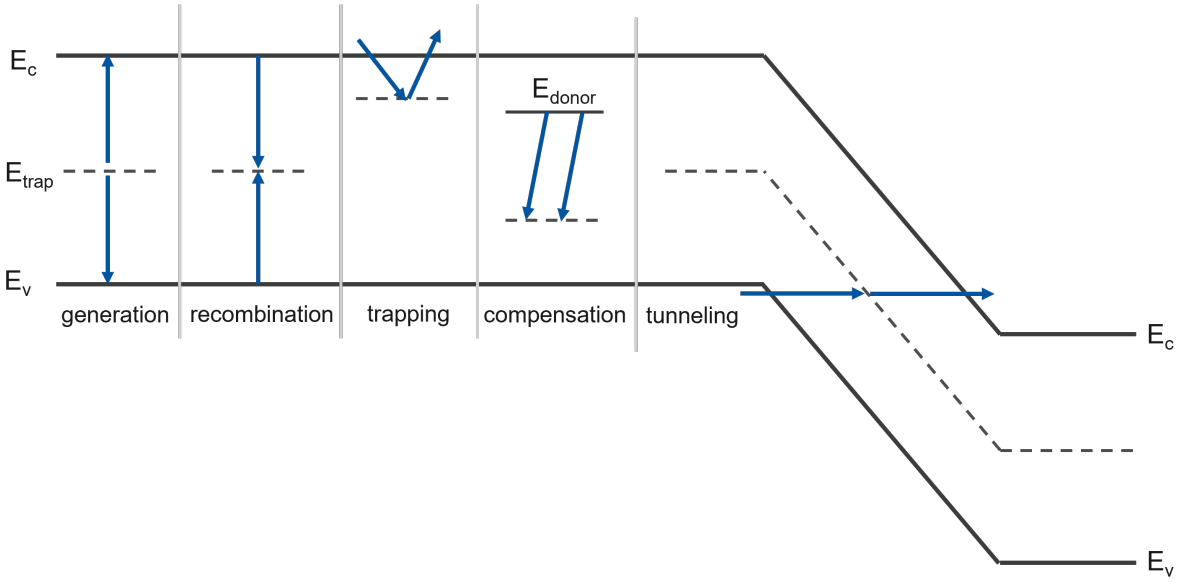

Figure 3.6: Intermediate states in semiconductor as a consequence of radiation damage (after [137])

Ionisation losses will not make any changes in the crystal lattice, thus the bulk damage occurs only because of non-ionising energy loss. However, the extent of damage is subject to several factors

including the type of the material, the type of the incident particle producing the damage, and its energy. Figure 3.7 illustrates the defect distributions in silicon resulting from three distinct incident particles. The left subfigure represents damage induced by 10 MeV protons, the middle subfigure displays defects caused by 24 GeV/c protons, and the right subfigure shows damage from 1 MeV neutrons [138]. Notably, the neutron-induced damage exhibits a more clustered pattern, while defects from 10 MeV protons appear to be evenly distributed. 24 GeV/c protons form a pattern that consists of both clusters and uniformly distributed damage sites, combined. As a solution to the problem of how to compare these damages, a NIEL scaling hypothesis was proposed [139]–[141].

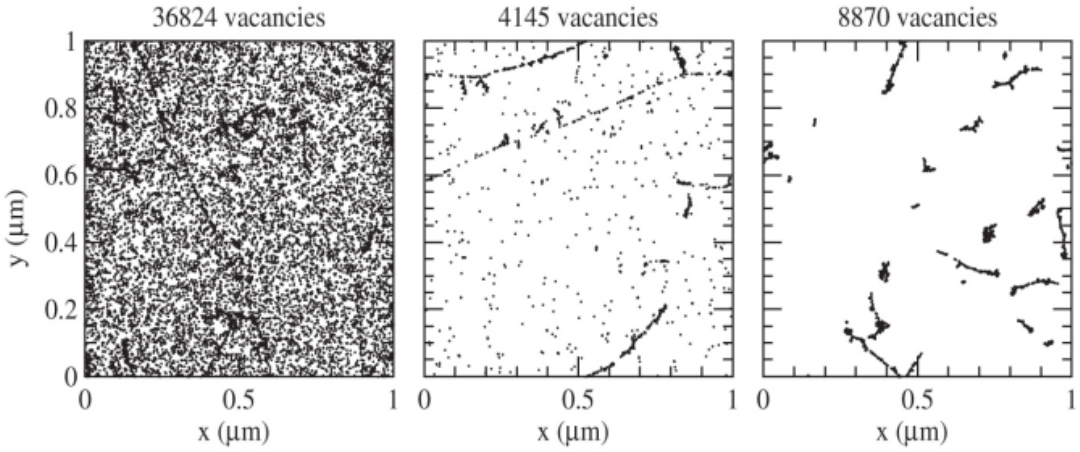

Figure 3.7: Simulation of the distribution of defects (vacancies) in 1 μm^3 of silicon, induced by 10 MeV protons (on the left), 24 GeV/c protons (in the middle), and 1 MeV neutrons (on the right) [138].

NIEL scaling hypothesis states that the bulk damage is directly proportional to the amount of energy deposited in the crystal lattice as the outcome of the collisions, regardless of where the defects are located or what happens afterwards. The part of the recoil energy that is deposited in the form of displacement damage is dependent on the recoil energy E_R and it can be estimated by the Lindhard partition function $P(E_R)$ [142]:

$$D(E) = \sum_i \sigma_i(E) \int_0^{E_R^{max}} f_i(E, E_R)\, P(E_R)\, \mathrm{d}E_R \tag{3.3}$$

Here, i is the index of all possible interactions between the incoming particle and the silicon atoms in the crystal lattice and σ_i is the cross-section for the interaction i. Function $f_i(E, E_R)$ is the probability of generating a PKA with recoil energy E_R by a particle of energy E, during the interaction i.

For comparing the damage efficiency generated by different particles with individual energy spectra $\phi(E)$ a hardness factor κ was defined. The hardness factor is usually normalised to the equivalent damage that would have been produced by the neutrons of 1 MeV:

$$\kappa = \frac{\int D(E)\phi(E)\mathrm{d}E}{D(E_n = 1\,\mathrm{MeV}) \int \phi(E)\mathrm{d}E} \tag{3.4}$$

where $D(E_n = 1\,\mathrm{MeV})$ is equal to 95 MeV·mb [143]. The equivalent fluence Φ_{eq} can be calculated by:

$$\Phi_{eq} = \kappa \Phi = \kappa \int \phi(E) \mathrm{d}E \tag{3.5}$$

and it is given in units n_{eq}/cm^2. It should be noted that the NIEL hypothesis is not ideal and the estimations of the total equivalent fluence can vary depending on the particles and energies in question. Limitations of the NIEL hypothesis are discussed in [138]. An example of simulations of normalised displacement damage functions $D(E)$ for neutrons, protons, electrons, and pions, taken from [144], is presented in Figure 3.8.

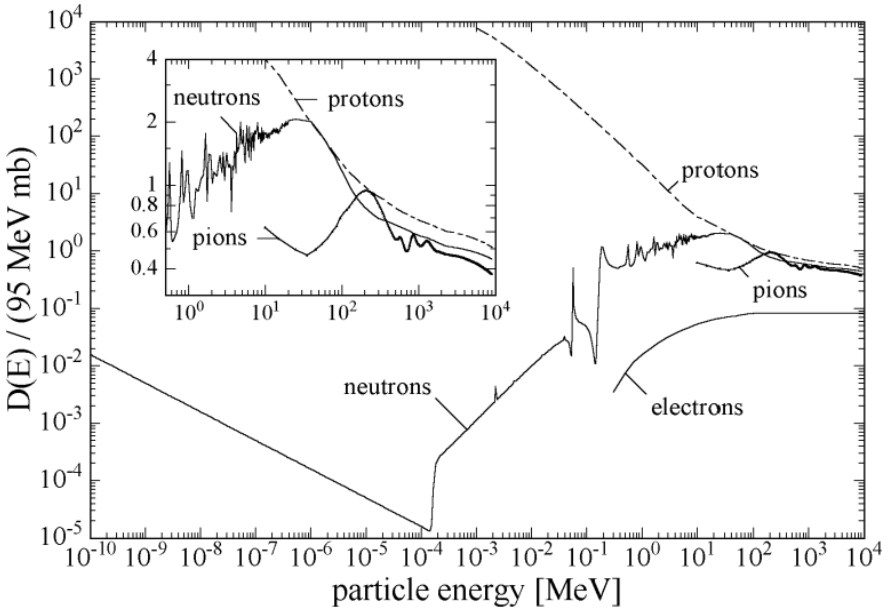

Figure 3.8: Displacement damage function $D(E)$ for neutrons, protons, electrons, and pions normalised to 95 MeV·mb [144].

Similarly to ionisation damage defects, displacement damage defects are not permanent and they can be annealed. There are two main mechanisms for the annealing of displacement damage. First, migration and complex formation is a process where defects (vacancies and interstitial atoms) become mobile at certain temperatures, and then they migrate through the crystal lattice. They can then recombine or they can form new and more complex defects with other impurities. These complex defects are more thermally stable than initial defects and a higher temperature is necessary to set them in motion again. This process is also called reverse annealing, as damage is increasing after the irradiation. The second mechanism is the dissociation of defects, where the defects are dissociated if the lattice vibrational energy is high enough to overcome the binding energy of the lattice [144]. Further, the defect will migrate until it is recombined or it forms a more complex defect.

Chapter 4

Silicon Photonics Chip functionality validation

Test vehicles for testing the radiation tolerance of Silicon Photonics devices have been Photonics Integrated Chips. The Back-End (BE) section of the Electronics Systems for Experiments (ESE) group at CERN [145] is investigating new technologies for the improvement of the current optical links. In 2014, the group initially designed the first version of the PIC, which was afterwards manufactured by IMEC (Interuniversity MicroElectronics Centre) [146] in 2015, in their iSiPP25G platform. This initial chip demonstrated promising results for radiation-hard silicon photonics devices [147]. SiPh Mach–Zehnder modulators showed that they can withstand TID levels up to a few hundred kGy [148], [149] and neutron fluence up to $2 \times 10^{15} \mathrm{n/cm^2}$ [150]. While it is sufficient enough for a large number of potential terrestrial and space applications, new particle physics experiments in preparation are requiring tolerance to much higher levels than the ones mentioned above, specifically 10 MGy and $1.6 \times 10^{16} \mathrm{n/cm^2}$. Based on the results from [148], [149], and the hardening by design (HBD) methods suggested therein, a new silicon photonics integrated chip with a novel and improved design of the SiPh PIC (PICv2) was designed by the EP-ESE-BE section at CERN and then fabricated by IMEC as a part of a Multi-Project Wafer (MPW) run.[1] The PICv2 was delivered at CERN in May 2020. [2]

4.1 Silicon Photonics Chip Design - PICv2

In May 2020, CERN received two batches, each containing approximately 40 bare chips (also known as dies), as depicted in Figure 4.1a. These chips were manufactured as part of an MPW run, wherein multiple projects and designs from different users share the space of one single wafer. This production approach was chosen due to the significant cost reduction compared to producing an entire wafer individually. The fabrication was conducted on IMEC's MPW iSiPP50G platform [151], which allows for the prototyping of high-speed SiPh components on 200 mm Silicon-On-Insulator wafers with 220 nm thick crystalline silicon on top of the 2 μm thick buried oxide. In this platform, some building blocks pre-designed by IMEC are offered, as well as the possibility of making custom designs within the limits of the platform. This platform offers three different etch depths, the possibility of doping with four n-type doping levels and four p-type levels, two metal layers, and the growth of the Ge on silicon. IMEC's standard allocation for each project on the wafer is an area

[1] The design of the chip is not part of this thesis.

[2] This thesis covers the work on the chip from the moment of its arrival at CERN.

measuring 5 mm by 5 mm, which will, therefore, be the dimensions of PICv2. Figure 4.1b depicts a microscopic view of one of the bare PICv2 chips.

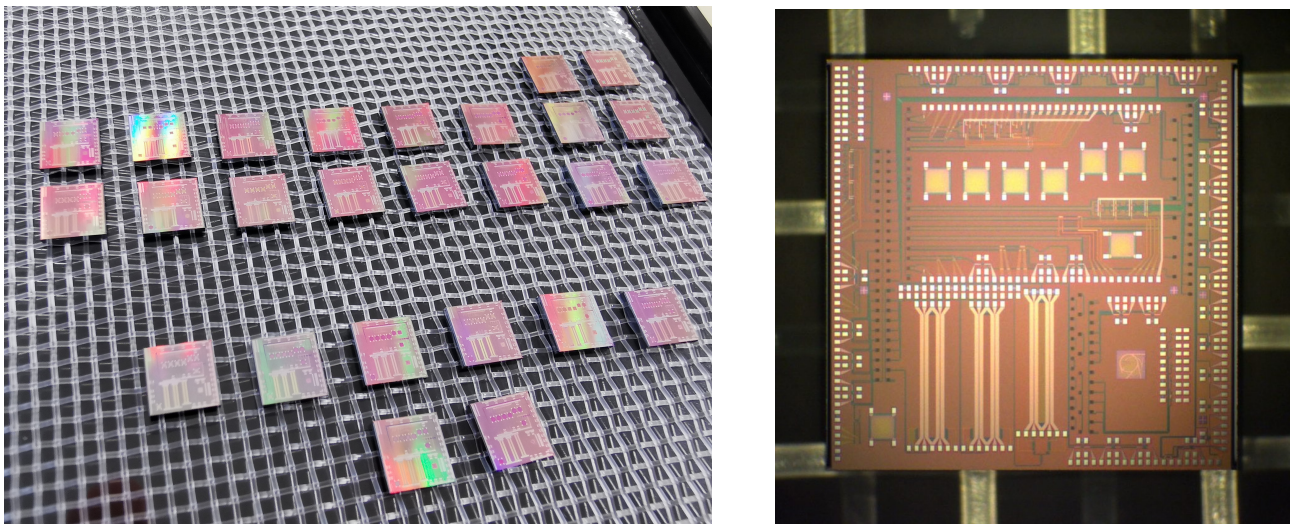

(a) **(b)**

Figure 4.1: (a) Photograph of one batch of Silicon Photonics chips that arrived at CERN in May 2020. (b) Bare SiPh chip (PICv2) under a microscope.

To ensure maximal utilisation of the space on the chip (die), the chip is divided into four independent sections. In order to use some of the areas of the chip, it is necessary to sub-dice the die (cut the die into smaller sections). Die sub-dicing is common practice in photonics integrated circuits. It involves using a mechanical saw or laser to cut through the wafer along predefined lines, marked with dicing markers.

In Figure 4.2, a schematic of the PICv2 divided into four sections is presented.

- Section #1 is the main section which is mainly used for radiation tolerance measurements on silicon photonics modulators. It includes 20 ring modulators and three Mach-Zehnder modulators. Three sides of the chip are used for the establishment of the electrical connections, while the left-hand side is used for the optical connection. On the left-hand side of Section #1, the array of 24 grating couplers is located.
- Section #2 contains five different Ge photodiodes and some basic photonics structures. This part of the chip can be used for the radiation tolerance measurements on photodiodes.
- In Section #3, structures for polarisation diversity tests are located. In order to use this part of the chip, sub-dicing is needed. Dicing markers are yellow crosses on the corners of the section, and they are included in the PIC layout during the design. In this section, optical connections are located on the left and right-hand sides, while electrical connections are on the top and bottom sides.
- Section #4 is the section with basic structures, such as ring modulators, waveguides and splitters, for operation on 1310 nm wavelength. For utilisation of this section, sub-dicing is necessary.

The section mainly used for the results presented throughout this thesis is Section #1, as illustrated in Figure 4.3. Along with Section #1, results on the photodiodes from Section #2 will be included in the thesis. Devices from the Sections #3 and #4, will not be covered.

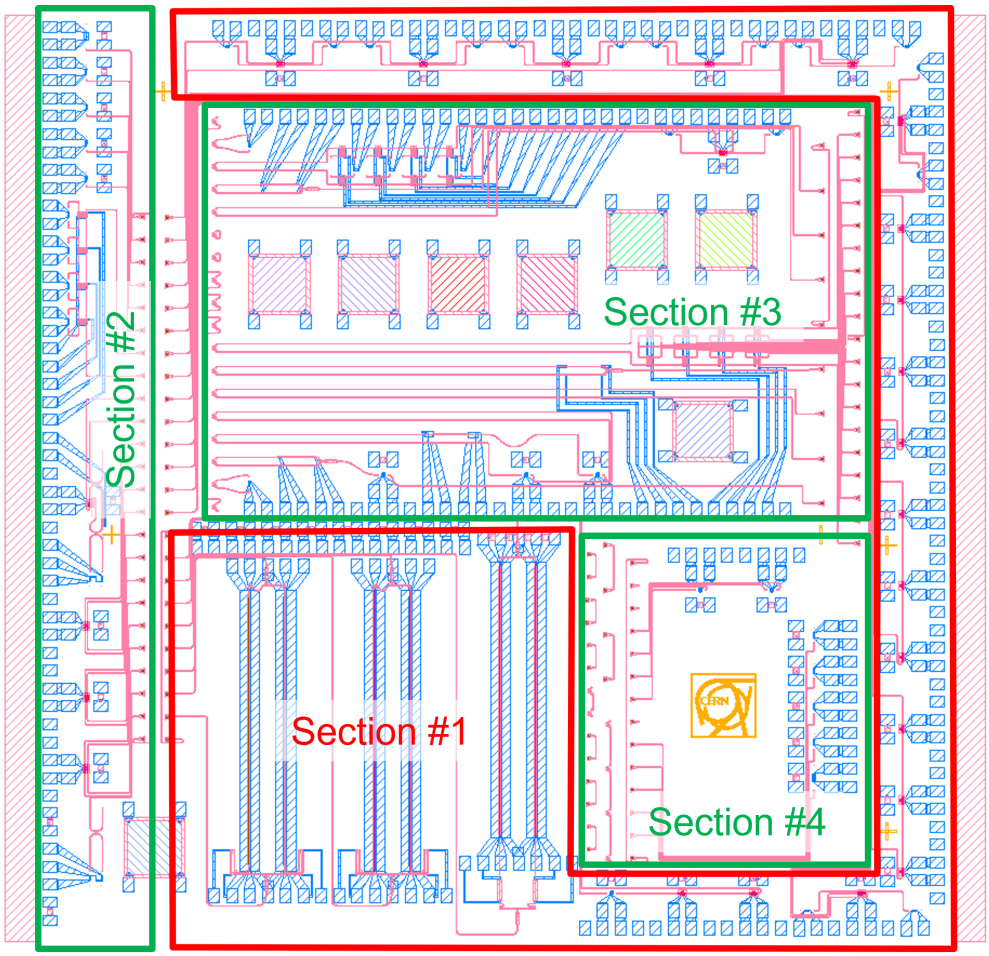

Figure 4.2: The layout of the PICv2 divides into four sections.

In Section #1, a total of 20 ring modulators equipped with micro-heaters are strategically positioned along the periphery of the chip. Additionally, three Mach-Zehnder modulators are placed in the bottom left corner. To ensure simultaneous and easy access to all devices, metallic bond pads are intentionally positioned near the top, bottom, and right-hand side edges of the chip. The bond pads have a pitch of 100 μm, allowing efficient machine assembly. On the left-hand side of the chip, an array consisting of 24 grating couplers is situated. These grating couplers have been designed with a pitch of 127 μm, a standard pitch of single-mode fibre arrays. Specifically, there are 12 input and 12 output grating couplers within this array, allowing access to all devices on the chip.

4.1.1 Ring modulators

The ring modulators integrated into the chip are organised into groups consisting of either three or four modulators, which are interconnected through a single bus waveguide. Each group shares a common input and output waveguide. Alternatively, individual input and output configurations are also utilised. All ring modulators are equipped with a micro-heater, although some of them are modelled with a drop port while others are not.

Figure 4.3 illustrates Section #1 with an enlarged part of the chip featuring a single ring modulator in a configuration with a drop port. Positioned on both sides of the ring modulator are Ge photodiodes (PD1 and PD2). Photodiode PD2 is responsible for receiving the optical power of the specific wavelength that is coupled into the ring modulator and subsequently extracted through

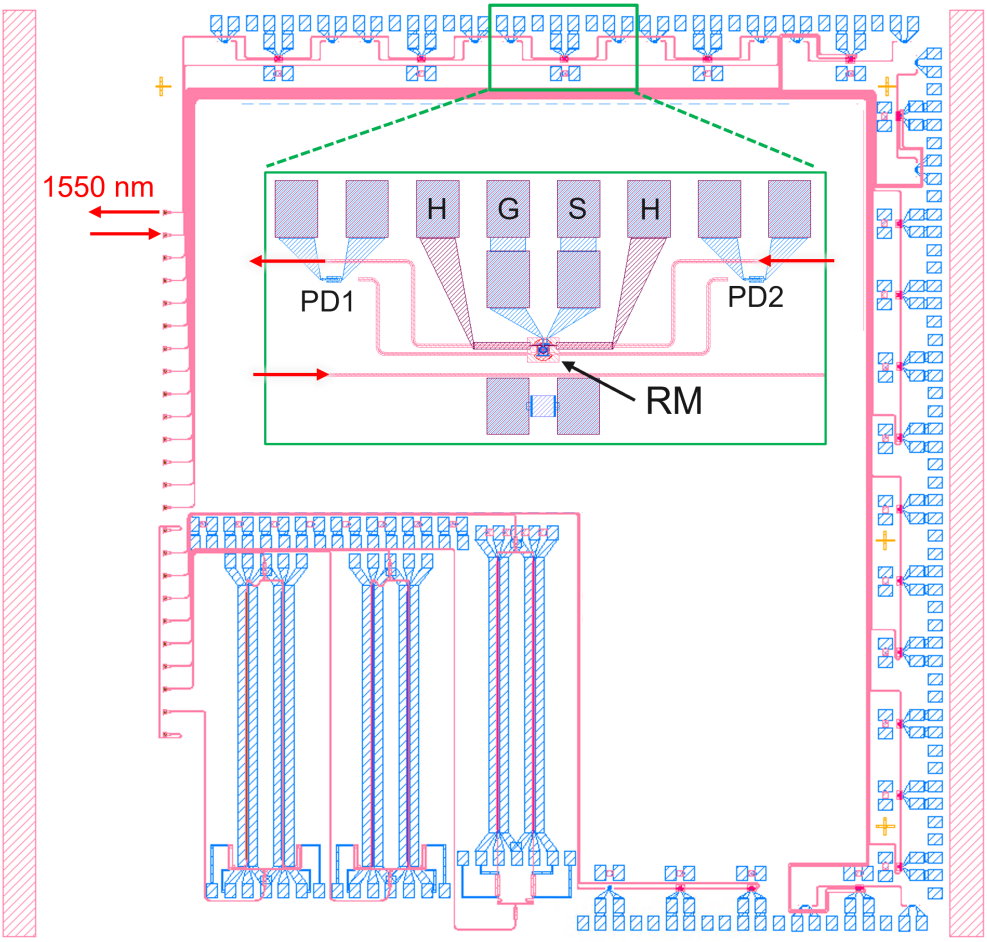

Figure 4.3: Layout of the Section #1 of PICv2 with an enlarged scheme of one ring modulator in drop port configuration and two photodiodes at each side of the RM. Modulation bond pads are surrounded by micro-heater bond pads and photodiode bond pads. H - heater, G - ground, S - signal

the drop port. On the other hand, PD1 is placed for symmetry purposes and solely detects any potential back reflections, if they exist. Within the enlarged image, the first and second bond pads correspond to the cathode and anode connections of the Ge photodiode, respectively. The third and sixth bond pads are dedicated to the micro-heater connections. Lastly, the fourth and fifth bond pads, which are high-speed pads, are linked to the cathode and anode of the ring modulator.

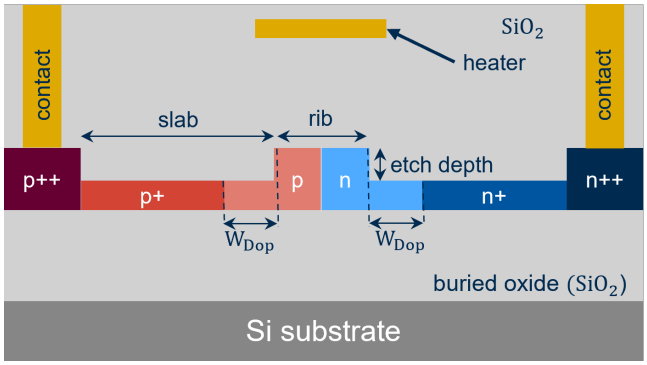

Figure 4.4: Cross-section of a ring modulator with a lateral pn-junction and tungsten micro-heater located above the rib.

Figure 4.4 illustrates a detailed cross-sectional view of the ring modulator, providing a concept of its internal structure. During the modelling of the chip and the devices, some geometrical dimensions such as etch depth, rib width, slab width, W_{Dop}, the radius of the ring, as well as the gap between the ring and the bus waveguide can be varied. Even though two etching depths are offered for the rib waveguides (shallow etch waveguide with 70 nm etching depth and deep etch waveguide with 160 nm etching depth), only the design of the deep etch RM is chosen. Shallow etching is not possible for these devices since the loss in the ring waveguide would be too high. A standardised rib width of 500 nm is chosen across all RMs to ensure confinement of the fundamental TE mode. The other parameters mentioned above have been varied, and their values for specific RMs are presented in Table 4.1.

In addition to the geometric parameters, the doping concentrations within the waveguide core may vary from one RM to another. The IMEC's platform provides two distinct levels of doping concentrations for each type of doping that can be used in the waveguide core. Those shall be referred to as high and low doping concentrations. The specific values of these doping concentrations have not been publicly disclosed by the foundry. However, it is expected that the values of rib doping should be in the range of $1 \times 10^{18}\text{cm}^{-3}$ [152]. The concentrations of the high contact doping (p++ and n++) and intermediate slab doping (p+ and n+) remain constant for all RMs, and they can not be altered during the production process.

Table 4.1: An overview of ring modulators' design parameters.

Name	**Core doping**	**Radius** (μ**m**)	$\mathbf{W_{Dop}}$**(nm)**	**Slab width (nm)**	**Through port gap (nm)**	**Drop port gap (nm)**
RM1	High	5	300	750	160	x
RM2	High	5	100	1000	160	x
RM3	High	5	10	1000	160	x
RM4	High	5	-10[1]	1000	160	x
RM5	High	5	-50[1]	1000	160	x
RM6	High	5	100	1000	170	x
RM7	Low	5	100	1000	160	x
RM8	Low	5	10	1000	160	x
RM9	Low	5	-10[1]	1000	160	x
RM10	High	5	100 (p++)[2]	1000	160	x
RM11	High	5	100	750	160	x
RM12	High	7.5	100	1000	180	x
RM13	Low	7.5	100	1000	180	x
RM14	High	5	100	1000	160	300
RM15	High	5	100	1000	160	160
RM16	High	7.5	100	1000	180	230
RM17	High	5	100	1000	160	220
RM18	High	5	100	1000	160	220
RM19	High	5	100	1000	160	220
RM20	High	5	100	1000	160	220

[1] Slab doping (both p+ and n+) is extended into the waveguide core.
[2] Contact doping (p++) is used instead of slab doping (p+) in the slab region.

For the ring radius, two values are taken into consideration, 5 μm and 7.5 μm, while for the

slab width, the values of 750 nm and 1000 nm are chosen. For the width of the low doping region in the slab (W_{Dop}), a variety of values were explored. Based on findings from [153], reducing the width of this region improves the radiation tolerance of Mach-Zehnder modulators to some extent. Accordingly, the W_{Dop} was selected to have values shorter than 300 nm. The majority of the RMs have positive values (300 nm, 100 nm and 10 nm) of W_{Dop} region, with a few exceptions. Three RMs have negative values, which corresponds with the fact that the doping of the slab (p+ and n+) is extended into the waveguide core by the value of $|W_{Dop}|$. During the irradiation tests, only ring modulators with W_{Dop} of 100 nm, 10 nm and -10 nm (i.e. all except RM1 and RM5) were tested. Further, one of the RMs (RM10) features a slab structure composed of 100 nm of p-doping and, adjacent to it, 900 nm of contact doping (p++) instead of slab doping (p+).

Finally, there are 13 RM with just one bus waveguide (just input and through port), and seven RM in configuration with a drop port, i.e. two bus waveguides (input, through, drop and add port). For the gap between the ring waveguide and the through port bus waveguide, there are three alternatives: 160 nm, 170 nm, and 180 nm. These values are carefully chosen in order to achieve critical coupling. For the gap between the ring waveguide and the drop port bus waveguide, values of 160 nm, 220 nm, 230 nm, and 300 nm are selected.

Upon careful examination of Table 4.1, it becomes evident that four RMs, denoted as RM17-RM20, exhibit identical parameters. These four RMs together form a four-channel Wavelength Division Multiplexing transmitter. The schematic representation of this WDM transmitter, based on four ring modulators, is illustrated in Figure 4.5. Notably, the four RMs share a common bus waveguide, which is equipped with two grating couplers (input and output), positioned at opposite ends. Despite sharing the same bus waveguide, the four RMs possess distinct drop port waveguides, each of which is terminated with photodiodes at both ends.

In order to ensure the smooth and efficient operation of the WDM transmitter, it is crucial for the resonant wavelengths of the individual ring modulators to be adequately separated. When the rings possess precisely identical radii, their resonant wavelengths tend to overlap. Therefore, it becomes necessary for the resonant wavelengths to be separated by a sufficient margin. With a ring radius of 5 μm, the Free Spectral Range measures ≈20 nm. Consequently, the spacing between the resonant wavelengths of two adjacent RMs should be ≈5 nm. To meet this requirement, the ring radii should be slightly varied one from the other. Specifically, a calculated difference of 24 nm between the ring radii is required to achieve the desired 5 nm spacing between the resonant wavelengths.

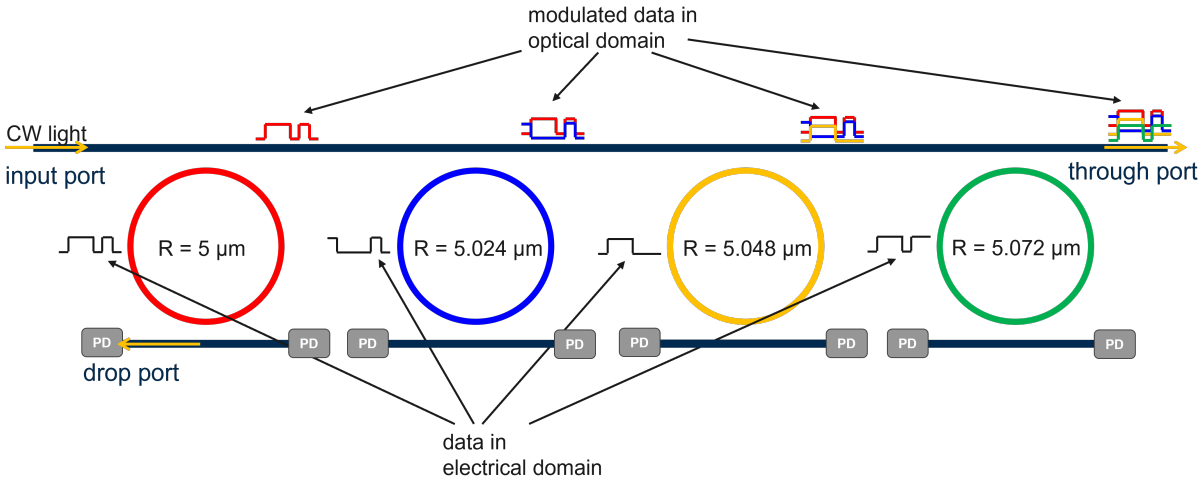

Figure 4.5: Schematic of four-channel WDM transmitter based on ring modulators.

4.1.2 Mach-Zehnder modulators

In Section #1, besides 20 RMs, there are three Mach-Zehnder modulators as displayed in Figure 4.6. The MZMs are built of two arms, both based on typical phase shifters (see Figure 2.6). The two arms are nearly identical in size, with a slight deviation to ensure they are not precisely in phase but rather operate around the quadrature point. Additionally, one portion of the arms incorporates a thermal phase shifter, allowing further adjustments of the phase shift to achieve the quadrature point. The high-speed input pads are arranged in a GSGSG configuration, where G denotes the ground pad, and S represents the signal pad.

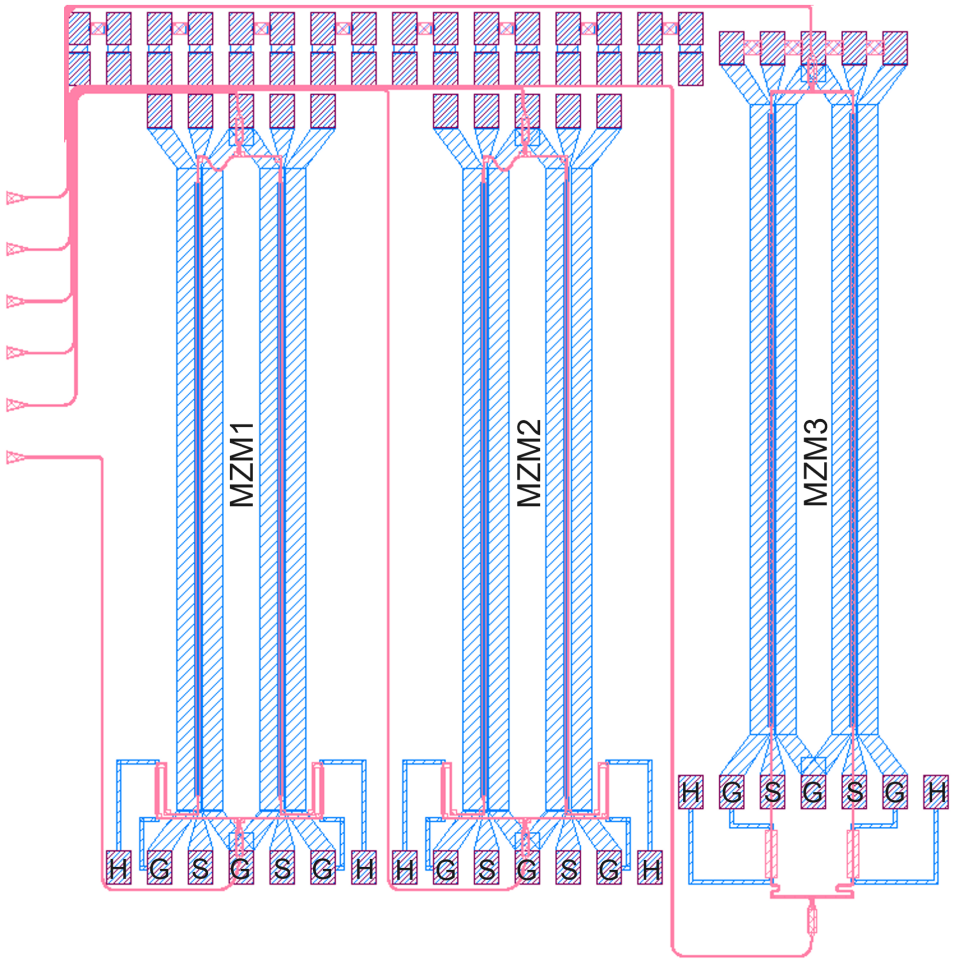

Figure 4.6: Schematic of Mach-Zehnder modulators. H - heater, G - ground, S - signal

Modulation in the Mach-Zehnder modulators is achieved through the utilisation of travelling wave electrodes. Each arm has a characteristic impedance of 50 Ω. In order to improve the modulator's bandwidth, the transmission line should be terminated with a 25 Ω-resistor, as suggested in [154]. MZM1 and MZM2 have floating 50 Ω resistors, which can be connected via bond pads if required. On the other hand, MZM3 has integrated 25 Ω-resistor between the signal and ground. For the measurements conducted in this thesis, MZM1 and MZM2 will not have floating resistors connected. However, due to the specific configuration of MZM3, the integrated resistor, in this case, will establish a connection between the ground and signal pads, enabling current flow. Consequently, the remaining travelling wave electrodes will function as resistors and experience heating. Accordingly, an additional phase shift will be induced in MZM3 due to the thermo-refractive effect.

Several dimensions remain consistent among all three MZMs, including rib width (450 nm), slab width (1275 nm), and length (1.5 mm). Moreover, the low doping concentration is employed for all the MZMs. The summarised design parameters of the MZMs are provided in Table 4.2. It is worth noting that MZM1 employs a shallow-etched phase shifter with an etching depth of 70 nm, while MZM2 and MZM3 utilise a deep-etched phase shifter with an etching depth of 160 nm. Furthermore, MZM1 and MZM2 have width of low doping (W_{Dop}) equal to 100 nm, while for MZM3, this width is set to 300 nm.

Table 4.2: An overview of Mach-Zehnder modulators' design parameters.

Name	Core doping	Length (mm)	W_{Dop} (nm)	Etch depth (nm)
MZM1	Low	1.5	100	70
MZM2	Low	1.5	100	160
MZM3	Low	1.5	300	160

4.2 Probing bare chips

After the arrival of the chips, it was necessary to do initial tests. The primary step involved testing all pn-junctions to assess their forward voltages. Since all pn-junctions on the chip are in fact the pn diodes, it was expected that there would be a specific voltage point, where a minor change in voltage would result in a substantial variation in current when forward-biased. To achieve this, each pn-junction, i.e. each modulator, was subjected to a range of biased voltages from 0 V to 1 V, using the Keithley 2400 Source Meter Unit (SMU). The approach was to place the bare PIC onto the probing station and carefully access the bond pads with the probes, as shown in Figure 4.7. The expectation was to observe a distinct change in measured current when the threshold of 0.7 V was reached. This phenomenon was consistently observed in all devices from one of the batches, validating their functionality. However, the same outcome was not observed in the other batch. Further investigation revealed that the devices or bond pads on the chips in this particular batch were short-circuited. Upon closer examination performed by IMEC, it was determined that the

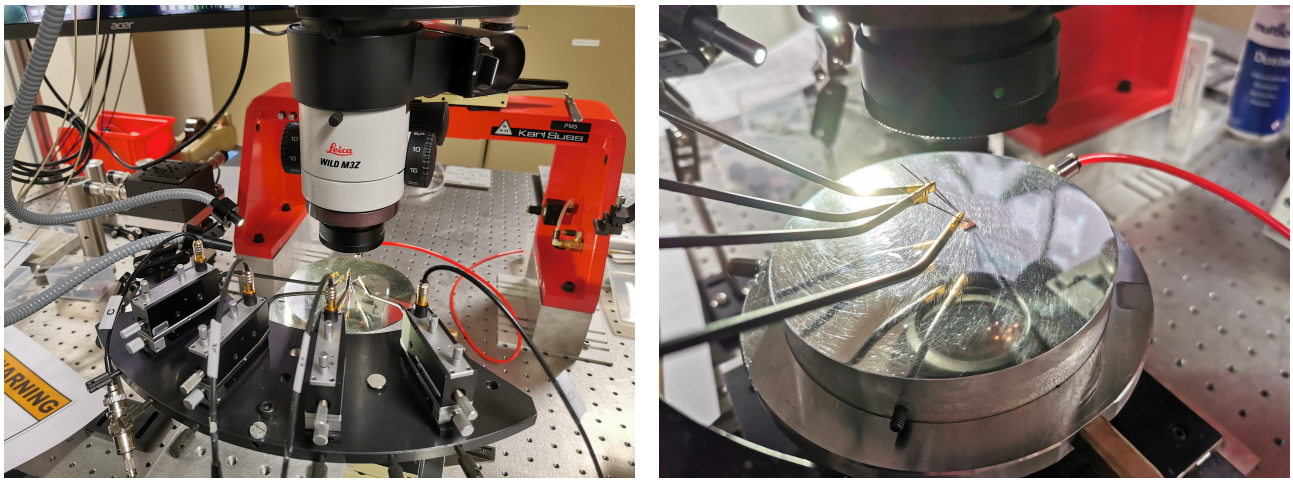

(a) **(b)**

Figure 4.7: (a) Photograph of a probing station with a single PIC on it. (b) Close-up of PICv2 under the probes.

second batch encountered production-related issues, leading to their defective state. Therefore, all following tests were carried out using chips from the first batch, given their reliable performance so far and the absence of initial defects.

4.3 Test board assembly

For achieving simultaneous access to different devices on the chip, a Printed Circuit Board (PCB) is used, along with the integration of optical fibre. The PCB, custom-designed and fabricated at CERN, offers convenient access to all the bonding pads through connectors, as depicted in Figure 4.8a. The chip is fixed to the PCB using a silver epoxy, and subsequently, gold wire bonding is performed to establish electrical connections using the ball bonding technique. The wire-bonding process is carried out by the company Hybrid SA [155]. Figure 4.8b presents a close-up view of the PIC assembled for the operation of Section #1 after wire bonding has been completed.

To enable optical access, a 24-channel glass fibre array pigtail is carefully attached to the PIC. The pigtail consists of two 12-channel ribbon single-mode (SM) fibres on top of each other, with a glass prism on one side and MPO/APC connectors on the other side. There is one MPO connector per ribbon. The glass prism has a 49° angle and a 127 μm pitch between the fibres in the tip of the prism. The alignment and placement of the fibre array onto the PIC were performed using Fineplacer Lambda as illustrated in Figure 4.9a. The prism was afterwards glued to the PCB next to the PIC and not directly to the PIC. An example of the fibre array successfully attached to the PIC can be observed in Figure 4.9b.

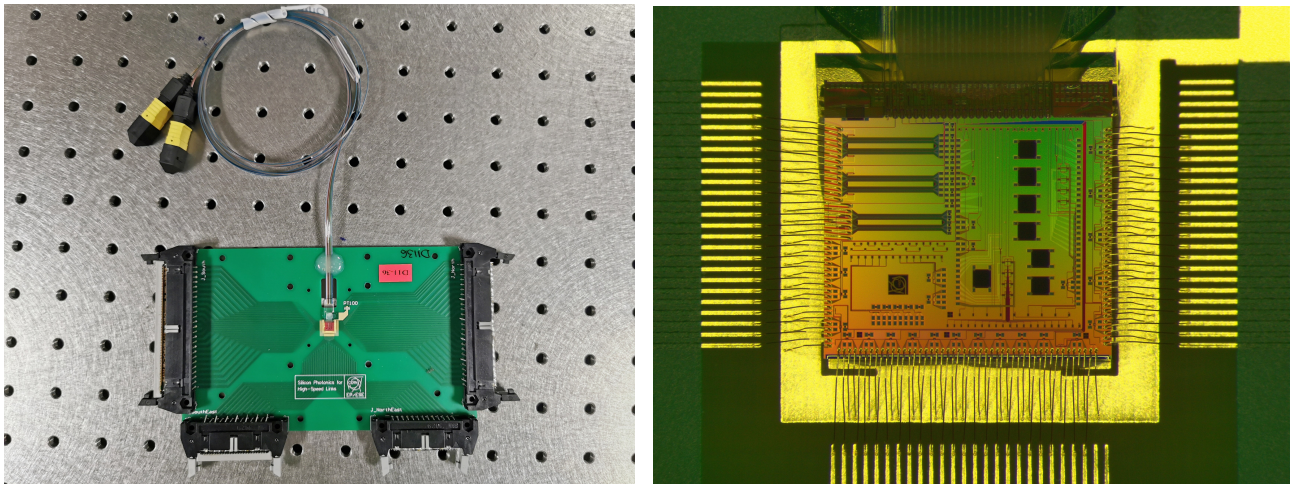

(a) **(b)**

Figure 4.8: (a) A fully assembled test board with a photonic chip wire bonded to a PCB and fibre array pigtail attached to it. (b) Close-up photograph of a PIC wire bonded for the operation of Section #1.

It is important to note that the images presented are associated specifically with the assembly of the test board designed for the operation of Section #1. However, depending on the specific requirements, the PCB assembly was adapted to alternative board configurations if needed.

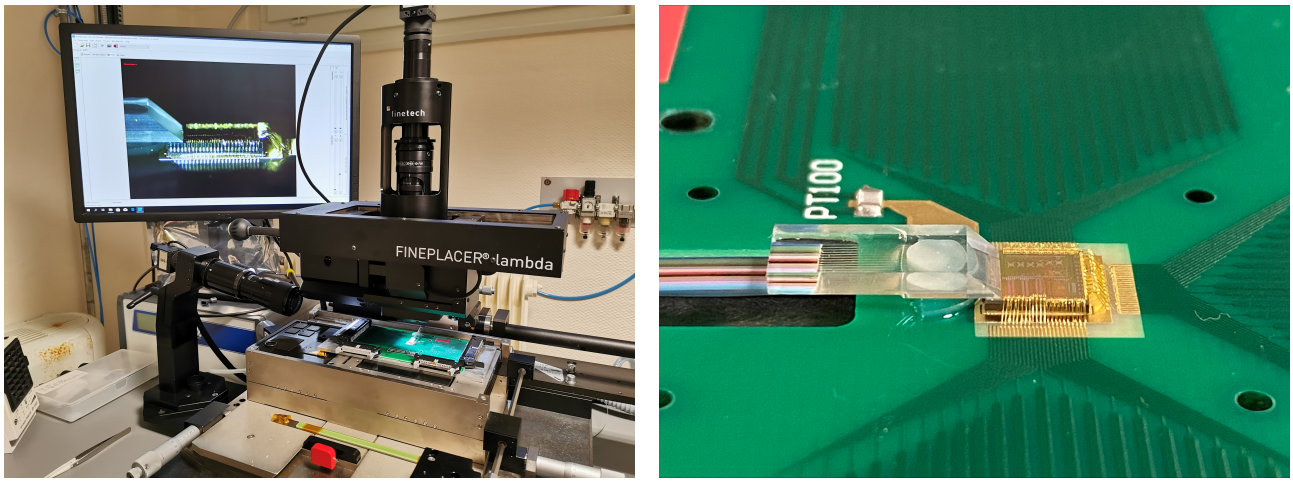

(a) **(b)**

Figure 4.9: (a) Photograph of a Fineplacer Lambda used for the alignment and the placement of the fibre array onto the PIC. (b) The close-up of a glass fibre array attached to a PIC.

4.4 Micro-heater characterisation

As previously indicated, all ring modulators are equipped with micro-heaters. The micro-heater is fundamentally a resistor made of tungsten (W) positioned approximately 1 μm above the ring waveguide. Figure 4.10 shows a 3D model of the ring modulator with the heater, where the heater is represented in red and the waveguides in pink. The heater forms an almost entire circle whose ends are connected to the copper (Cu) terminals (contacts). A voltage applied to the heater's terminals causes ohmic heating in the tungsten with the heat dissipating through the SiO_2, resulting in heating of the ring waveguide. Consequently, this process induces changes in the refractive index and the resonant wavelength of the ring modulator.

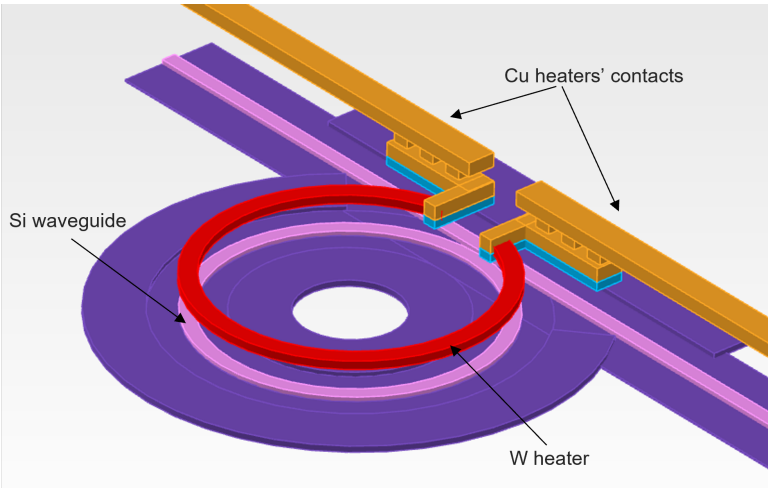

Figure 4.10: 3D illustration of the ring modulator with the tungsten micro-heater.

In order to assess the effectiveness of the heaters under investigation, a series of measurements were conducted to characterise their performance. The first step involved investigating the shift in resonant wavelengths in response to variations in temperature. A schematic of the experimental setup used for this particular measurement is depicted in Figure 4.11. A superluminescent diode (SLED) with a central wavelength of 1550 nm was used as an input light source. The light coming

from the SLED was coupled into the chip via grating couplers and the modulated light was decoupled back into an optical fibre connected to the Optical Spectrum Analyser (OSA), *Yokogawa AQ6370D*, used to record the transmitted optical spectrum. To ensure precise control of the temperature conditions during the measurements, the test board was placed inside a climatic test chamber, *CTS T-40/50*.

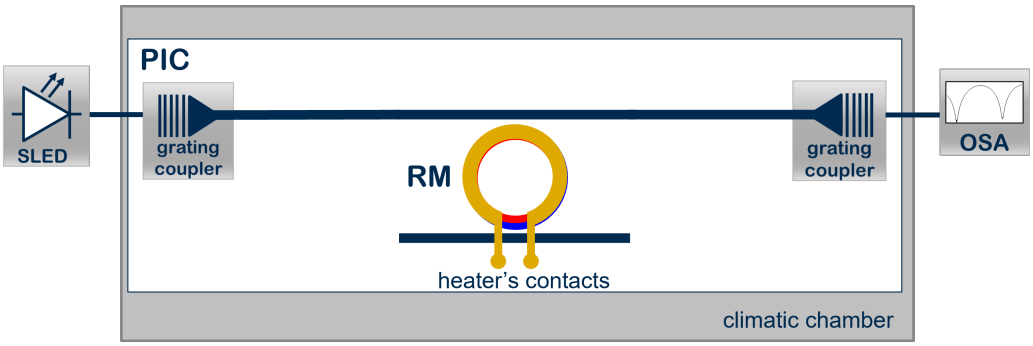

Figure 4.11: Schematic of the test setup for characterising the micro-heaters.

For this test, a range of temperatures from -10 °C to 30 °C was chosen since the glue used in the assembly of the fibre array was thermally stable in this range, and the power coupled into the chip will remain the same. For every step, an optical spectrum was recorded for every ring modulator separately and the value of the resonant wavelength was extracted. A temperature increase induces a shift of a modulator resonant wavelength towards longer wavelengths, as shown in Figure 4.12. The measurement was repeated on all the ring modulators for three different test boards and all the heaters have consistent characteristics with small variations up to 0.75 pm/°C from the mean value. The average measured shift of the resonant wavelength is linear with temperature and is equal to

$$\frac{\Delta\lambda_{res}}{\Delta T} = 71.75\,\text{pm/°C}. \tag{4.1}$$

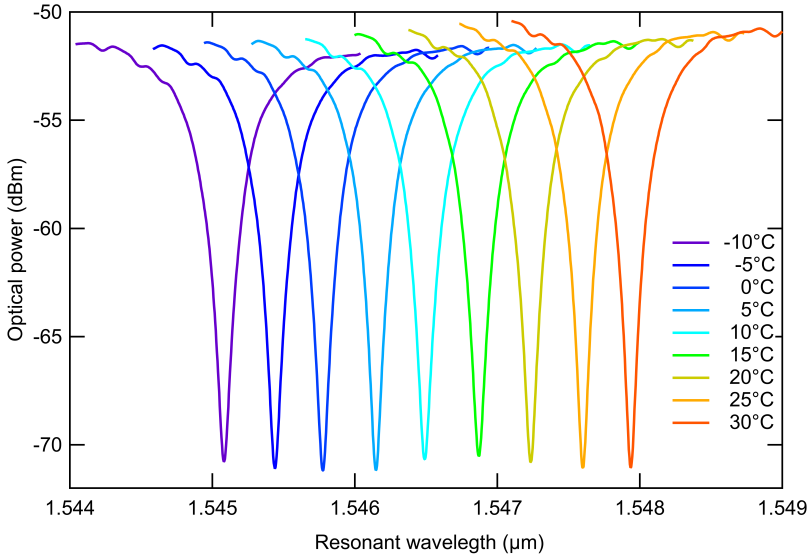

Figure 4.12: Shift of resonant wavelength of the ring modulator due to change of the temperature. A temperature increase generates a redshift of the resonant wavelength.

Further, the resonant wavelength shift related to the various voltage levels applied to the heater's contacts was investigated. Having in mind that the heater is the resistor with a resistance that is not constant, a current consumed by the heater was also recorded. Figure 4.13a shows the voltage and the current of the heater with respect to the resonant wavelength shift. The analysis indicates that the resonant wavelength shift does not exhibit a linear relationship with either voltage or current. According to [156], a resonant wavelength shift is expected to be linear with the power applied to the heater. In Figure 4.13b, the electrical power applied to the heater versus the resonant wavelength shift is presented. It has been measured that the efficiency of the heater is:

$$\frac{\Delta\lambda_{res}}{\Delta P} = 278\,\text{pm/mW}. \tag{4.2}$$

Along with the power, on the right axis of the same plot, the equivalent temperature versus the resonant wavelength shift is shown. It can be noticed that the two curves exhibit a linear trend. Furthermore, it should be noted that the temperature in this plot represents the temperature increase necessary for the shift and not the absolute temperature.

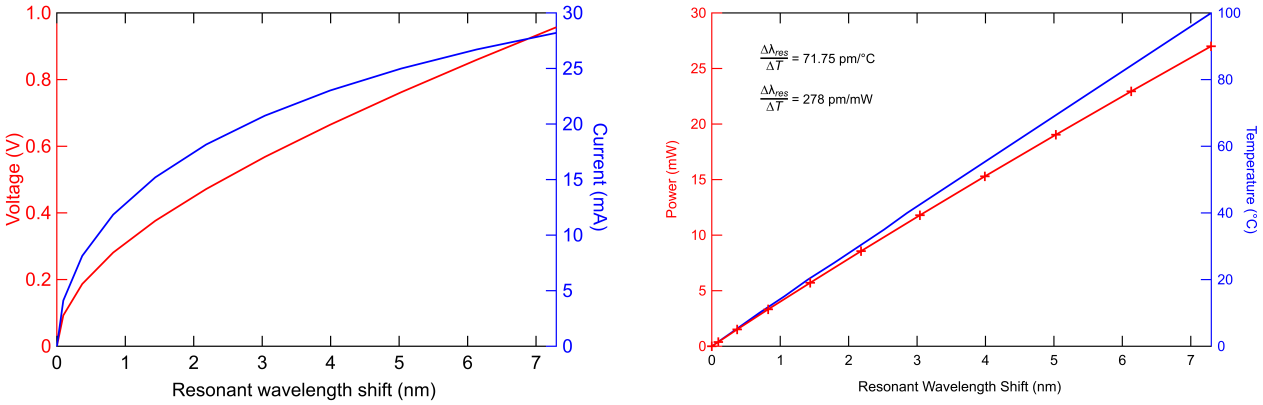

(a) **(b)**

Figure 4.13: (a) Voltage and current of the heater versus the resonant wavelength shift (b) Power of the heater and temperature of the ring modulator as a function of resonant wavelength shift.

To confirm the previous measurements, a simulation of the temperature distribution on a ring modulator cross-section was done. Since SiO_2 has very low thermal conductivity, there will be a significant temperature gradient between the heater and the waveguide, as shown by the device simulation in Figure 4.14. The simulation was done using a Lumerical HEAT solver [157]. The distribution of the temperature presented in Figure 4.14 is for the power of 15 mW on the heater. The temperature of the substrate was kept constant at 300 K. In this specific example, the temperature of the tungsten heater is approximately 100 K higher than the temperature in the waveguide.

For a more precise characterisation, the power applied to the heater was systematically varied over a range of 0 to 50 mW. During this experiment, the temperatures of both the tungsten heater and the Si waveguide were recorded. The resulting data is graphically represented in Figure 4.15a, where a clear linear correlation between the simulated temperature of the heater and the simulated temperature of the waveguide is observed.

Figure 4.15b illustrates the temperature of the Si waveguide as a function of the power applied to the heater, presenting both simulated and experimental results. It is evident that the experimental temperatures exhibit a slightly lower slope compared to the simulated ones. This difference can be attributed to the fact that the heater, situated above the waveguide, does not form a perfect ring and,

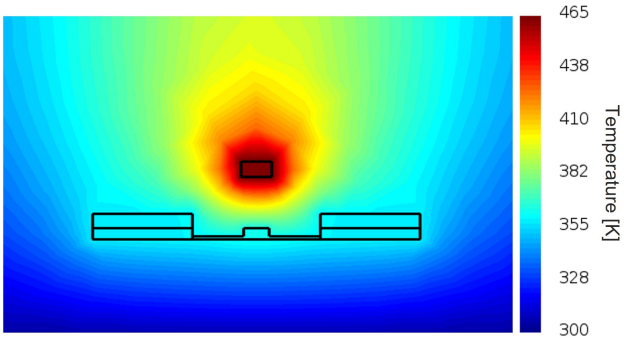

Figure 4.14: Simulation of the temperature distribution in the ring modulator cross-section for the power of 15 mW on the heater.

therefore, fails to cover the entire waveguide uniformly. As a result, the experimental temperatures represent an average value across the waveguide. On the other hand, the simulated temperatures specifically correspond to the region immediately below the heater. Thus, it was expected for the simulated temperature to be slightly higher compared to the experimental results due to a lack of appropriate modelling.

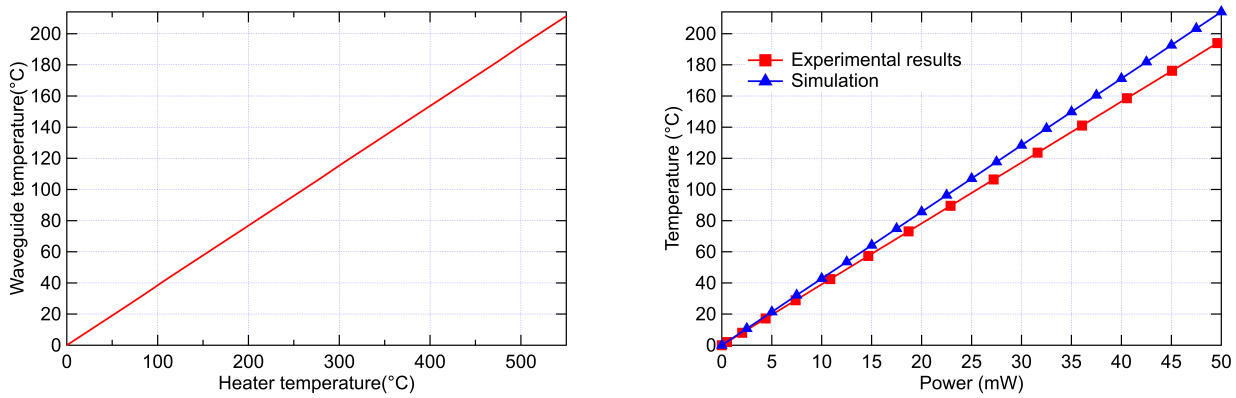

(a) **(b)**

Figure 4.15: (a) Simulated temperature of the ring waveguide as a function of the temperature of the heater. Due to the low thermal conductivity of the SiO_2, the temperature of the waveguide is significantly lower. (b) Comparison of the measured and simulated temperatures of the ring waveguide as a function of the power applied to the tungsten micro-heater.

An additional test was conducted to assess the micro-heaters in a controlled experimental setup. The primary focus of this test was to investigate potential cross-talk between two micro-heaters and establish if heating one micro-heater would induce a temperature rise in the adjacent ring modulator even when the latter is not actively heated. For this purpose, a single ring modulator was subjected to a power of 30 mW, resulting in a temperature increase of 120°C on the waveguide and 300°C on the heater. The resonant wavelength shifts of the adjacent ring modulators were measured to be 72 pm and 92 pm, respectively. These shifts correspond to temperature increases of approximately 1°C. Furthermore, the resonant wavelength shift of the ring modulator positioned at the opposite end of the chip was found to be 60 pm.

It is important to note that these temperature variations are considered negligible, as substantially higher temperatures will be employed for the planned experiments.

4.5 Pre-irradiation characterisation of SiPh devices

Prior to the beginning of the irradiation measurement campaigns, it was imperative to perform an assessment of the fundamental characteristics of the devices on the chip. To achieve this, the measurement setup scheme from Figure 4.16 was employed. A top scheme was used for the measurements on the MZMs, while a bottom scheme was utilised for RMs and photodiodes. A superluminescent diode with a central wavelength of 1550 nm was employed as the primary input light source for these measurements. In order to record the output spectra of the MZMs and RMs, an optical spectrum analyser was placed at the output. In the case of modulators, the main data is the recorded spectra, while for the photodiodes, the generated current was primarily measured. All the values are recorded over a period of 12 hours to ensure stability in measurement procedures.

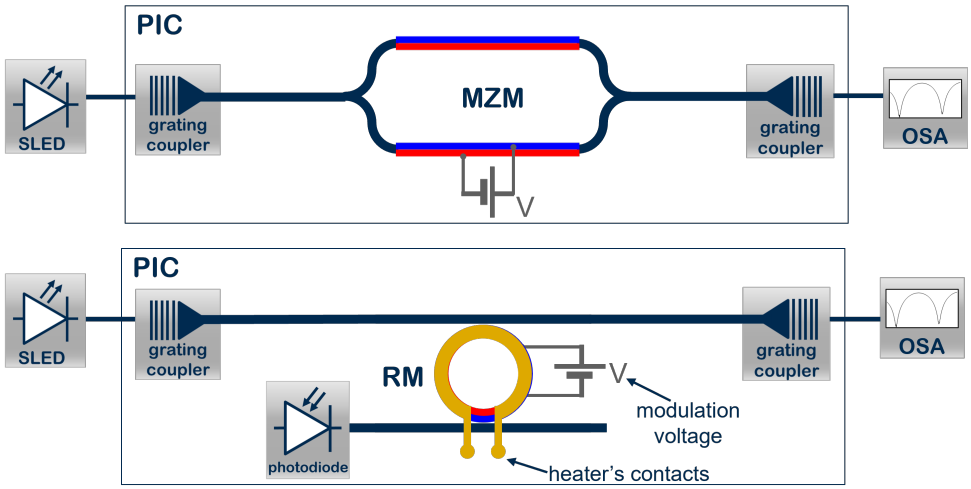

Figure 4.16: Schematic of the measurement setup used for the static characterisations of MZMs (top scheme) and RMs and photodiodes (bottom scheme).

Figure 4.17 presents the measured output optical spectra of Mach-Zehnder and ring modulators. Additionally, the acquired data underwent a fitting process aimed at determining fundamental parameters: specifically, the FSR and the central wavelength (λ_0) for MZMs, as well as the Full Width at Half Maximum (FWHM) and the resonance wavelength (λ_{res}) for RMs. The MZM spectra were fitted with the following function [147]:

$$P_{out} = P_0 + A \cdot \exp\left(-\left(\frac{\lambda - \lambda_{env}}{\sigma_{env}}\right)^2\right) \cdot \sin^2\left(\frac{\lambda - \lambda_0}{FSR} \cdot \pi\right) \tag{4.3}$$

where P_0 is the offset parameter, A is the amplitude, and λ_{env} and σ_{env} are the central wavelength and the width of the spectrum of SLED after grating couplers, respectively. λ_0 is the position of the spectrum minimum. It is important to highlight that the fitting operations were conducted within the linear domain (expressed in mW), whereas the data presented in Figure 4.17a is expressed in the logarithmic domain (dBm). Regarding RMs, the following Lorentzian fitting function was used:

$$P_{out} = P_0 + \frac{\left(\frac{FWHM}{2}\right)^2 \cdot ER}{(\lambda - \lambda_{res})^2 + \left(\frac{FWHM}{2}\right)^2} \tag{4.4}$$

where P_0 is the offset parameter, FWHM is the full width at half maximum of the fitted curve, ER is the difference between the maximum and the minimum of the optical spectrum in W, and λ_{res}

is the resonant wavelength of the RMs. Same as for the previous function, the spectrum has the Lorentzian shape in the linear scale, while data plotted in Figure 4.17b is in the logarithmic scale.

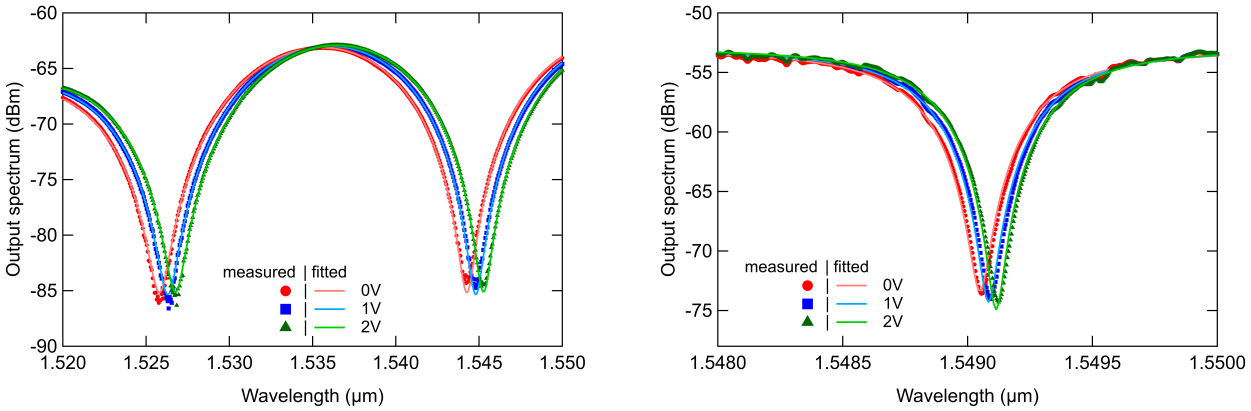

Figure 4.17: (a) Measured and fitted output spectra for MZMs at 0 V, 1 V, and 2 V of reverse bias voltage. (b) Measured and fitted output spectra for RMs at 0 V, 1 V, and 2 V of reverse bias voltage.

As explained in Section 2.2, applying a reverse bias voltage to the contacts of modulators results in a shift in spectral characteristics. For the RM, a resonance wavelength shift is called modulation efficiency and is quantified in picometers (pm). In the case of MZMs, this shift is named phase shift and is calculated as:

$$\Delta\phi = \frac{2\pi(\lambda_0(1\,V) - \lambda_0(0\,V))}{FSR \cdot L} \tag{4.5}$$

where L is the length of the modulator. The phase shift for Mach-Zehnder modulators is conventionally expressed in terms of phase shift per unit of length, specifically in units of π/mm. Figure 4.18a displays the experimental results of phase shifts observed in MZMs, while subjected to a 1 V and 2 V reverse bias. It can be noticed that the shallow-etched MZM1 has a phase shift of approximately $38 \cdot 10^{-3}\,\pi$/mm for 1 V bias voltage, while it is $70 \cdot 10^{-3}\,\pi$/mm for 2 V bias. The deep-etched MZM2 shows a higher phase shift of $53 \cdot 10^{-3}\,\pi$/mm and $98 \cdot 10^{-3}\,\pi$/mm for 1 V and 2 V of bias voltage, respectively. The higher phase shift is expected in deep-etched MZMs because of the better wave confinement. [158] The deep-etched MZM3 is a special case where part of the phase shift is induced by the thermo-refractive effect because of its configuration. Total phase shift induced by both the thermo-refractive effect and the free-carrier plasma dispersion effect is $0.12\,\pi$/mm and $0.38\,\pi$/mm for 1 V and 2 V bias voltages, respectively. In this stage of measurement, it was not possible to distinguish what percentage of the phase shift is due to which effect.

Figure 4.18b show the modulation efficiency of all 20 RMs when reverse biased with 1 V and 2 V. High doping ring modulators have clearly higher modulation efficiency than the low doping ones. For the 16 high doping ring modulator, the modulation efficiency in the range of 32 to 40 pm is measured with 1 V of reverse bias, while 63-73 pm is measured with 2 V. Four low doping RMs have modulation efficiencies in the range of 14 to 19 pm for 1 V and 25 to 36 pm for 2 V.

In addition to phase shift, a free spectral range for MZMs was measured, and it is equal to 18.5 nm for MZM1 and MZM2, while MZM3 has an FSR of 13.9 nm. One more parameter that can be calculated for MZMs is the voltage necessary for the phase shift of π i.e. V_π. Calculated V_π for the two MZMs with different etching depths is presented in Figure 4.19. Since deep-etched MZM has a larger phase shift, less voltage is necessary to achieve the shift of π. This value is calculated

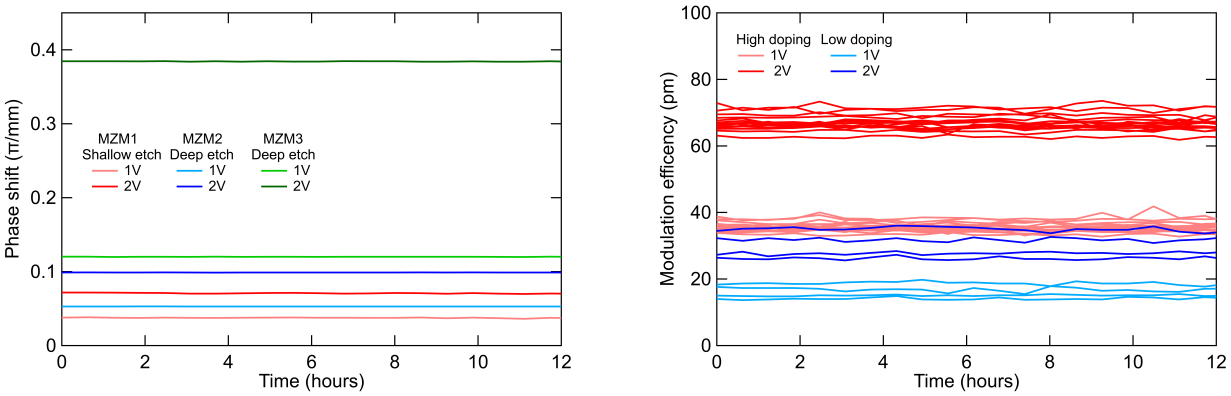

(a) **(b)**

Figure 4.18: (a) Measured phase shift of MZM when reverse biased with 1 V. (b) Measured modulation efficiency of RMs while reverse biased with 1 V.

to be 12.6 V for deep-etched MZM2, and 17.7 V for shallow-etched MZM1. The V_π parameter for MZM3 was not calculated due to the complexity of its phase shift and its non-linear relationship with applied voltage.

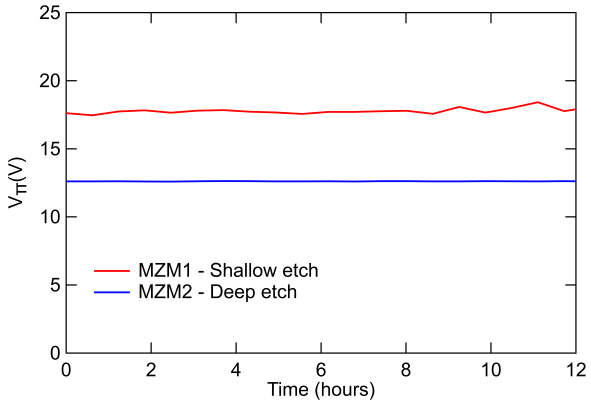

Figure 4.19: The measured V_π for the MZM1 and MZM2 over time.

The measured figures of merit for RMs are FSR, extinction ratio (ER), quality factor, and V_π. The free spectral range was measured to be around 19.3 nm for all the rings with a radius of 5 μm, and about 13 nm for RMs with a radius of 7.5 μm. The extinction ratio of RMs is in the range of 5 dB to 25 dB with no specific correlation between the ER value and the RM parameters. Figure 4.20a presents a measured Q factor. For most RMs, the Q factor ranges from 1500 to 2500. However, for some specific RMs, it goes up to 4500. As for a V_π, most of the high doping RMs have V_π of approximately 260 V. The two RM with high doping and ring radius of 7.5 μm, have V_π of 180 V, since their FSR is smaller. The low doping RMs have V_π in the range of 430 V to 700 V, because of their low modulation efficiency.

In addition to the modulators, characterisation was conducted on five Ge photodiodes within the PICv2, two lateral PIN (LPIN1-2) and three vertical PIN (VPIN1-3) photodiodes. The primary parameter under investigation during this characterisation process is the dark current. The measurement of dark current involved measurements taken in the absence of optical power from the SLED when the reverse bias voltage of 1 V is applied across the photodiodes. The results over time

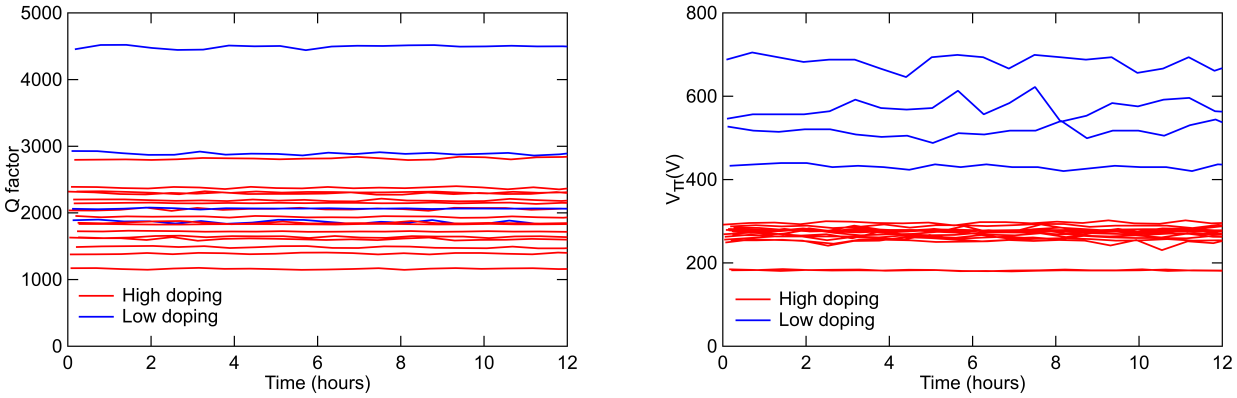

(a) **(b)**

Figure 4.20: (a) The measured Q factor of the four low doping and 16 high doping RMs over time. (b) The measured V_{π} of the four low doping and 16 high doping RMs over time.

are presented in Figure 4.21. The recorded dark current values for four photodiodes fall within the range of 10 to 25 nA, aligning with acceptable values reported in literature [159], [160]. Photodiodes with dark current values below 0.1 μA are generally considered to exhibit satisfactory performance.

However, one of the photodiodes, LPIN1, deviates from the expected range, displaying a dark current of approximately 0.32 μA. This observation is unexpected, especially given that the same measurements were repeated on multiple dies, yielding consistent results across all samples. The anomalous dark current in LPIN1 may raise concerns, particularly in the context of radiation hardness, and it will be closely monitored throughout the irradiation tests.

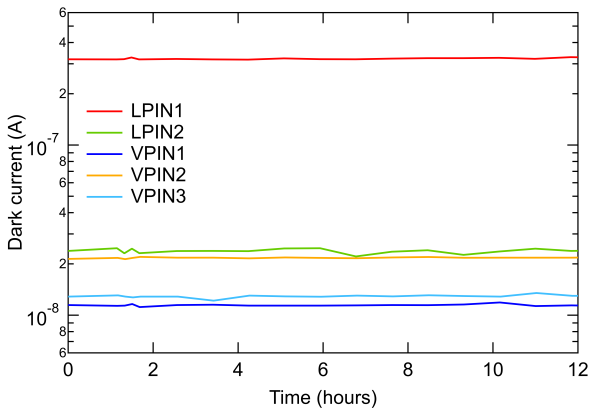

Figure 4.21: Measured dark current of Ge photodiodes over time.

Chapter 5

Evaluation of radiation damage due to TID in SiPh devices[1]

Devices and components installed in the inner-most detectors of the HL-LHC will have to withstand a total ionising dose of at least 10 MGy. For the evaluation of the radiation-hardness of the SiPh devices on the ionising radiation, 3 X-ray tests were conducted with different dose rates and TIDs. Several samples were irradiated with 10 keV X-rays at the EP-ESE Irradiation System [161] at CERN. Results from these tests divided into Sections according to the type of device (modulators or photodiodes) will be presented in this chapter. Results on waveguides are presented together with modulators.

5.1 SiPh modulators

It has been reported in the literature [148], [149], [162]–[164] that MZMs have radiation tolerance up to a few hundred kGy. However, the RMs were not subjected to this sort of exposure and testing. The novel MZM and custom RM designs were first exposed to ionising radiation. The X-ray machine (Seifert RP149) was used to irradiate the samples. It has a vacuum tube with a tungsten target that produces X-rays with an energy spectrum peaking at 10 keV. The maximum power supply voltage of the tube is 50 kV, and the maximum current is 60 mA [165]. Depending on the voltage and the current of the tube, and the distance from the target to the sample, the dose rates can vary from 0.5 Mrad(SiO_2)/h to 10 Mrad(SiO_2)/h [161].

5.1.1 First X-ray test - initial evaluations

In August 2020, the first X-ray test was conducted, focusing on Section #1 of the chip. The primary objective of this test was to identify the amount of radiation damage based on the geometric parameters of the modulator. The experimental setup, as depicted in Figure 5.1, can be divided into two pathways: the optical pathway, denoted in yellow, and the electrical pathway, featuring blue schematic blocks.

[1] Parts of this chapter are published in: **M. Lalović et al.,** "*Ionizing Radiation Effects in Silicon Photonics Modulators,*" in IEEE Transactions on Nuclear Science, vol. 69, no. 7, pp. 1521-1526, July 2022, doi: 10.1109/TNS.2022.3148579. *and* **Lalović, M. et al.** "*Thermal Annealing in Silicon Photonics Ring Modulators.*" Journal of Instrumentation 18, no. 03 (March 2023): C03028. doi: 10.1088/1748-0221/18/03/C03028.

A *Thorlabs* SLED with a central wavelength of 1550 nm, an optical bandwidth of 90 nm, and an optical power of 2 mW, regulated by a *Pilot PC 500* laser diode controller, was the main optical source in the test. The light was guided through a single-mode optical fibre to a manually operated polarisation controller for maintaining the amount of optical power coupled to the PIC maximised. Next, the light is split into two equal parts, with one directly guided to the *JDS Uniphase SB Series* optical switch and the other undergoing depolarisation before being directed to the switch. The output of this switch is 12 single-mode fibres that correspond with 20 Ring modulators, 3 Mach-Zehnder modulators and one optical shunt. Any of the 12 channels can be connected to depolarised or polarised light depending on the switch state. However, just one channel at a time will receive the optical signal. Depolarised light was utilised for measuring the transmitted optical power, as slight movements of the optical fibre could induce fluctuations in the optical power. Consequently, the impact of radiation on the output optical power was isolated from the fibre movements. On the other hand, polarised light was employed for evaluating the optical spectrum and associated figures of merit. At the output of the PIC, the 12 single-mode optical fibres were linked to a second *JDS Uniphase SB Series* optical switch. Subsequently, the output light was divided into two equal parts, one directed to an *Agilent 8163B* Optical Power Meter (OPM), and the other to a *Yokogawa AQ6370D* Optical Spectrum Analyser (OSA).

For the purpose of establishing electrical connections between the PIC, three source meters (*Keithley 2410 Source Meter*), one power supply (*Keysight E3648A DC power supply*), and a multichannel electrical switch (*Keysight 34970A*), a routing board was employed. Two source meters were used for biasing the modulators, while one source meter and one power supply were utilised for biasing the micro-heaters. The electrical switch was configured so that each channel could toggle between the measure and idle states. In the measure state, the DUT (device under test) is connected to the measurement bias voltage and in the idle state to the idle bias voltage. In the top left corner of Figure 5.1, a simple schematic of how the electrical switch is implemented with the modulators (represented with a diode symbol) is shown. At any given moment, only one DUT at most was connected to the source meter designated for measurement, while all other devices were connected to the idle source meter. This approach allowed for uninterrupted measurement of the response of an individual device. During the application of a measurement voltage to a modulator, optical spectrum, optical power, and modulator current were recorded.

Since more than one ring modulator can be on the same bus waveguide, their resonant wavelength will overlap. In that case, to record the spectrum of the specific RM, it is necessary to heat that RM to separate its resonant wavelength from the others. Hence, one micro-heater will be connected to the bias voltage, while the others will be kept on the idle voltage.

All instruments used in the setup are connected in parallel via GPIB cables and further connected to the PC via a *National Instruments* GBIP-to-USB converter. The procedures for controlling the instruments are written in Igor Pro [166]. The code used for recording all the data and the functions for further analyses were also written in Igor Pro. The measurement procedure consisted of measuring the spectra of MZMs, RMs, and the shunt and measuring the optical power of MZMs and shunt. The measurements were automated and repeated during the irradiation in an infinite loop. One measurement loop for measuring all the devices took approximately 30 minutes, implying that every value was recorded with a frequency of 30 minutes.

All instruments stacked in a rack and connected to the PC were placed next to the irradiation cabinet, as presented in Figure 5.2a. The cabinet acts as a shield to protect the external environment and instruments from the scattered X-rays. The board with the PIC on it was placed inside the cabinet under the X-ray tube, as given in Figure 5.2b. The centre of the chip was aligned to the centre of the beam with the help of the red laser pointers. The distance between the chip and the X-ray

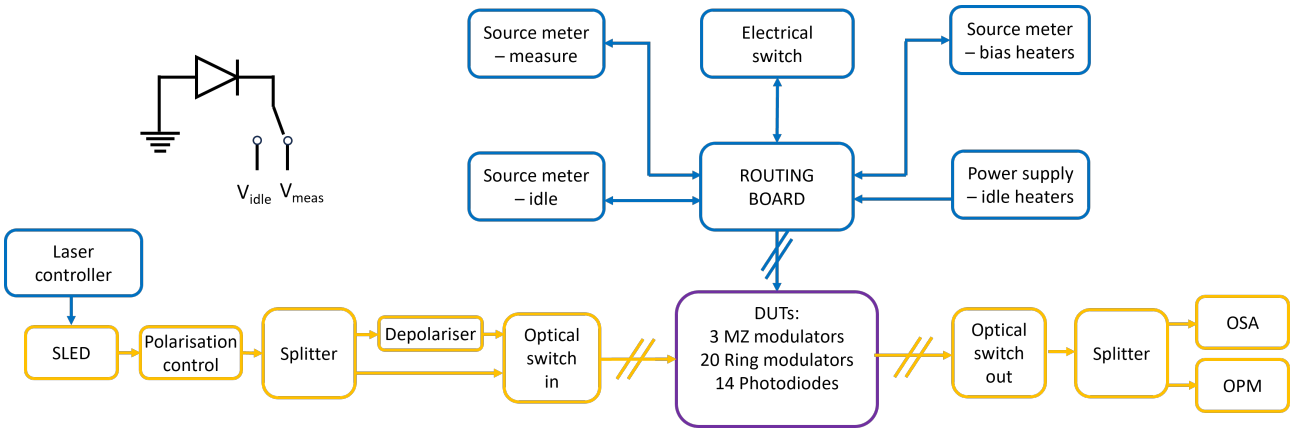

Figure 5.1: Scheme of the setup used for the first x-ray test conducted in August 2020. The test's main objective focused on Section #1 of the chip and the different modulators' designs present on the PICv2.

tube was set to 50 mm. At this height, the beam diameter was uniform up to 5 mm in the x-direction and 10 mm in the y-direction. Since the area of Section #1 is 4 mm by 5 mm, the dose delivered to the chip was uniform all over the area. The power supply voltage of the tube was 40 kV, and the current was 50 mA. The dose rate was 13.45 Gy^2/s (4.84 Mrad/h) with the maximum variation up to ±9.44%. The chip was exposed to 4.5 MGy of TID. During the irradiation, the temperature of the metal plate below the PCB was kept at 25°C.

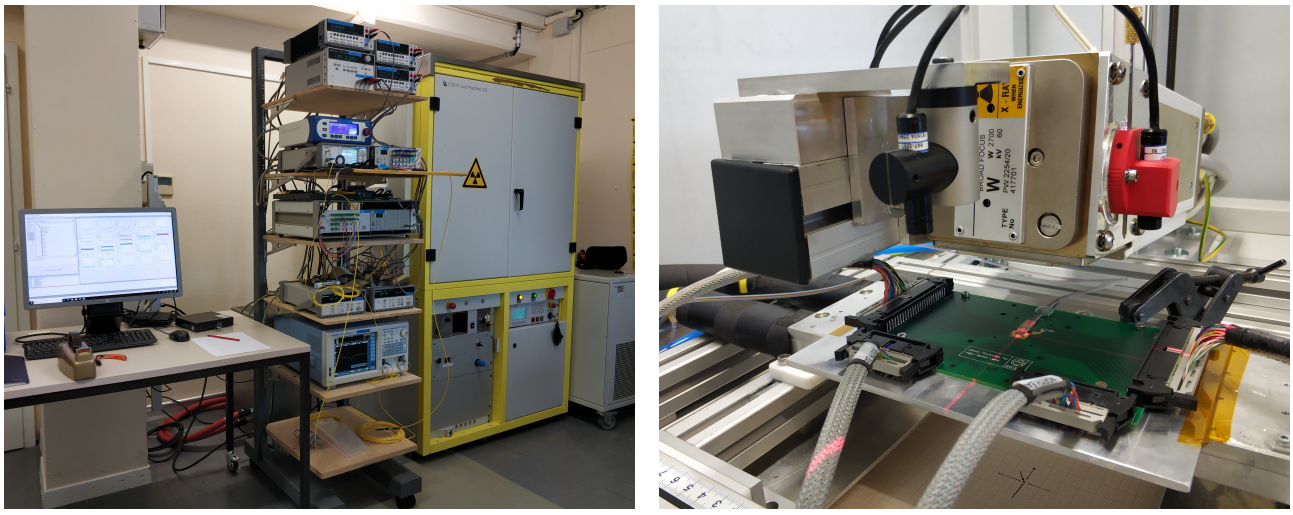

(a) **(b)**

Figure 5.2: (a) The picture of the measurement setup and the PC installed in the radiation-free area next to the irradiation cabinet at the EP-ESE irradiation facility at CERN. (b) The PCB board with the PICv2 was installed inside the irradiation cabinet and aligned to the beam centre with the red laser pointers. The X-ray tube was precisely set to 50 mm above the chip.

The measurement for this experiment was conducted in two distinct phases. In the initial phase, the measurement loop was initiated at the same time as the X-ray beam. Data acquisition occurred at 30-minute intervals throughout this phase. Afterwards, following the end of the X-ray beam, data recording continued for a duration of 75 hours at the same intervals to monitor potential post-irradiation effects, including additional degradation or annealing phenomena.

[2]The reference material for TID throughout the thesis is SiO_2.

Adjacent to the PIC on the PCB, a PT100 sensor was strategically positioned for the purpose of temperature monitoring. This sensor provided a reliable approximation of the thermal conditions on the DUT board throughout the whole experiment. As illustrated in Figure 5.3, a consistent temperature of 24.2°C was maintained during the irradiation phase, with a marginal increment of 1°C observed in the post-irradiation phase. It should be noted that between irradiation and post-irradiation measurements, the setup was moved from the room with the X-ray machine to another laboratory. The small discontinuity in temperature is due to this relocation.

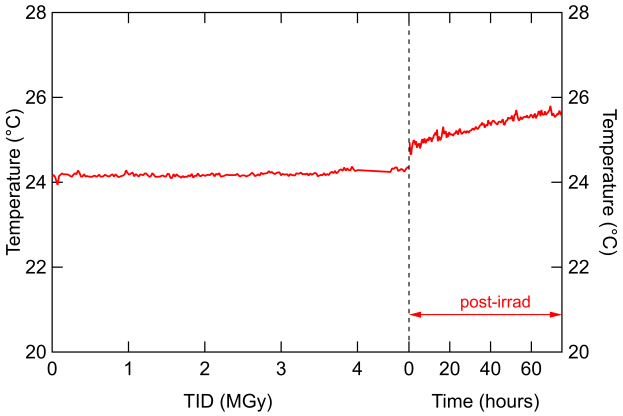

Figure 5.3: Temperature of the DUT board during the irradiation and post-irradiation phase.

5.1.1.1 Mach-Zehnder modulators

Prior to the PICv2 design, Mach-Zehnder modulators were included in the PICv1 design. Their performance characteristics can be found in literature [147]–[150], [153], [158], [162], [167]. However, the PICv2 now integrates a novel and enhanced MZM design. In the first X-ray irradiation test, only two MZMs were subjected to measurement, as the experimental setup encountered difficulties in measuring the third modulator. Throughout the experiment, the DUT was subjected to reverse biasing of 0 V, 1 V, or 2 V, while simultaneously recording optical spectra and optical power. All other devices on the chip were held at an idle voltage with an average of 1 V. The reported modulation efficiencies are the resulting phase shift when 0 and 1 V bias voltages are applied to the modulator contacts. Moreover, these values are normalised to the value at the beginning of the test.

The two MZMs subjected to measurement share identical geometric parameters, both possessing W_{Dop} width of 100 nm and differing only in etching depth. Figure 5.4 illustrates the normalised modulation efficiencies during the irradiation for these MZMs. A degradation in modulation efficiency is observed as the TID increases, displaying a similar trend for both MZMs. The shallow-etched MZM exhibits a slightly better response compared to the deep-etched counterpart. Following irradiation to a dose of 4.5 MGy, the modulation efficiency of the shallow-etched MZM reduced to approximately 70% of its initial value, while the efficiency of the deep-etched MZM decreased to approximately 57%. As it was foreseen, the MZM with a thicker slab was more radiation resistant than the one with a thinner slab.

In the post-irradiation phase of the experiment, the modulation efficiencies for both MZMs continued to degrade, reaching values of 58% and 45%, respectively. Nevertheless, due to the deep-etched MZM's initially higher absolute value of phase shift and its relatively similar modulation efficiency after irradiation, the deep-etched MZM exhibits a higher absolute value of phase shift at the end of the test.

5.1.1.2 Ring Modulators

The influence of various design parameters on the radiation tolerance of ring modulators is investigated. The obtained results are categorised based on factors such as the doping concentration of the pn-junction, ring radius, width of the p and n doping in the slab (W_{Dop}), the doping level of the slab, temperature, and other distinguishing device characteristics. During the experiment, the DUT was subjected to reverse biasing of 0 V, 1 V, or 2 V, while simultaneously recording optical spectra and optical power. All other devices were maintained at an idle voltage averaging 1 V. All modulation efficiencies reported in the following are measured as the difference in resonance wavelengths when 0 and 1 V bias voltage is applied to the ring modulators. These values are then normalised relative to the value at the beginning of the test.

The ring modulator under the test was thermally heated to a level where its resonant wavelength significantly differed from those of other RMs on the same bus waveguide. In this first X-ray test, temperatures were not precisely selected. Although precise temperatures were not strictly defined, a bias voltage of 1 V was applied to the heaters for all ring modulators except RM11, where a 0.65 V bias was employed. Additionally, RM17-RM20 were maintained at ambient temperatures. RM temperatures were calculated based on the specific heaters' thermal efficiencies defined during the pre-irradiation characterisations. While one ring modulator was subjected to heating, the heaters of the remaining devices were held at 0 V, thus maintaining room temperature conditions.

Regarding the impact of the heater on the dose delivered to the pn-junction, after calculation based on the Beer–Lambert law using tungsten as material and 10 keV X-rays, the additional attenuation due to the heater is below 10%, therefore negligible. The heater is 600 nm wide, and it covers the whole rib region and a small portion of the low doping slab. The rest of the slab is not covered by the heater, and the dose delivered to this part of the slab will be the same as in the case of structures without a heater. However, since all RMs on PICv2 do have heaters, for comparison among each other, they will receive the same amount of radiation.

Doping concentration

IMEC's Multi-Project Wafer platform provides access to two distinct doping concentrations, high and low, with specific quantitative values undisclosed. However, it is established that the high doping level is approximately ten times higher compared to the low doping level. Figure 5.5

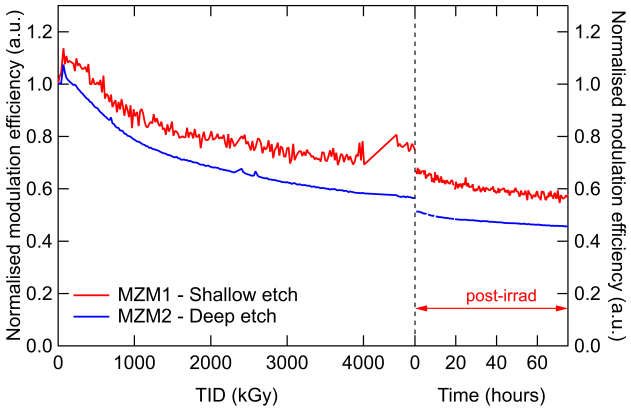

Figure 5.4: Normalised modulation efficiencies of MZMs with different etching depths during the irradiation up to 4.5 MGy and the post-irradiation measurements.

illustrates the normalised modulation efficiencies of RMs with different doping concentrations. Figures 5.5a and 5.5b respectively display the outcomes for RMs with radii of 5 μm and 7.5 μm. These RMs share identical design parameters, differing solely in the doping concentrations and radii. Precisely, they possess a doping width (W_{Dop}) of 100 nm, a slab width of 1000 nm, and a through-port gap of 160 nm. Both the high and low doping RMs were heated to 120°C and 140°C, respectively, for approximately 40 seconds every 30 minutes. During this X-ray test, sporadic problems with data acquisition within the measurement loop were encountered, resulting in the presence of several outlier points in the presented curves.

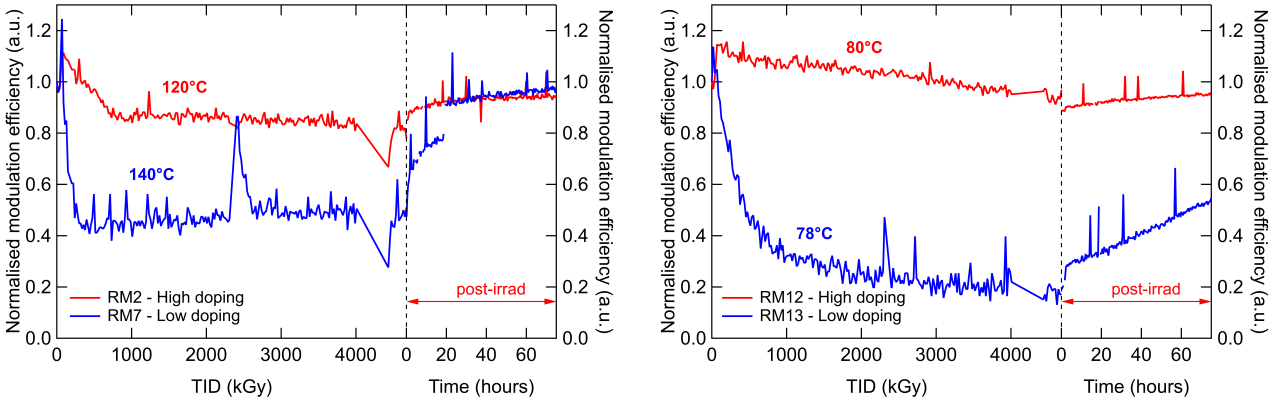

(a) **(b)**

Figure 5.5: (a) Normalised modulation efficiency of RMs (RM2 and RM7) with a radius of 5 μm for different doping concentrations of the pn-junction during the irradiation up to 4.5 MGy and the post-irradiation measurements. (b) Normalised modulation efficiency of RMs (RM12 and RM13) with a radius of 7.5 μm for different doping concentrations of the pn-junction during the irradiation up to 4.5 MGy and the post-irradiation measurements.

In Figure 5.5a, an evident degradation in modulation efficiency is observed with increasing TID. Saturation in degradation is observed after 1 MGy. Specifically, the high doping RM encounters a degradation to 80% of its initial efficiency after 4.5 MGy, whereas the low doping one has around 50% of the original modulation efficiency. However, at the beginning of the irradiation, the effect of the increase in modulation efficiency is noticeable, and the normalised modulation efficiency is greater than 1 at the beginning of the irradiation before it starts to degrade. This effect was previously reported in [149], [153], and [162]. The answer lies in a fixed positive charge that has been deposited at the Si/SiO_2 interface, which then pushes the free carriers in the rib toward the centre of the rib. This effect impacts the effective refractive index of the waveguide and the phase shift. The induced phase shift is stronger for the same bias voltage, which reflects in an enhancement of the modulation efficiency.

Following irradiation, measurements resumed under identical conditions for 75 hours. The positive trend in recovery can be noticed in both the RMs, with nearly full recovery to initial modulation efficiencies after 30 hours. It is essential to mention that an anomaly occurred during data acquisition in the post-irradiation phase, resulting in the low doping RM being heated to 140°C for longer than 40 seconds. This prolonged heating led to an accelerated recovery, inducing a noticeable jump in the data.

For RMs with a radius of 7.5 μm (Figure 5.5b), the contrast between high and low doping RMs becomes more pronounced. These RMs were heated to roughly 80°C, unlike the previous ones. In this example, the low doping RM experienced a degradation, possessing just 20% of its initial

modulation efficiency, while the high doping RM had 90% of the starting value after the same TID. Even though the low doping RM encountered severe degradation, after 75 hours of post-irradiation measurement, it recovered to approximately 55%. The conclusion can be drawn that the higher doping concentration positively affects the radiation hardness of the ring modulators.

Radius

In the design of the PICv2, two values for ring radius were taken into consideration: 5 μm and 7.5 μm. The normalised modulation efficiencies of RMs with different radii are depicted in Figure 5.6. Two RMs are high doping RMs, and they have the other design parameters such as W_{Dop} width and the slab width the same. Moreover, the RM with a radius of 5 μm was operated at a temperature of 120°C for 40 seconds every 30 minutes, while the RM with a radius of 7.5 μm was at 80°C with the same intervals as the former. The results suggest a higher radiation tolerance in the larger radius ring modulator compared to the other RM. However, it is important to note that these differences may be attributed to the different operating temperatures, which will be further investigated.

Despite the apparent differences in degradation rates during irradiation, subsequent post-irradiation measurements reveal nearly identical response characteristics. Therefore, based on these findings, drawing a definitive conclusion regarding the direct impact of ring radius on radiation hardness remains a complex task. Further research is needed to estimate the connection between ring radius and radiation hardness.

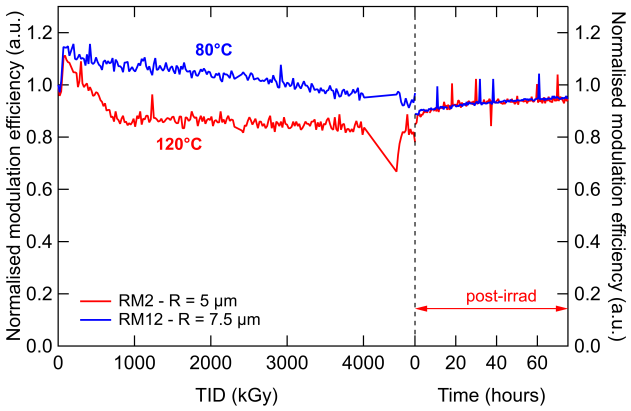

Figure 5.6: Normalised modulation efficiency of high doping RMs (RM2 and RM12) with different radii during the irradiation up to 4.5 MGy and the post-irradiation measurements.

Width of W_{Dop}

Various values of W_{Dop} were incorporated in the design of the ring modulators. Figure 5.7a illustrates the modulation efficiencies of high doping ring modulators with W_{Dop} values of 100 nm, 10 nm, and -10 nm. All three ring modulators possess a radius of 5 μm, a slab width of 1000 nm, and a through-port gap of 160 nm. They underwent heating of 40 seconds every 30 minutes at

temperatures of 120°C, 110°C, and 130°C, respectively. The observed decline in the modulation efficiencies during irradiation is comparable for all presented RMs. In the post-irradiation part, a small difference is noticeable between the curves. The RMs at more than 110°C have recovered to more than 90% of initial efficiency, while the RM at 110°C stayed with a normalised modulation efficacy of 0.83. Consequently, a definitive conclusion on how the width W_{Dop} affects the radiation hardness of RMs based solely on these results is not feasible.

However, Figure 5.7b presents modulation efficiencies for ring modulators with identical designs but featuring lower doping concentrations. They were operated at temperatures of 140°C, 140°C, and 130°C, respectively. Notably, the ring modulator with a wider W_{Dop} exhibits more degradation compared to the other two, with modulation efficiency reducing to 50% of its initial value, in contrast to the latter two, which experienced only a 30% reduction in efficiencies. It was expected that the shorter the W_{Dop} region gives the more radiation-tolerant devices. Nevertheless, the shorter W_{Dop} will influence the performance of the ring modulator and the compromise between the two must be achieved.

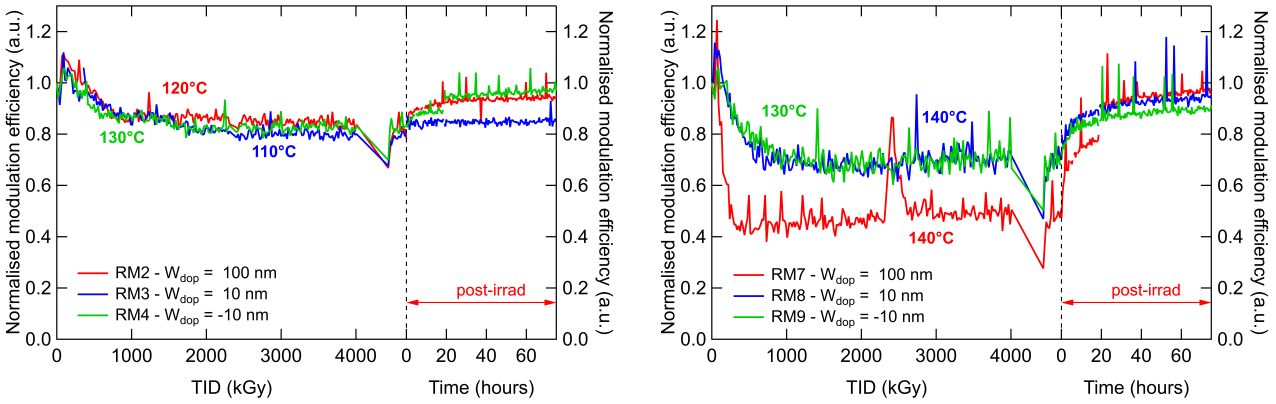

Figure 5.7: (a) Normalised modulation efficiency of high doping RMs (RM2, RM3, and RM4) for different W_{Dop} widths during the irradiation up to 4.5 MGy and the post-irradiation measurements. (b) Normalised modulation efficiency of low doping RMs (RM7, RM8, and RM9) for different W_{Dop} widths during the irradiation up to 4.5 MGy and the post-irradiation measurements.

Slab doping

The primary cause of ionising radiation-induced damage in the SiPh modulators is attributed to the low doping concentration within the slab region and the pinch-off effect that occurs consequently. The hypothesis would be that elevating the doping concentration within the slab region could potentially enhance the radiation tolerance of the ring modulator. Bearing that in mind, an RM with a slab doped with contact doping (p++) rather than intermediate doping (p+) was included in the design of PICv2. Figure 5.8 illustrates the normalised modulation efficiencies of RMs employing p+ and p++ slab doping, operated at temperatures of 120°C and 130°C, respectively. Despite the expectations for RM with p++ doping to be more radiation tolerant, no noticeable difference in performance characteristics was observed between the two configurations.

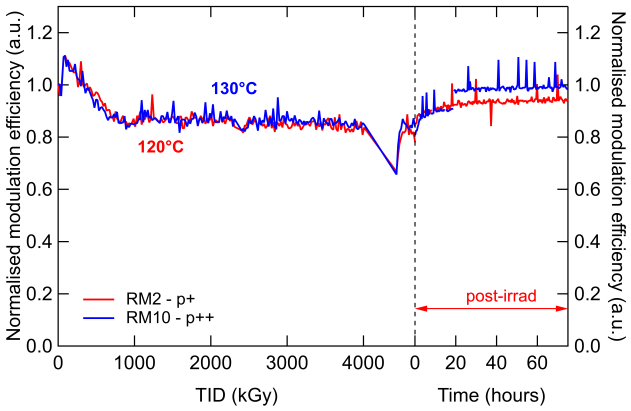

Figure 5.8: Normalised modulation efficiency of high doping RMs (RM2 and RM10) with different doping in the slab on the p-side of the phase shifter during the irradiation up to 4.5 MGy and the post-irradiation measurements.

Heater's temperature

In the previous discussion, distinctions in the modulators' responses may have arisen due to different operating temperatures. Unlike prior investigations, which were based on various modulator parameters, the current analysis maintains the same ring modulator design, differing solely in the measurement protocol. Specifically, one of the ring modulators underwent measurement without employing a micro-heater, whereas the other was subjected to heating by applying a 1 V bias voltage across the heater. The former maintained a constant temperature throughout the entire experiment, remaining at room temperature. In contrast, the latter underwent periodic heating for approximately 40 seconds every half hour, reaching a temperature of 120°C. As depicted in Figure 5.9, it is evident that the non-heated ring modulator exhibited no noticeable degradation during the irradiation, in contrast to the heated one, which experienced degradation to some extent. In the post-irradiation phase, only a gradual decrease in the efficiency of the non-heated RM was noticed. This is possibly happening due to the leftover charge trapped at the Si/SiO_2 interface, which will diffuse further from the waveguide over time, thus, the enhancement of the modulation efficiency will disappear.

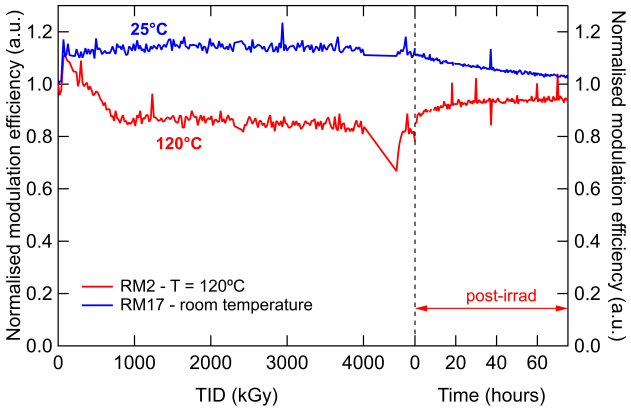

Figure 5.9: Normalised modulation efficiency of high doping RMs (RM2 and RM17) with one RM (RM17) kept at room temperature and the other (RM2) heated to 120°C during the irradiation up to 4.5 MGy and the post-irradiation measurements.

Other parameters

In addition to the previously mentioned parameters, the modulation efficiencies of the remaining RMs were subjected to comparative analysis. In this study, an investigation was conducted regarding the impact of slab length, through port gap, and drop port gap on radiation hardness. Upon careful examination of the modulation efficiency characteristics of such RMs, no noticeable difference was observed. Consequently, it is concluded that neither the slab length nor the through port or drop port gaps have an impact on the radiation hardness of the ring modulators. Nevertheless, it is crucial to consider these parameters during the design phase, as the RMs' performance depends upon them.

5.1.1.3 Modulator comparison

In this subsection, a comparative analysis was conducted between two different modulator types. The experiments were conducted under uniform conditions, specifically at room temperature and subjected to a TID of up to 4.5 MGy. Both modulators possess identical geometrical attributes of their cross-section, such as a W_{Dop} width of 100 nm, and the same etching depth. Nevertheless, they differ in their doping concentrations, with the MZM having lower doping, while the RM has higher doping levels. It is worth noting that in this X-ray test, no RMs with low doping were at room temperature, so the comparison between such two modulators was not possible.

Figure 5.10 illustrates the modulation efficiencies of both modulator types during and after irradiation. The ring modulator undoubtedly outperformed the Mach-Zehnder modulator throughout the irradiation and subsequent post-irradiation phases. Whereas the modulation efficiency of the MZM exhibited a monotonous decline after 100 kGy, the RM demonstrated an enhancement in efficiency with no observable degradation, even at the maximum dose of TID. At 4.5 MGy of TID, the MZM had approximately 50% of its initial efficiency, whereas the RM demonstrated an efficiency exceeding its pre-irradiation values. The phenomenon of modulation enhancement was discussed in the preceding section. Following the end of the irradiation, both modulators experienced a gradual degradation over the subsequent 75 hours.

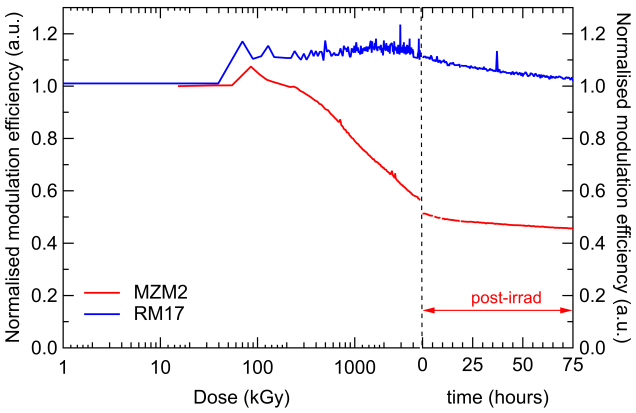

Figure 5.10: Normalised modulation efficiencies of deep-etched MZM and high doping RMs at room temperature during the irradiation up to 4.5 MGy and the post-irradiation measurements.

The primary conclusion drawn from the initial irradiation test is that ring modulators exhibit excellent potential as radiation-hard modulators when compared to Mach-Zehnder modulators.

Within the MZM designs on the chip, it was observed that the one possessing a thicker slab demonstrated slightly better resistance to radiation effects. Furthermore, ring modulators characterised by high doping concentrations undoubtedly manifested better performance. On the other hand, other parameters did not have a strong impact on radiation hardness. The findings from this preliminary test highlighted the significance of monitoring the temperature of ring modulators. This factor substantially influences the radiation hardness, therefore, it will be a primary focus of upcoming X-ray irradiation tests.

5.1.2 Second X-ray test - temperature variations

In April 2021, the second X-ray test was conducted, again focusing on Section #1 of the chip. The primary objective of this test was to identify the influence of the temperature on the radiation hardness of the ring modulators and to create a more robust setup for monitoring modulators without interruptions. Further, measuring the other parameters of the modulators except just optical power and optical spectrum was necessary. As depicted in Figure 5.11, the experimental setup can be divided into two pathways: the optical pathway, denoted in yellow, and the electrical pathway, featuring blue schematic blocks. A significant difference from the setup used in the first test was the integration of a 20-channel programmable voltage source. This voltage source was employed as an autonomous supply for each micro-heater, allowing programmable voltage control and enabling individual current measurements for each channel. To eliminate parasitic resistance from the long wires, every channel was connected using a 4-wire measurement method. By simultaneously measuring both current and voltage on the heater, it was possible to calculate the power applied to the heater and consequently determine the modulator temperature. With this programmable voltage source in the setup, it became possible to maintain the ring modulators at consistent temperatures throughout the entire test, i.e. during the pre-irradiation, irradiation, and post-irradiation phases. Moreover, every ring modulator can have an individual working temperature, not dependent on the others.

With the exception of the programmable voltage source, all instruments employed in the setup were connected in parallel via GPIB cables and subsequently connected to a PC through a *National Instruments* GPIB-to-USB converter. Communication with the programmable voltage source was established using the Inter-Integrated Circuit (I2C) protocol. The procedures for instrument control were written in Igor Pro, and the code for data acquisition and subsequent analysis functions were also implemented within Igor Pro. The measurement procedure consisted of the spectrum measurements of MZMs, RMs, and the shunt, the optical power measurements on every channel, the measurement of the leakage currents of both MZMs and RMs, and the recording of the precise current and voltage of micro-heaters. The measurements were automated and repeated during the experiment in an infinite loop. One measurement loop for measuring all the devices took approximately 40 minutes, with specific data points recorded at intervals of 40 minutes.

Similarly to the first irradiation test, all instruments stacked in a rack and connected to the PC were placed next to the irradiation cabinet. The board with the PIC on it was placed inside the cabinet under the X-ray tube, with a Peltier cooler beneath it. The distance between the chip and the X-ray tube was set to 50 mm. At this height, the beam diameter was uniform up to 5 mm in the x-direction and 6 mm in the y-direction. Since the area of Section #1 is 4 mm by 5 mm, the dose delivered to the chip was uniform all over the area. The power supply voltage of the tube was 40 kV, and the current was 50 mA. The dose rate was 15.83 Gy/s (5.69 Mrad/h) with the maximum variation up to ±8.44%. The chip was exposed to 11 MGy of TID. Throughout the irradiation process, the temperature of the PCB was regulated by the Peltier cooler, as the integrated cooler in the radiation

cabinet used in the first test was non-operational. The Peltier cooler was independently controlled from the rest of the setup via the *ILX Lightwave LDC-3714B* laser diode controller, maintaining the PCB temperature at 25°C.

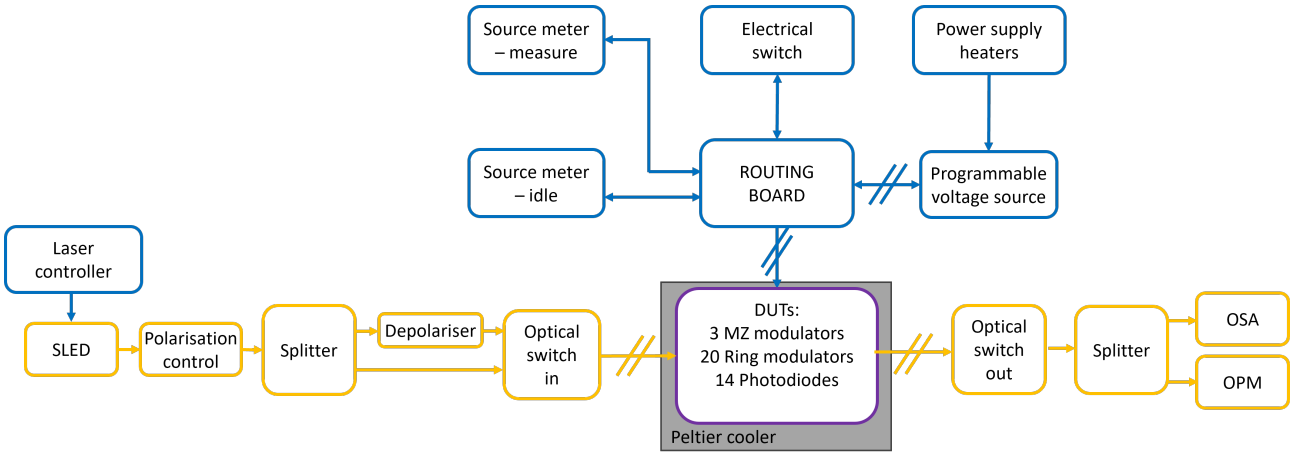

Figure 5.11: Scheme of the setup used for the second X-ray test conducted in April 2021.

The measurement for this experiment was conducted in three phases. In the initial phase, the measurement loop was running for 15 hours without any irradiation present. In this phase, pre-irradiation values of every parameter were recorded. After the beam was initiated, data acquisition occurred at 40-minute intervals over the course of 8 days until the TID of 11 MGy was reached. Afterwards, following the end of the X-ray beam, data recording continued for a duration of 150 hours at the same intervals to monitor the post-irradiation effects, including additional degradation or annealing phenomena.

The temperature on the DUT board was monitored throughout the whole experiment. As illustrated in Figure 5.12, a consistent temperature of 25°C was maintained during the pre-irradiation phase. When the beam was initiated, the temperature was gradually increasing during this phase and reached a maximum of 31.5°C at the end of the irradiation. The increase in temperature can be attributed to the heating produced by the X-ray machine, as the integrated cooler in the radiation cabinet used in the first test was non-functional, and the Peltier cooler was not compensating enough. Since the increase was 6.5°C during the 8 days, the temperature change was slow and

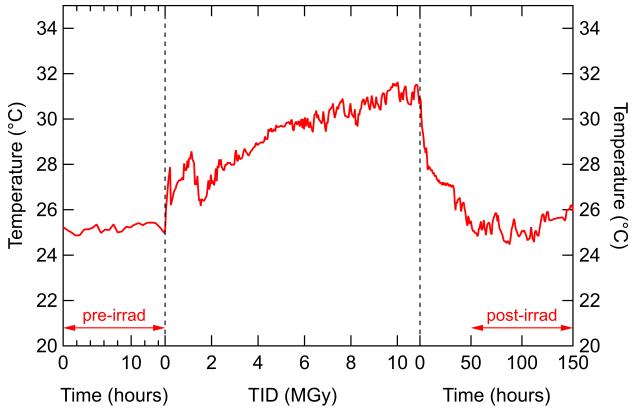

Figure 5.12: Temperature of the DUT board during the pre-irradiation, irradiation, and post-irradiation phase.

marginal for measuring the phase shift of ring modulators. After the beam was turned off, the temperature was stabilised and reached the initial 25-26°C at the end of the post-irradiation phase.

5.1.2.1 Shunt waveguide

The simplest configuration within the PICv2 includes a Si waveguide situated between two grating couplers. The length of this waveguide is approximately 1.5 mm. Figure 5.13 displays the change in optical power observed in the shunt waveguide during irradiation, reaching a TID of 11 MGy. At the beginning of irradiation, a loss of approximately 0.07 dB is observed at the output of the shunt waveguide. Further, a gradual increase in optical loss is documented throughout the irradiation. Particularly, this increase in loss exhibits a correlation with the temperature of the board presented in Figure 5.12. After the end of irradiation, the optical loss is lower with the decrease in temperature. Consequently, it is reasonable to attribute this additional optical loss to the elevation in temperature rather than the irradiation itself. In conclusion, ionising radiation does not lead to a substantial increase in optical loss within integrated Si waveguides, even when irradiated up to a maximum TID of 11 MGy.

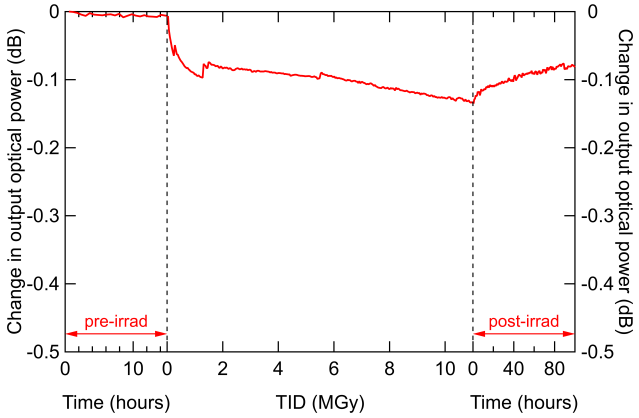

Figure 5.13: Change in optical power at the output of the shunt waveguide during the irradiation up to TID of 11 MGy.

5.1.2.2 Different modulator designs at room temperatures

In this study, a comparative analysis of different modulator designs at room temperature has been carried out. Furthermore, the results obtained from the modulators in PICv2 were compared with those of the previous chip design, PICv1.[3] One key difference between PICv1 and PICv2 is that the latter was manufactured in the improved fabrication process now available from the foundry. One of the major changes in the process is the change in nominal doping concentrations in the different cross-section regions. While the foundry does not reveal the absolute values of these doping concentrations, the values normalised to the overall lowest doping concentration are reported in Table 5.1.

Both PICs' modulators share the same etch depths of 160 nm and rib heights of 220 nm. In the case of MZMs, the rib width is 450 nm, whereas RMs have a rib width of 500 nm. The slab widths for MZMs and RMs are 1275 nm and 1000 nm, respectively. Variations in the W_{Dop} parameter have

[3]Results from PICv1 presented here are not measured during the second X-ray test. These results were collected prior to the beginning of the research on this thesis.

been introduced in order to enhance radiation tolerance. Specifically, PICv1 MZM and PICv2 MZM3 are characterised by a W_{Dop} of 300 nm, whereas the rest of the modulators feature a W_{Dop} of 100 nm. Two MZM configurations with two different doping concentrations and one RM configuration with three distinct doping concentrations are subjected to assessment.

Table 5.1: An overview of the design parameters of the tested devices

	Device	W_{Dop} (nm)	Relative doping concentration	
			rib (p/n)	slab (p+/n+)
PICv1	MZM	300	3x	11x
	RM	100	5x	
PICv2	MZM3	300	1x	50x
	MZM2	100	1x	
	RM7	100	1x	
	RM2	100	10x	

Two different types of MZMs were tested, two designs with W_{Dop} of 300 nm, and one design W_{Dop} of 100 nm,. In Figure 5.14a, the radiation tolerance of the same MZM design on the two chip iterations is compared. This gives an indication of the impact on radiation tolerance introduced by the foundry process changes. The normalised modulation efficiency as a function of TID for the MZM from PICv1 and MZM3 is plotted in Figure 5.14a. The measured modulation efficiency is approximately constant until a dose of 70 kGy and until a dose of 1 MGy for PICv1 MZM and MZM3, respectively, after which it quickly approaches zero. Since both devices have the same geometrical design parameters, the improvement in radiation-hardness is due to changes in the production process and differences in doping concentrations in the rib and slab regions. The lower doping concentration in the rib region leads to the better optical performance of MZMs [168], while the higher doping concentration in the slab region indicates more effective compensation for ionising radiation damage in the pinch-off region. Note that the modulation efficiency of the MZM from PICv1 is greater than 1 at the beginning of the irradiation before it starts to degrade.

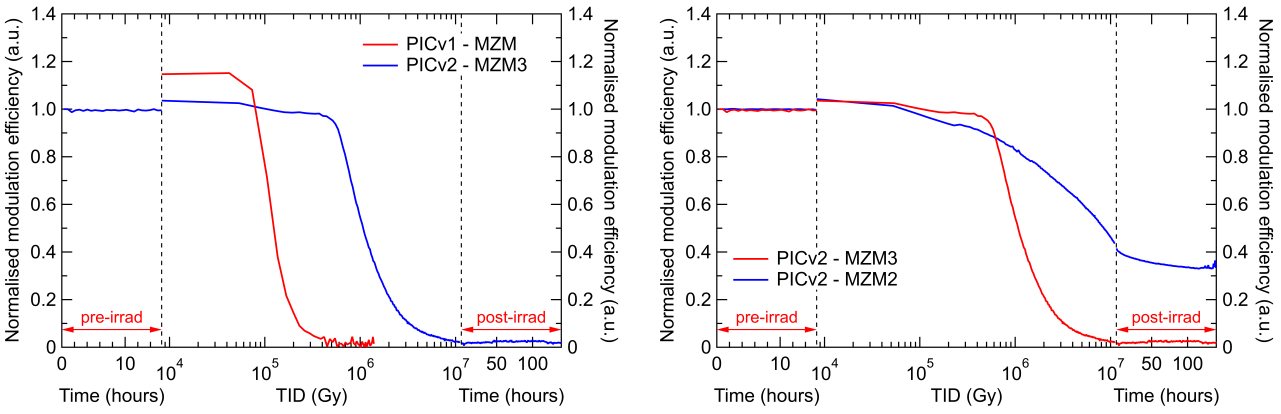

Figure 5.14: (a) Modulation efficiency degradation with TID of MZM with W_{Dop} of 300 nm normalised to its pre-irradiation value for the two PIC versions. (b) Modulation efficiency of the MZM3 and MZM2 from PICv2 normalised to its pre-irradiation value.

Figure 5.14b shows the difference in the modulation efficiency degradation between the MZM3 and MZM2 of PICv2. The MZM3 started rapidly to degrade after 1 MGy. However, the MZM2 degraded more slowly with the increase of TID. Remarkably, it is still operable after 11 MGy, but with a reduced efficiency of 40% of its pre-irradiation value. The main difference between MZM3 and MZM2 is in the width of W_{Dop}, which is shorter in the latter case. By reducing W_{Dop}, the possible pinch-off region is shorter, and the p+ doped region will easily compensate for the lower concentration of free holes. Hence, the radiation tolerance increases by reducing W_{Dop}.

Figure 5.15 shows the normalised modulation efficiencies for RMs with the same cross-section though with three different doping concentration levels. The modulation efficiency of the PICv1 RM, represented by the red curve, begins to rise slowly until 200 kGy and then rapidly starts to degrade, finally falling down to zero at 500 kGy. The blue curve shows the behaviour of the same design of RM on PICv2 (RM7) but with three times lower doping concentration. Although it was expected for RM with the lowest doping concentration to be the least radiation tolerant, the higher doping concentration in the slab region influenced RM7 to be more radiation tolerant than PICv1 RM. Even though this design is more radiation tolerant than the RM from PICv1, it still degrades and has almost no modulation efficiency after 11 MGy. The green curve shows the RM2 with ten times higher doping concentration than the minimal. Surprisingly, this design stays fully functional even after the TID of 11 MGy. Once the X-ray beam was turned off, the measurement of transmission characteristics was continued for the following 150 hours with the goal of observing possible post-irradiation annealing. Whilst keeping the same measurement conditions during this time, only a gradual decrease of efficiency to 90% of its pre-irradiation value was noticed. This is possibly happening due to the leftover charge trapped at the Si/SiO_2 interface, which will diffuse further from the waveguide over time, thus, the enhancement of the modulation efficiency will disappear. The significant difference between RM7 and RM2 could be attributed only to a difference in the doping concentrations of the pn-region. This is consistent with previous work on MZMs, showing that a higher doping concentration in the rib enhances radiation resistance [149] and the first X-ray test.

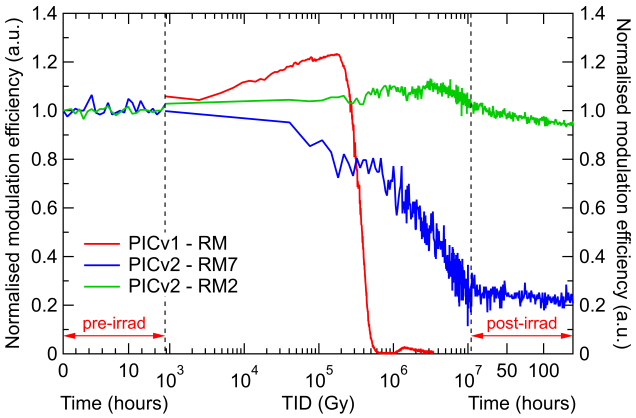

Figure 5.15: The modulation efficiency of the three tested RM designs normalised to its pre-irradiation value for different doping concentrations.

Finally, if the two modulator designs with the same cross-section and doping concentrations from the PICv2 (RM7 and MZM2) are compared, the difference in their modulation efficiency can be seen in Figure 5.16. It can be noticed that degradation curves have the same trend for both modulators. The MZM degrades to 40% of its initial value after 11 MGy. In the post-irradiation period, it keeps gradually degrading over time such that after 150 hours, it falls down to 35% of its initial value. Possible further degradation after this period was not recorded. The RM has slightly

lower modulation efficiency during the irradiation and also much more noise in the measurement. The only difference between the two is a different kind of modulator design with different footprint dimensions. Even though the MZM shows slightly better results, it should be noted that the best MZM design and the worst RM design in a matter of performance were compared.

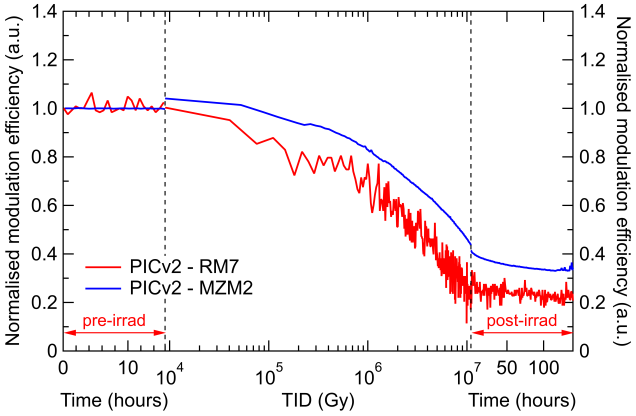

Figure 5.16: The modulation efficiency of the two modulator designs with the same cross-section and doping concentrations from the PICv2 normalised to their pre-irradiation value.

5.1.2.3 Effect of temperature on radiation-hardness of ring modulators

In order to observe the radiation tolerance dependence on temperature, six RMs (RM2, RM6, RM10, RM15, RM17, RM19) with the same cross-section parameters and doping concentrations were irradiated while locally heated at temperatures in the range from 25°C to 200°C. Specifically, RM6 at 25°C, RM10 at 60°C, RM2 at 100°C, RM19 at 125°C, RM17 at 150°C and RM15 at 200°C. The operating temperatures of the RMs were calculated according to the heater characterisation carried out before the irradiation test. The results are shown in Figure 5.17. All mentioned devices were constantly kept at the desired temperature during the test. The device at 25°C shows no degradation after 11 MGy. For the device kept at 60°C, the degradation is significant. However, the recovery in the post-irradiation measurement is evident. This RM recovered from 20% of its initial efficiency up to 70% after 150 hours of post-irradiation heating. The RM operated at 100°C degraded even more quickly than the one at 60°C, but after 11 MGy it reached the stable value of 40% of its initial modulation efficiency. In the post-irradiation period, the recovery was faster than that in the case of 60°C due to higher temperature annealing. At the end of the measurement period, the modulation efficiency of this RM was 85% of its pre-irradiation value. If the results were compared at these three temperatures, the room temperature presents the best result because it does not show any degradation. However, the RM operated at room temperature is expected to degrade at a higher TID level, which is not reached in this experiment. During the post-irradiation period, RMs operated above room temperature experienced recovery, while the RM at room temperature still degraded after the X-ray source was turned off.

For higher temperatures, 125°C, 150°C and 200°C, the degradation after 11 MGy is minimal. The devices reach a stable state of 80%–90% of their initial modulation efficiency at 2 MGy, after which no further degradation occurs with the ionising dose. This would indicate that the recovery rate at these temperatures matches the degradation rate. For these temperatures, the post-irradiation recovery reaches 97% of their initial performance. Running RMs above 125°C could be an advantage over lower operating temperatures thanks to the fast TID damage recovery observed during this test. Since the annealing rate is independent of the dose rate, and the degradation rate is dependent

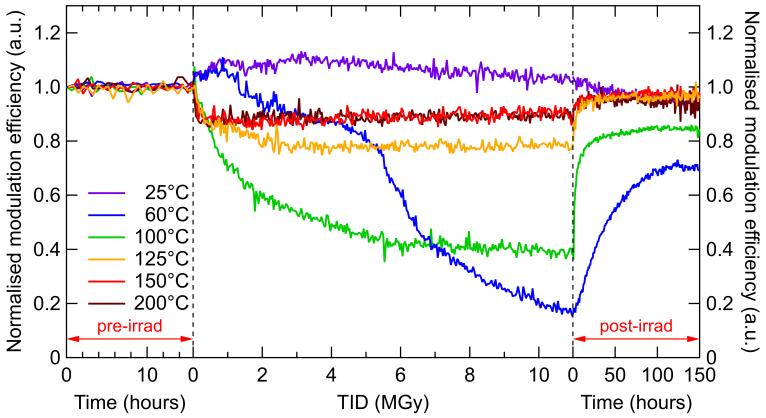

Figure 5.17: Normalised modulation efficiencies of high doping ring modulators operated at different temperatures (RM6 at 25°C, RM10 at 60°C, RM2 at 100°C, RM19 at 125°C, RM17 at 150°C and RM15 at 200°C).

on the dose rate, a different degradation curve is expected for dose rates more similar to the LHC environment.

Figure 5.18 depicts four low-doping RMs (RM7, RM8, RM9, RM13) subjected to similar conditions. These modulators underwent localised heating within a temperature range from 25°C to 200°C. Specifically, RM7 at 25°C, RM13 at 60°C, RM8 at 100°C, RM9 at 200°C. The RM operating at 60°C exhibited the most noticeable degradation, with its modulation efficiency approaching zero after just 2 MGy of TID. Nevertheless, despite the fact that the normalised modulation efficiency of this RM reached zero after 11 MGy, in the post-irradiation phase, the RM recovered up to 70% of its pre-irradiation value. The recovery trend aligns closely with that observed in the RM with higher doping concentrations at the same temperature. The RM operated at 25°C experienced a degradation to 25% of its initial efficiency, and this degradation continued even when the beam was deactivated. The RM operated at 100°C exhibited less degradation compared to the prior two, eventually stabilising at approximately 50% of its pre-irradiation efficiency after a TID of 2 MGy. After the end of irradiation, this RM exhibited a recovery to 80%, aligning with the results observed for the high-doping RMs. Lastly, the RM operated at 200°C gave the most favourable results, maintaining a modulation efficiency consistently above 90% throughout the duration of the experiment. Once again, it has been demonstrated that the high operating temperatures are advantageous regardless of the levels of doping concentrations.

Regarding the leakage currents that were measured during this test, all modulators, regardless of the operating temperature, had similar values. The leakage currents for MZM modulators were around 2 nA and 4 nA for 1 V and 2 V bias voltages and stayed below these values all the time. For the RMs, the leakage current for 1 V bias voltage before irradiation was approximately 2 nA, and after the beam was started, the currents dropped to 0.2 to 0.3 nA range and stayed in it during the whole test. For the 2 V bias voltage, RMs leakage currents were 3 nA before the irradiation and in the range from 0.4 to 0.5 nA during the irradiation.

In conclusion, the test performed here was an accelerated test, where the 10 MGy TID expected to be accumulated in ten years of operation in the innermost part of the CERN Experiments was reached in eight days. Therefore, understanding the rate of TID damage and annealing when exposed to the dose rate present in the CERN detectors is a key point to predict the device performance across the foreseen ten-year lifetime.

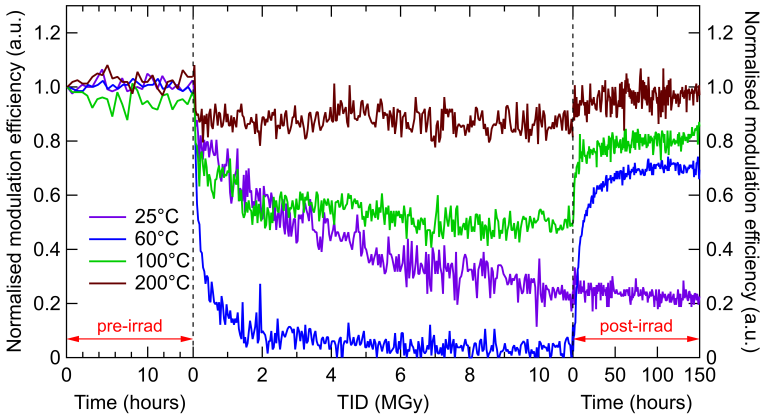

Figure 5.18: Normalised modulation efficiencies of low doping ring modulators operated at different temperatures (RM7 at 25°C, RM13 at 60°C, RM8 at 100°C, RM9 at 200°C).

5.1.3 Third X-ray test - lower dose rate

In February 2022, the third and final X-ray test for Section #1 was conducted. The primary objective of this test was to test the response of ring modulators at a lower dose rate and to closely study the effect of high temperature on the annealing in order to determine the ideal mode for their operation. The scheme of the setup used in this test is the same as one used in the second X-ray test and presented in Figure 5.11. Similarly to the other two irradiation tests, all instruments stacked in a rack and connected to the PC were placed next to the irradiation cabinet. The board with the PIC on it was placed inside the cabinet under the X-ray tube, with a Peltier cooler beneath it. The distance between the chip and the X-ray tube was set to 70 mm. At this height, the beam diameter was uniform up to 4 mm in the x-direction and 6 mm in the y-direction. The dose delivered to the chip was uniform all over the area of the Section #1. The power supply voltage of the tube was 40 kV, and the current was 25 mA. The dose rate was 5.55 Gy/s (2 Mrad/h) with the maximum variation up to ±3.17%. The chip was exposed to 3.3 MGy of TID.

Throughout the irradiation process, the temperature of the PCB was regulated by the Peltier cooler, as the integrated cooler in the radiation cabinet used in the first test was non-operational. The Peltier cooler was independently controlled from the rest of the setup via the *ILX Lightwave LDC-3714B* laser diode controller, maintaining the PCB temperature at 25°C. Unfortunately, the Peltier cooler, more precisely the controller, experienced a problem during the period between 150 hours to 180 hours after the beam was stopped, during which time the substrate temperature rose to an unknown value. In this period, the recorded data are not accurate and this is indicated by the shaded red areas.

Figure 5.19 illustrates the temperature of the DUT board as measured by the PT100 sensor. Throughout the pre-irradiation phase, the temperature remained stable at 25°C. Following the start of the irradiation beam, a minor temperature spike was noticeable. However, it was quickly compensated, with temperature maintained within the range of 25°C to 28°C throughout the rest of the test. In the post-irradiation phase, the board's temperature mostly remained at approximately 25°C (with minimal oscillations of ±0.5°C between day and night), except during the period characterised by the malfunction of the cooling system, resulting in a temperature spike to 60°C. Once the system was repaired, the temperature stabilised at 25±0.5°C until the end of the measurements.

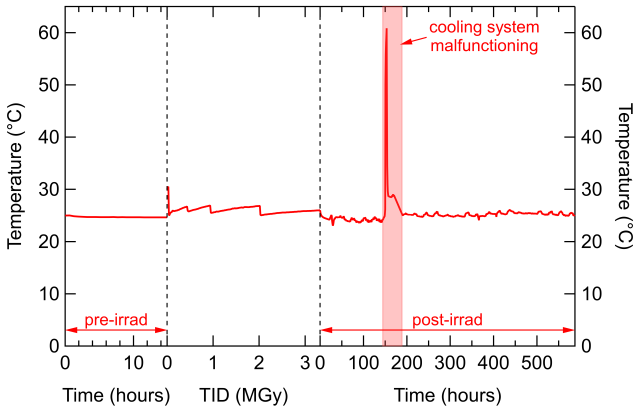

Figure 5.19: Temperature of the DUT board during the pre-irradiation, irradiation, and post-irradiation phase.

5.1.3.1 Effect of different dose rates

Previously reported observations indicate the sensitivity of Metal-Oxide-Semiconductor Field-Effect Transistor (MOSFET) devices to different dose rates [107], [169], [170], indicating that lower dose rates induce greater damage in such devices. Considering the structures' similarities, SiPh devices were subjected to a dose rate three times lower than in the previous test. The responses of the Mach-Zehnder modulators (MZM2) from both X-ray tests are illustrated in Figure 5.20. Throughout both tests, the MZMs were operated at room temperature, subjected to a 1 V reverse bias, and irradiated with the same X-ray source.

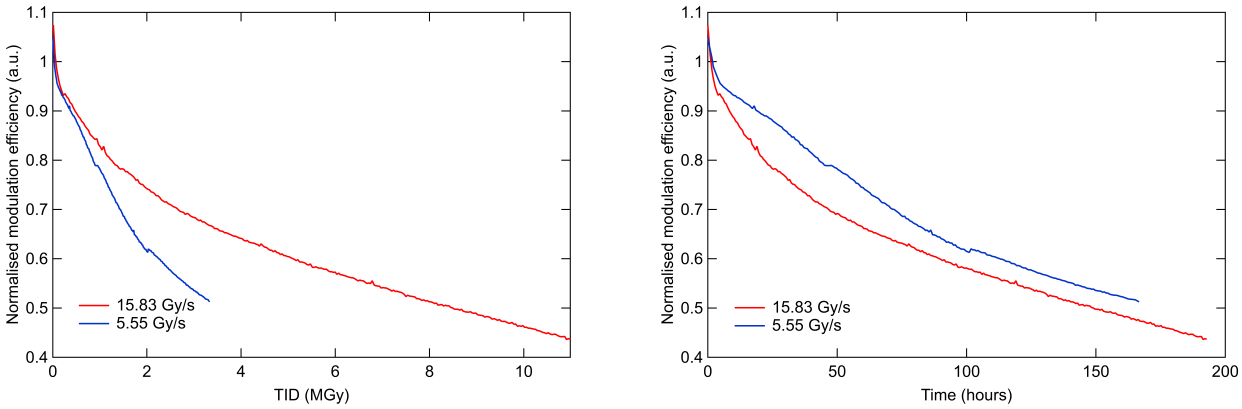

(a) **(b)**

Figure 5.20: (a) Modulation efficiency of MZM2 for different dose rates over total ionising dose. (b) Modulation efficiency of MZM2 for different dose rates over time.

Figure 5.20a shows the degradation of the normalised modulation efficiency over the accumulated total ionising dose for dose rates of 15.83 Gy/s and 5.55 Gy/s. An MZM irradiated at the lower dose rate exhibited a more pronounced degradation compared to its counterpart subjected to the higher dose rate. At the accumulated TID of 3.3 MGy, corresponding to the maximum dose received at a dose rate of 5.55 Gy/s, the MZM exposed to the lower dose rate experienced a degradation to 50% of its initial modulation efficiency. In contrast, the MZM exposed to the higher dose rate retained 67% of its pre-irradiation modulation efficiency at the same TID. The MZM subjected to the higher dose rate reached the 50% efficiency mark after an accumulated TID of 8 MGy. However,

upon comparing the two MZMs over time, as depicted in Figure 5.20b, the difference between them is less evident. The MZM subjected to a lower dose rate exhibited a milder degradation than the MZM exposed to the higher dose rate, with less than 5% difference observed between the two after the end of the shorter test.

Given that the predicted dose rate in HL-LHC (10^3 Gy/day) will be three orders of magnitude lower than in these tests, the observed outcomes raise significant concerns for SiPh optical links. However, prior tests have indicated that the high operating temperatures of ring modulators can induce thermal annealing in these devices. Therefore, a further investigation was conducted to examine the influence of various dose rates on ring modulators. A series of ring modulators were subjected to an equivalent temperature as in the second X-ray test, while the delivered dose rate was reduced by a factor of three. The results for ring modulators at temperatures of 100°C and 150°C are depicted in Figure 5.21. It is noteworthy that the identical ring modulators were subjected to the same temperatures in both experiments, thus enabling a direct comparison of the results without the influence of any geometrical parameters.

Figure 5.21a illustrates two ring modulators (RM2 and RM19) at 100°C. The RM exposed to a dose rate of 5.55 Gy/s exhibited a slightly better performance after 3 MGy of TID than the RM exposed to 15.83 Gy/s dose rate. The first RM degraded to 60% of initial modulation efficiency, while the modulation efficiency of the second one decreased to 55% of the initial value. It should be noted that the RM subjected to the higher dose rate also received a higher cumulative TID (11 MGy in total), resulting in a normalised modulation efficiency of 0.38 following the complete irradiation process. During the post-irradiation phase, despite their different initial states, both RMs exhibited recovery, ultimately converging to approximately 85-90% of their initial modulation efficiency after just 50 hours.

Figure 5.21b demonstrates the behaviour of the two ring modulators (RM17 and RM18) at 150°C. Regardless of the irradiation dose rate, the ring modulators showed minor degradation at this temperature. However, RM at a lower dose rate exhibited marginally less modulation efficiency. In the post-irradiation measurements, the RMs managed to fully regain their initial modulation efficiency. The general conclusion drawn from this investigation suggests that the lower dose rates, consistent with those which will be encountered in the actual operation of the LHC, will have an even more minimal impact on the SiPh ring modulators.

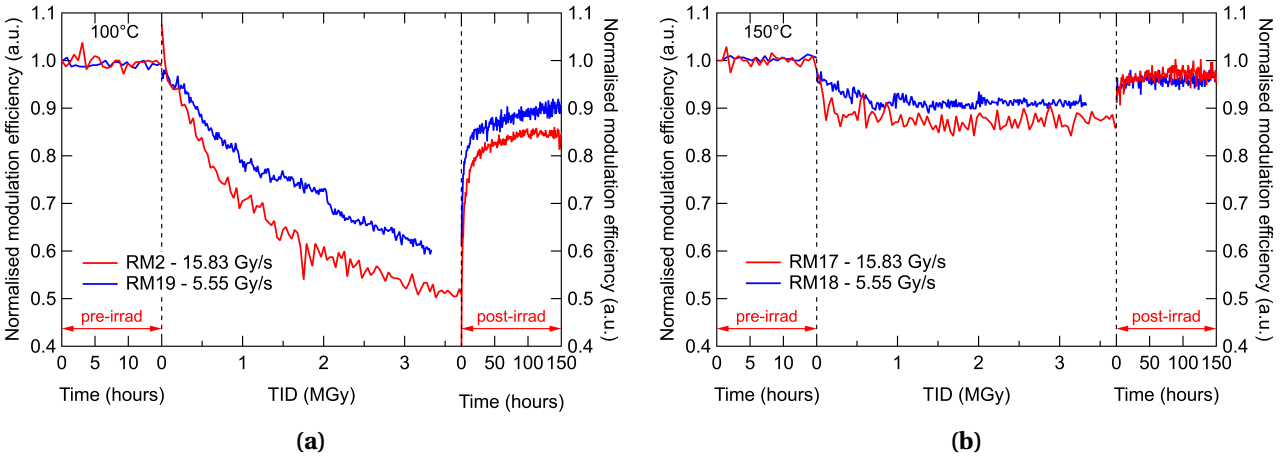

Figure 5.21: (a) Modulation efficiency of ring modulators operated at 100°C for different dose rates. (b) Modulation efficiency of ring modulators operated at 150°C for different dose rates.

5.1.3.2 Different doping concentration in the slab region

Since inconsistent results were observed during the first irradiation test regarding the influence of the doping concentration in the slab region on the radiation hardness of the ring modulator (see Section 5.1.1.2), an additional test regarding the same matter was conducted. Two RM with the same geometrical characteristics except the p-doping in the slab were tested at middle range temperature. The temperature was kept constant at 60°C during all three phases of the test. The specific temperature was chosen since the previous test has shown the most significant degradation at this temperature compared to the lower or higher temperatures. Results are presented in Figure 5.22. The difference between the two characteristics can be easily observed after 3 MGy. Even though both RMs have similar trends in the first couple of MGys, after 2.5 MGy the RM with p+ doping in the slab region experienced a significant loss in the modulation efficiency. The RM with p++ doping had 70% of the initial modulation efficiency after the end of the irradiation, while the modulation efficiency of the other RM fell to 35%. The higher doping in the slab region can more easily compensate for the lack of free carriers in the pinch-off region, which is an outcome of the high ionising dose. In the post-irradiation phase, both RMs started to recover as soon as the beam was turned off. After 50 hours of heating, both RMs reached 80% of the initial modulation efficiency and slowly continued to recover for the next 100 hours, finally reaching 85%. This would suggest that no matter the level of the irradiation damage, the RMs will recover to the same levels for a given temperature. However, an additional question would be whether higher temperatures would anneal the SiPh ring modulators furthermore.

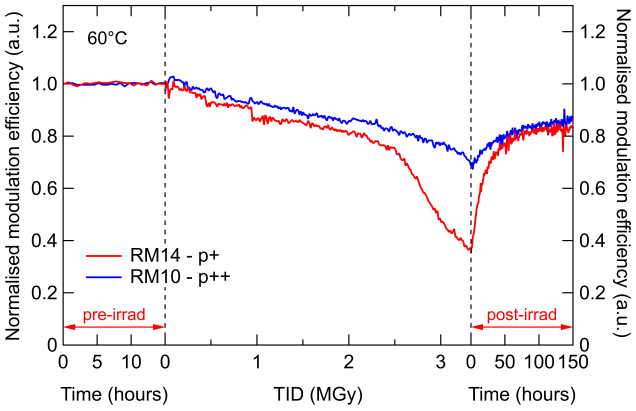

Figure 5.22: Modulation efficiencies of two ring modulators with different doping in the slab region while irradiated with X-rays.

5.1.3.3 Effect of temperature on annealing

In order to inspect the effects of the different temperatures on annealing in SiPh ring modulators, a total of seven RMs were tested with the unique heating campaigns. Two distinct campaigns were used during this test. First, all ring modulators were kept at room temperature during the irradiation and then heated to different temperatures during the post-irradiation phase. Second, the ring modulators were heated to various temperatures, whereas in the post-irradiation phase, at some point, they were all heated to the same high temperature. During the pre-irradiation and the irradiation measurements, temperatures were kept constant. More precisely, four ring modulators were kept at 25°C, one RM at 60°C, one at 100°C, and one at 150°C. The effect of changing the

operating temperature during annealing was studied by changing the device temperatures at different intervals following an initial recovery period of several hundred hours at the original temperature used during the irradiation.

Figure 5.23 illustrates the outcomes for the three high-doping ring modulators (RM2, RM6 and RM15) and one low-doping ring modulator (RM7, black curve). Throughout irradiation, as well as the initial 230 hours of post-irradiation, all ring modulators were kept at room temperature. It should be noted that between 150 and 180 hours, the cooling system experienced a problem, and the results during this period should be disregarded. During the irradiation, all high-doping ring modulators maintained their normalised modulation efficiencies slightly above pre-irradiation levels. Upon turning off the beam, the modulation efficiencies decreased to 1, losing the initial amplification. They remained at this level until the cooling system malfunctioned, after which they lost approximately 10% of their initial modulation efficiency. The precise conditions of the board during this period remain unknown, however, the hypothesis is that uncontrolled heating of the board induced unforeseen effects in the chip, impacting not only the ring modulators, but also the substrate and the rest of the devices on the PIC.

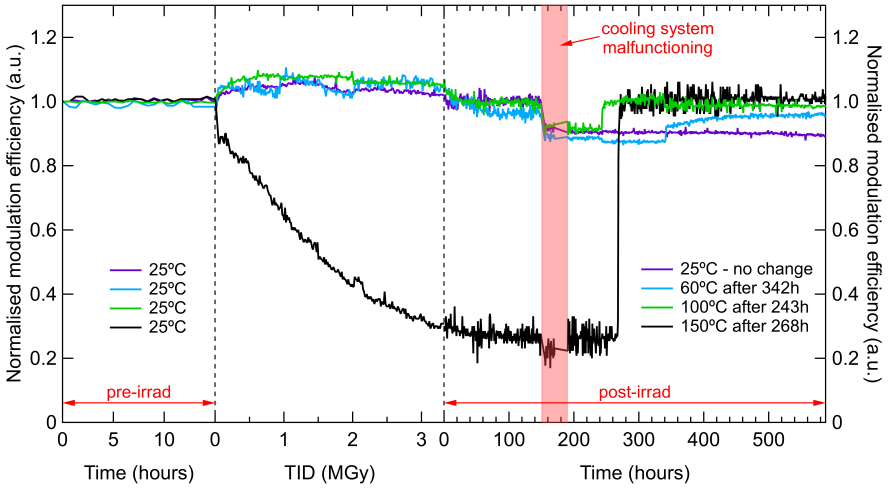

Figure 5.23: Modulation efficiency of four RMs heated to different temperatures after irradiation, one low doping RM (RM7, black curve) and three high-doping RMs (RM2, RM6 and RM15, coloured curves).

The high temperature also induced a difference in the optical coupling. The glue used for attaching the glass fibre block to the board had a glass transition temperature (T_g) of 80°C. Having that in mind, it was noticed that starting with a temperature as low as 40°C, the mechanical properties of the glue started to change, and the fibre block experienced a slight displacement, resulting in a small change of the optical coupling. With the temperature going up to 60°C, the change became more evident. Figure 5.24 shows the optical power measurements recorded at three distinct optical channels, with colours corresponding to those in Figure 5.23. It is evident that the optical power remained relatively stable with minor fluctuations throughout the test, except for three instances associated with setup relocation, and one occurrence linked to the malfunction of the cooling system. Due to constraints on the availability of the irradiation facility, the part of the pre-irradiation and post-irradiation measurements were conducted in different rooms. Consequently, when the setup was moved, optical fibres were reattached, resulting in slight alterations in polarisation and subsequent variations in optical power measurements (the first and the second interruption). The third instance involved a setup relocation within the same room. However, the fourth change in optical powers at the beginning of the red-shaded area is solely

attributed to the different optical coupling between the fibre block and the PIC. Even though the optical power coupled to the RMs is lower, this does not affect the measurement of the modulation efficiency. Therefore, the results presented in Figure 5.23 are not influenced by such change.

Following the resolution of the cooling issue, the experimental setup was carefully monitored for a period exceeding two days to identify any further changes caused by the previously explained problem. Considering that everything was stable, the operating temperatures of three of the ring modulators, RM6, RM15, and RM7, were individually adjusted to 60°C, 100°C, and 150°C, respectively, while one was kept at room temperature. After 243 hours, the temperature of one of the high-doping ring modulators was changed to 100°C, while temperatures of the others remained unaltered. This particular RM underwent thermal annealing, subsequently restoring its modulation efficiency to the pre-irradiation level after 5 hours. After 268 hours, the low-doping RM, which exhibited the highest degradation, was heated to 150°C. The high temperature facilitated thermal annealing in the pn-junction, and the modulation efficiency raised from 20% to 100% of the initial value after 6 hours. Lastly, the RM represented in blue was heated to middle range temperature (60°C) after 342 hours. The specific temperature was chosen to rule out any damaging effects related to this temperature range, given that the devices were exposed to approximately 60°C during the cooling malfunction. However, only positive annealing was observed, with RM recovering to 95% until the end of the test and potentially returning to the pre-irradiation value if the test was extended. The ring modulator that remained under constant conditions throughout the rest of the test did not exhibit any additional degradation or recovery. In conclusion, all heated RMs recovered with different time constants depending on their temperature and the level of degradation, with the RM heated to 60°C being the slowest one to reach a steady state.

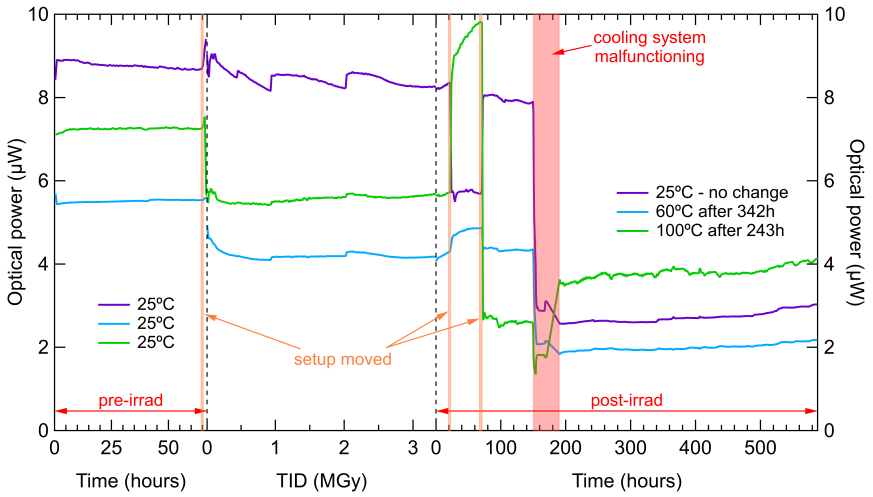

Figure 5.24: Optical power of three RM during the different stages of the test.

The second part of the investigation of the effects of temperature on annealing was to subject ring modulators degraded to different levels to the same high temperature. Figure 5.25 shows diverse levels of degradation of four ring modulators (RM7, RM14, RM19, and RM18) operated at 25°C, 60°C, 100°C, and 150°C, with higher operating temperatures leading to greater radiation tolerance. There are three high-doping RMs and one low-doping RM (black curve). The low-doping RM (black curve) is physically the same device in both figures 5.23 and 5.25. Following the end of the X-ray beam, recovery was observed for all RMs operated at temperatures higher than room temperature. On the contrary, the modulation efficiency of the RM at room temperature kept degrading slowly. In the first part of the post-irradiation measurement, all RMs were kept at the

same operating temperature as during the irradiation. After approximately 200 hours of annealing, all the RMs reached a steady state. The period of the cooling malfunctioning will be disregarded since the values after the repair were the same as those obtained prior to the malfunction. Ring modulators operated at 60°C, 100°C, and 150°C recovered to 82%, 92%, and 97% of the initial values, respectively. The achieved steady-state levels were found to be dependent on the annealing temperature, with higher temperatures leading to more significant recovery.

As no further recovery was observed, three RMs that had been operated at temperatures below 150°C were subjected to temperature elevation to 150°C at different time points. The RM operated at 150°C during the irradiation was maintained at that temperature until the end of the test. After 243 hours, RM previously operated at 60°C was heated, and within 15 hours it reached 98% and slowly continued to recover back to 100% by the end of the test. The temperature of RM operated at 100°C was changed after 342 hours, requiring 35 hours to reach 98% of the initial value. Regarding the RM operated at room temperature, recovery occurred with the fastest rate, with just 6 hours necessary to reach the pre-irradiation values. Ultimately, all RM recovered to 100% of the initial modulation efficiency by the end of the test. The recovery time was longer for RM with smaller degradation compared to the one that degraded the most. This indicates that the time necessary for recovery depends not just on the temperature of the annealing, but also on the extent of degradation. Nevertheless, even in cases where the time required for certain RMs to reach pre-irradiation values was prolonged, these RMs still had sufficient modulation efficiency (phase shift) for accurate operation.

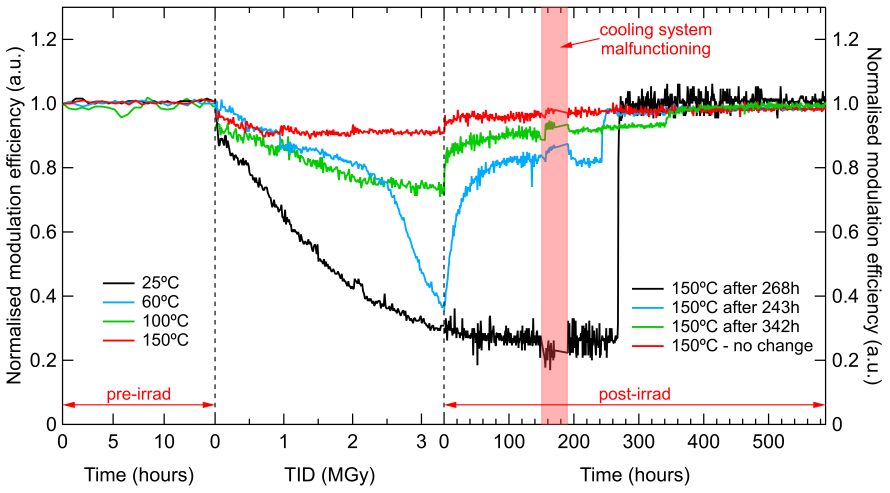

Figure 5.25: Effect of operating temperature on modulation efficiency during irradiation and high temperature during the post-irradiation. One low-doping RM (RM7, black curve) and three high-doping RMs (RM14, RM19, and RM18, coloured curves).

5.1.4 Summary of the X-ray tests on modulators

Comparative analysis revealed that ring modulators exhibit superior resilience to radiation in comparison to Mach-Zehnder modulators, withstanding target doses of 10 MGy ionising radiation. Ring modulators have shown that they can easily handle elevated radiation levels expected during the last run of the LHC.

Specifically, better performance is observed in ring modulators with higher doping concentrations in the rib part of the waveguide when subjected to either type of irradiation. Expanding

contact doping on the p-side of the phase shifter throughout the entire slab contributes to enhanced radiation hardness to ionising radiation. Operation of ring modulators at temperatures exceeding 125°C proves promising, as minimal degradation from ionising radiation is observed at these temperatures. Furthermore, ring modulators at high temperatures exhibit increased resilience to lower dose rates of ionising radiation, in contrast to Mach-Zehnder modulators that experience more pronounced degradation at lower dose rates. Considering the predicted dose rate in HL-LHC ($\sim 10^3$ Gy/day) is three orders of magnitude lower than the conducted tests, even less degradation is expected in an environment more similar to actual LHC conditions. Additionally, thermal annealing of ionisation damage in ring modulators during post-irradiation has been demonstrated, with complete recovery achieved through heating to 150°C, regardless of the initial degradation level.

5.2 Photodiodes

In order to ensure the radiation resistance of the entire optical link, Ge photodiodes were subjected to irradiation. Although promising radiation tolerance to TID has been previously demonstrated in Ge photodiodes, [150], [153], [171], it was necessary to evaluate their resilience against higher doses of TID (i.e. 10 MGy) as required by upcoming upgrades of the LHC. The results presented here were gathered during the second X-ray test conducted on Section #1 when devices were irradiated up to 11 MGy of TID with a dose rate of 15.83 Gy/s. Thus, a set of 14 vertical PIN photodiodes (VPIN1) with identical characteristics were subjected to testing. Seven out of 14 photodiodes are located at the drop port of the ring modulators, while the rest are situated at the add port. Results for the photodiodes located at the drop ports are presented below. No ionising radiation measurement was done on Section #2 populated with different types of Ge photodiodes.

5.2.1 Dark current

The dark current, representing the current generated in the photodiodes in the absence of incident light, was measured when the optical source (SLED) was switched off, while the photodiodes were reverse-biased with 1 V. This measurement was repeated every 40 minutes throughout all three phases of the test. Figure 5.26a illustrates the dark currents for all seven VPIN PDs. Prior to irradiation, dark currents ranged from 10 nA to 16 nA. Upon activation of the beam, a small increase was observed, with currents remaining in the range of 20 to 30 nA, gradually increasing to 26 to 36 nA by the end of irradiation. Following the deactivation of the beam, the dark currents exhibited a gradual reduction, stabilising within the 20 to 30 nA range.

5.2.2 Photocurrent

Following the dark current measurements, the light source was activated, and the response of the seven photodiodes, while reverse-biased with 1 V, was once again recorded. It is noteworthy that, due to the positioning of half of the photodiodes at the add port of the ring modulators, they did not receive direct optical power, and their photocurrents were not recorded. Additionally, the other half of the photodiodes, situated at the drop port of the drop bus waveguide of the RMs, and therefore, the measured photocurrents exhibited relatively low values. In Figure 5.26b, the photocurrents were presented through three phases of the test: pre-irradiation, irradiation, and post-irradiation. The measured photocurrents during pre-irradiation were within the range of 0.2 to 0.8 μA and remained stable throughout all three measurement phases.

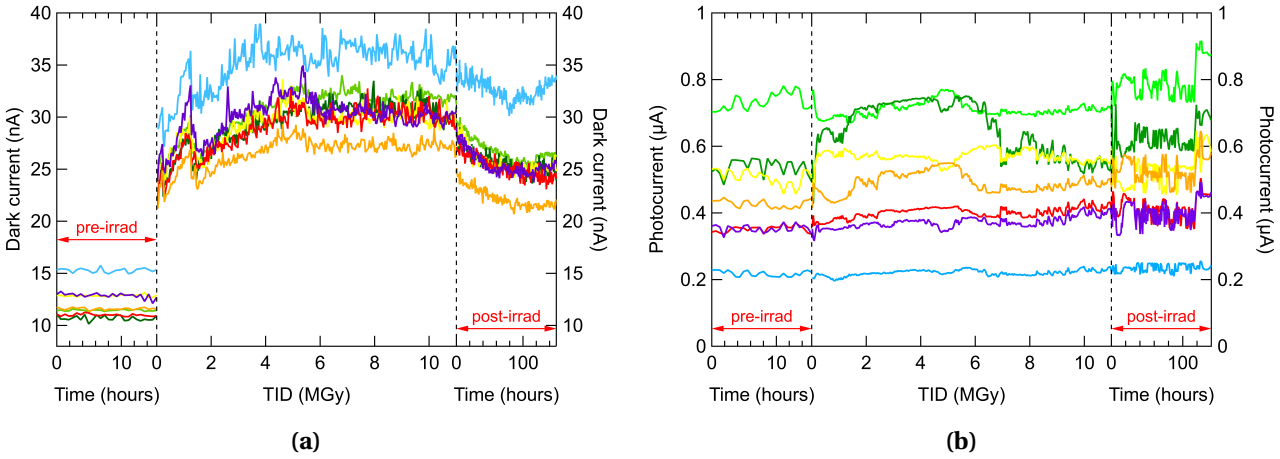

Figure 5.26: (a) Dark currents of VPIN Ge photodiodes during the irradiation with the X-rays. (b) Photocurrents of VPIN Ge photodiodes during the irradiation with the X-rays.

5.2.3 Summary of the X-ray test on photodiodes

Both the dark currents and photocurrents of Ge photodiodes remained unaffected when exposed to X-ray irradiation at doses exceeding those previously reported in the literature. Hence, Ge photodiodes present themselves as a reliable choice for optoelectrical conversion in environments featuring ionising irradiation.

Chapter 6

Evaluation of radiation damage due to NIEL in SiPh devices[1]

Devices and components installed in the inner-most detectors of the HL-LHC will have to withstand a neutron fluence of at least $1.6 \times 10^{16}\,\mathrm{n_{eq}/cm^2}$. In order to test the radiation hardness of SiPh devices to non-ionising radiation damage, two neutron tests were performed, one on modulators and the other on Ge photodiodes and the shunt waveguide. The irradiation facility was the Neutron Irradiation Facility (NIF) [172] at the Cyclotron Resource Center (CRC) in Louvain-La-Neuve, Belgium [173]. A neutron beam at this facility is a secondary beam produced as a nuclear reaction when the 50 MeV deuteron[2] (d) beam hits the beryllium (Be) target:

$$^{9}\mathrm{Be} + \mathrm{d} \rightarrow \mathrm{n} + \mathrm{X} \tag{6.1}$$

The products of such a reaction are a neutron beam (n) and other particles (X). A filter placed behind the target successfully removes charged particles, low-energy neutrons and most of the $\gamma-$rays. The contamination of the neutron beam with the $\gamma-$rays is 2.4%, and for other particles, it is less than 0.1% [174]. After the target, the continuous neutron beam remains with an energy spectrum ranging from 15 to 25 MeV and the centre on 20.4 MeV [174], [175] and the hardness factor (κ) of 1.95 [176]. Accordingly, the 1 MeV equivalent neutron fluence for the 20 MeV neutrons is:

$$\Phi_{\mathrm{eq}}^{1\,\mathrm{MeV(n)}} = 1.95 \cdot \Phi\,[20\,\mathrm{MeV\,n}] \tag{6.2}$$

In Figure 6.1, a neutron beam line located at NIF is shown. Figure 6.1a displays the pipe coming from the ceiling through which the deuteron beam travels to the Be target. At the end of the beam line, after the particle filter, DUT boards ready for irradiation are located. During the same test, several boards were irradiated simultaneously by being arranged one after the other. As shown in Figure 6.1b, in both tests, the SiPh board was the first one in the row, closest to the particle filter. The distance between the particle filter plate and the Be target is 1.5 cm. The neutron beam size at this point is approximately 2 cm. The radius of the beam is calculated as a distance from the centre of the beam at which the beam flux falls down to 80% of the maximum value. The diameter of the beam is big enough to cover the whole area of the PICv2, even at the closest point to the filter plate. The room with the beamline is effectively isolated from the rest of the facility with thick

[1] Parts of this chapter are published in: L. Olanterä, C. Scarcella, **M. Lalović** et al., "*Effects of High Fluence Particle Irradiation on Germanium-on-Silicon Photodiodes*," in IEEE Transactions on Nuclear Science, doi: 10.1109/TNS.2023.3327434.

[2] The deuteron is the nucleus of deuterium (^{2}H) and it contains one neutron and one proton.

walls, establishing a radiation-free zone outside of these walls. Within the radiation-free zone, all instruments required for the characterisations of DUTs are positioned. Between the measurement setup and the DUTs, 50 m long cables and optical fibres were placed.

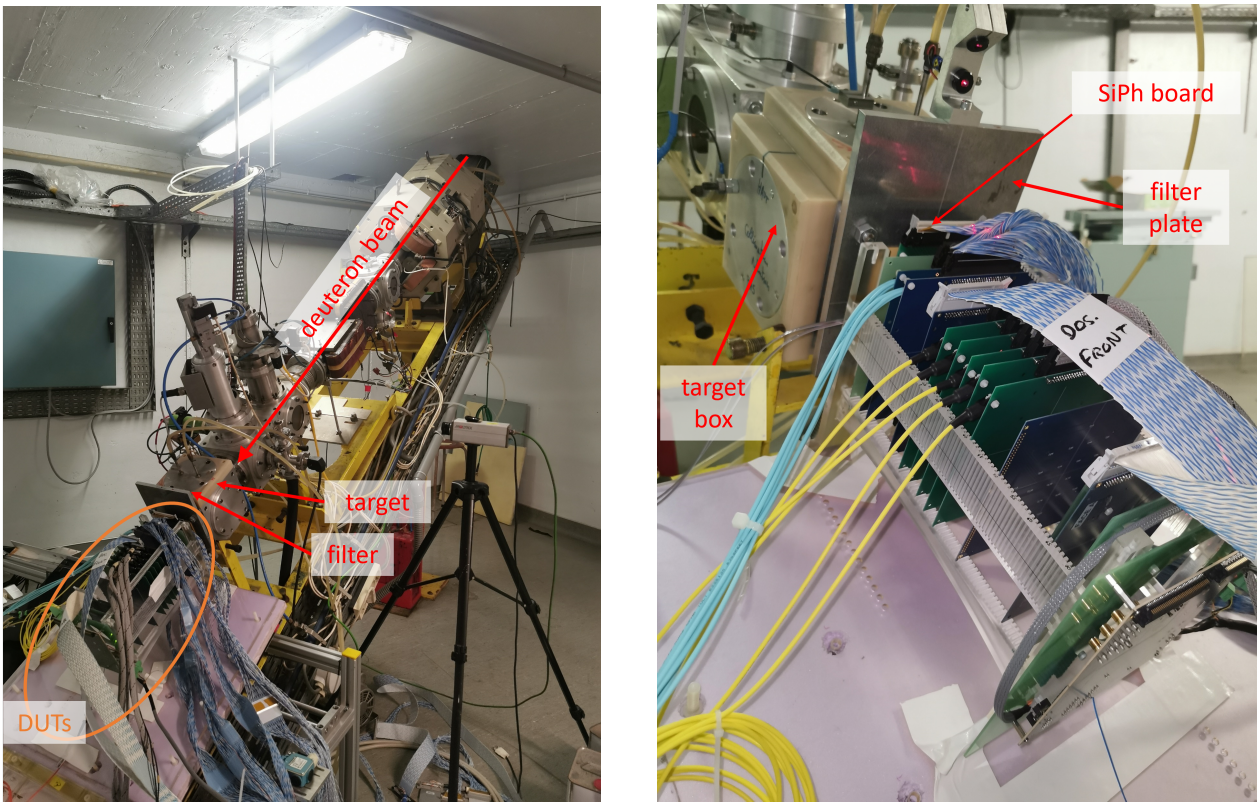

(a) **(b)**

Figure 6.1: (a) Photograph of the high flux neutron beamline at Neutron Irradiation Facility (NIF) at the Cyclotron Resource Center (CRC) in Louvain-La-Neuve, Belgium (b) The PCB boards were placed in front of the neutron beam one after each other. The SiPh board with the PICv2 was installed first in the line, closest to the target.

6.1 Modulators

In May 2022, a 35-hour neutron test was executed on SiPh modulators situated on Scheme #1 of PICv2. The SiPh board was positioned at 1.6 cm away from the filter plate for the duration of the test, resulting in a distance of 3.1 cm between the SiPh board and the target. The beam diameter at this specified distance from the target was calculated to be 2.35 cm. The fluence rate, presumed to be uniform across the entire chip, was determined to be 1.03×10^{15} n/cm^2/h. The total fluence to which the devices on the PICv2 were exposed to was 3.6×10^{16} n/cm^2. Along with the neutrons, approximately 2.2×10^{-14} kGy/n/cm^2 [177] of TID from γ-ray was present, amounting to a total of 790 kGy. According to the findings presented in Chapter 5, it is imperative to acknowledge that this level of ionising irradiation is non-negligible and it will be taken into consideration when presenting the results.

The experimental setup used in this test is illustrated in Figure 6.2. It is evident that the setup closely resembles those implemented in X-ray experiments with one major difference. The different configurations of the beamline and the layout of the irradiation room were space-restricting and

the implementation of a Peltier cooler or a similar system for the temperature regulation of the whole board and the chip was impossible. Furthermore, it should be noted that all micro-heaters as well as PT100 sensor were powered and measured through a 4-wire measurement method. This methodology was necessary to compensate for voltage drops that were observed due to extended cable lengths. Consequently, precise temperatures for each ring modulator were determined from the corresponding power.

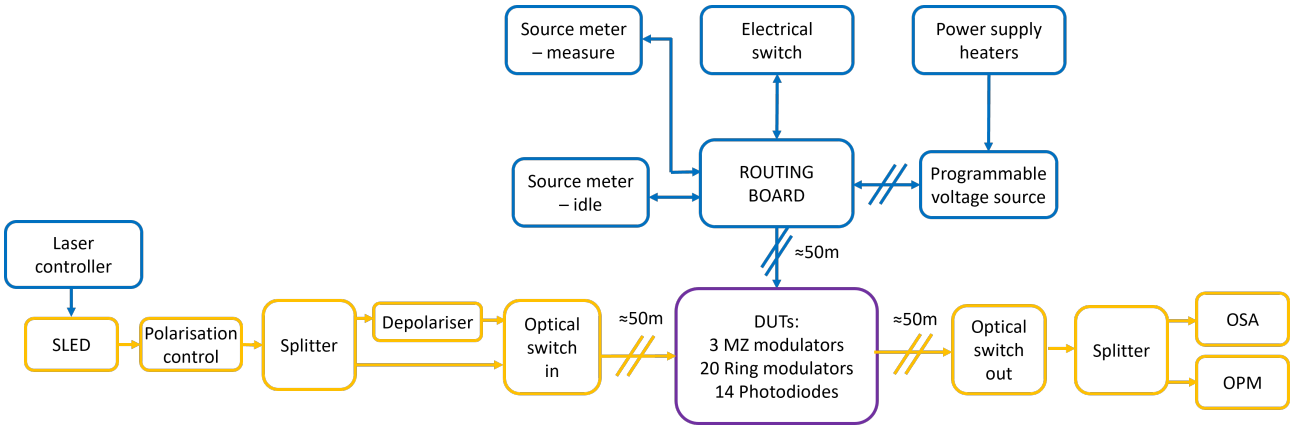

Figure 6.2: Scheme of the setup used for the neutron test conducted in May 2022.

The test included three distinct phases: pre-irradiation, irradiation, and post-irradiation. Throughout all these phases, data acquisition was conducted at approximately 40-minute intervals. First, measurements were executed over a 20-hour period to assess the stability of the measurement setup. Afterwards, upon closure of the door to the room with the beamline and the start of the deuteron beam, the second phase of measurements began for 35 hours. Following the deuteron beam deactivation, the post-irradiation measurements were initiated. Throughout this period, the room remained sealed due to the radioactive nature of its contents. Post-irradiation measurements took place over the following ten days.

Figure 6.3 shows the temperature data recorded by PT100 sensor. Notably, during the pre-irradiation measurements, the temperature was stable at 26.4°C. Upon activation of the beam, the temperature exhibited a sudden increase to 27°C, reaching 27.7°C by the end of the irradiation phase. After deactivation of the beam, the temperature gradually decreased to the pre-irradiation level. However, a gradual temperature rise was recorded over the following ten days. Despite the

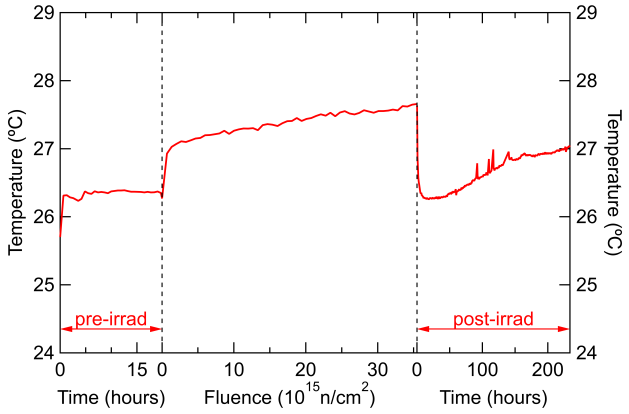

Figure 6.3: Temperature of the DUT board during the pre-irradiation, irradiation, and post-irradiation phase.

absence of a system for temperature regulation, the variations of the temperature during the test were confined within 1°C. Therefore, these fluctuations are considered non-significant for the modulator measurements.

6.1.1 Mach-Zehnder modulators

Figure 6.4 depicts the responses of two Mach-Zehnder modulators during the conducted test. Throughout the experiment, the MZMs underwent reverse biasing at voltages of 0 V, 1 V, or 2 V, while simultaneously capturing optical spectra. All other devices on the chip, including the remaining MZM, were maintained at an idle voltage with an average of 1 V. The modulation efficiencies presented herein represent the resulting phase shift when 0 V and 1 V bias voltages are applied to the modulator contacts, normalised relative to the values observed during the pre-irradiation phase.

Following the start of irradiation, both MZMs exhibited degradation, with their modulation efficiencies dropping below 40% of the initial values after reaching a fluence of 3.6×10^{16} n/cm^2. Specifically, the shallow-etched Mach-Zehnder modulator displayed a slightly better modulation efficiency, 30%, while the deep-etched counterpart registered only 23% of the pre-irradiation values. In the post-irradiation phase, the modulation efficiencies continued to gradually degrade, reaching the stable value of approximately 20% of the initial values.

As mentioned before, the effect of ionising irradiation should be taken into account. In this particular test the TID of 790 kGy was accumulated over the period of 35 hours. resulting in an approximate dose rate of 6.2 Gy/s. In Section 5.1.3.1, it has been demonstrated that lower dose rates can influence the radiation hardness of Mach-Zehnder modulators. In this neutron test, the dose rate of γ-rays was similar to one in the third X-ray test.[3] The MZM subjected solely to ionising radiation at a comparable dose rate exhibited a 20% reduction in modulation efficiency for the deep-etched MZM and just 5% for the shallow-etched counterpart at the same TID. This observation suggests that the predominant loss in this neutron test can be attributed to neutron exposure rather than impurities within the neutron beam. Furthermore, the influence of etching depth on the radiation hardness of the MZMs, as observed in the case of ionising radiation, is not as pronounced in the case of neutron irradiation.

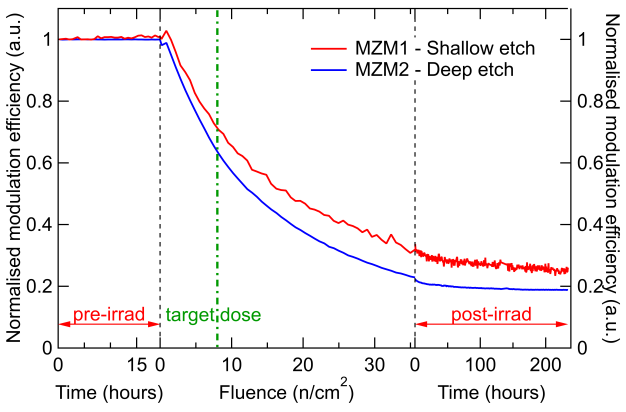

Figure 6.4: Normalised modulation efficiencies of MZMs with different etching depths during the irradiation up to 3.6×10^{16} n/cm^2.

[3]The energies of the two beams were different and the dependence of the energy of ionising radiation on the radiation hardness of SiPh devices was not covered by this thesis.

6.1.2 Ring modulators

Although the response of Mach-Zehnder modulators to neutron irradiation has been partially explored in previous studies [163], the radiation hardness of ring modulators to non-ionising irradiation has not been previously investigated. During this test, eight high doping ring modulators (RM2, RM6, RM11, RM12, RM15, RM18, RM19 and RM20) were subjected to temperatures ranging from 25°C to 200°C while being irradiated up to a fluence of 3.6×10^{16} n/cm^2. Specifically, RM11 at 25°C, RM12 at 40°C, RM6 at 60°C, RM20 at 75°C, RM19 at 100°C, RM2 at 125°C, RM18 at 150°C and RM15 at 200°C. Similarly to the Mach-Zehnder modulators, the RMs underwent reverse biasing at voltages of 0 V, 1 V, or 2 V. Optical spectra were simultaneously captured, while the remaining devices were maintained at an idle voltage averaging 1 V. The modulation efficiencies presented here are the resulting phase shift when 0 V and 1 V bias voltages are applied to the modulator contacts, normalised relative to values observed during the pre-irradiation phase.

Figure 6.5 illustrates the normalised modulation efficiencies observed during the test. At the beginning of irradiation, a marginal increase in modulation efficiencies is observed for some ring modulators. The increase in modulation efficiency can occur if the defects are formed around the structure in such a way that it results in better confinement of the light in the waveguide. This effect was also recorded during the X-ray tests. After the fluence of 1.5×10^{16} n/cm^2, two distinct groups emerge. The first group, containing ring modulators operated at temperatures above 150°C, exhibited less degradation compared to the second group operated at temperatures below 150°C. Ring modulators operated at higher temperatures experienced 5% less degradation when compared to those at lower temperatures after reaching the maximal fluence of 3.6×10^{16} n/cm^2. All ring modulators, regardless of their operating temperature, maintained modulation efficiencies within the range of 70% to 80% of the initial values.

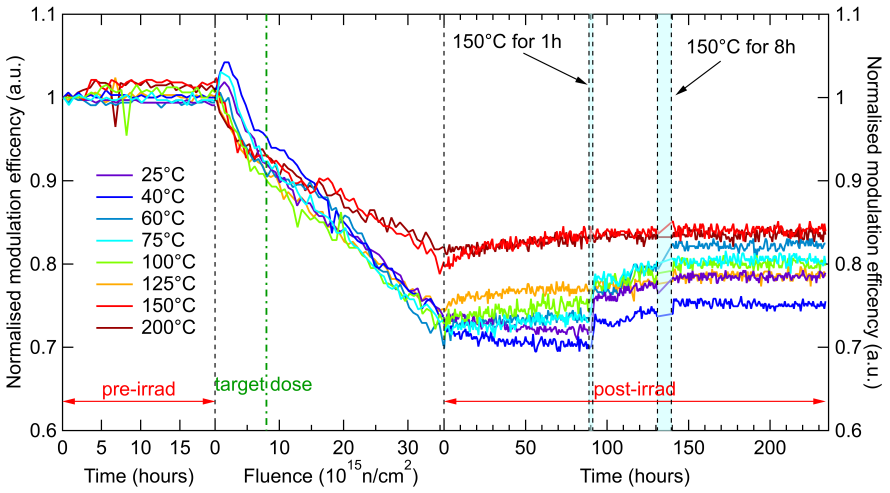

Figure 6.5: Normalised modulation efficiencies of high doping ring modulators operated at different temperatures between the 25°C and 200°C while irradiated with 20 MeV neutron beam. During the post-irradiation phase, thermal annealing of the ionising radiation was done. (RM11 at 25°C, RM12 at 40°C, RM6 at 60°C, RM20 at 75°C, RM19 at 100°C, RM2 at 125°C, RM18 at 150°C and RM15 at 200°C)

In the post-irradiation phase, the ring modulators were maintained at their initial temperatures for a duration of four days. Some of the observed damage in the devices is attributed to the co-presence of ionising radiation with the neutron beam, as previously explained. As demonstrated in the previous chapter, it is possible to reduce damage caused by ionising radiation through the application of high temperatures. Additionally, to a certain extent, displacement damage can

also undergo annealing at elevated temperatures. Consequently, during the initial period of post-irradiation, a small annealing effect was observed for RMs operated at temperatures exceeding 125°C.

To induce further annealing, after 90 hours under the previous conditions, the micro-heaters of each ring modulator were adjusted to elevate their temperature to 150°C for a duration of 1 hour. The temperature of 150°C was specifically chosen as it was shown in Section 5.1.3.3 that this temperature has induced total recovery in all ring modulators. This expedited the annealing process, even in ring modulators previously operated at lower temperatures. Modulation efficiencies of RMs operated at 25°C and 40°C exhibited an improvement of 5%. Following the one-hour heating regime, all ring modulators were set to the same temperatures as during irradiation. Over the next 40 hours, a small additional annealing was observed. To enhance annealing further, all RMs were heated once again to 150°C for an extended period of 8 hours. No major improvements were recorded during this period. Following the second heating cycle, the RMs were returned to their initial conditions until the end of the test. Regardless of their operational temperatures, all ring modulators reached stable values towards the end of the test. The permanent degradation attributed to the neutron beam was estimated to be in the range of 15-25%. Considering that the delivered fluence to the samples was twice the expected fluence during HL-LHC operation, the high-doping ring modulators exhibited remarkable resilience to non-ionising radiation damage.

In addition to the high-doping ring modulators, four low-doping ring modulators (RM7, RM8, RM9, and RM13) were subjected to four different temperatures: 25°C, 60°C, 100°C, and 200°C. Specifically, RM7 at 25°C, RM13 at 60°C, RM8 at 100°C, RM9 at 200°C. The response of these modulators to neutron irradiation is presented in Figure 6.6. Following the beginning of irradiation, the four curves exhibited distinct degradation slopes, indicating that temperature influences radiation hardness in the case of non-ionising radiation, analogue to ionising radiation. The ring modulator operated at 200°C experienced the least degradation, maintaining 65% of the initial modulation efficiency at the end of irradiation. The ring modulator heated to 100°C exhibited more degradation, with only 40% of the pre-irradiation efficiency remaining. Two ring modulators operated at even lower temperatures encountered the most significant degradation, retaining only 20% of

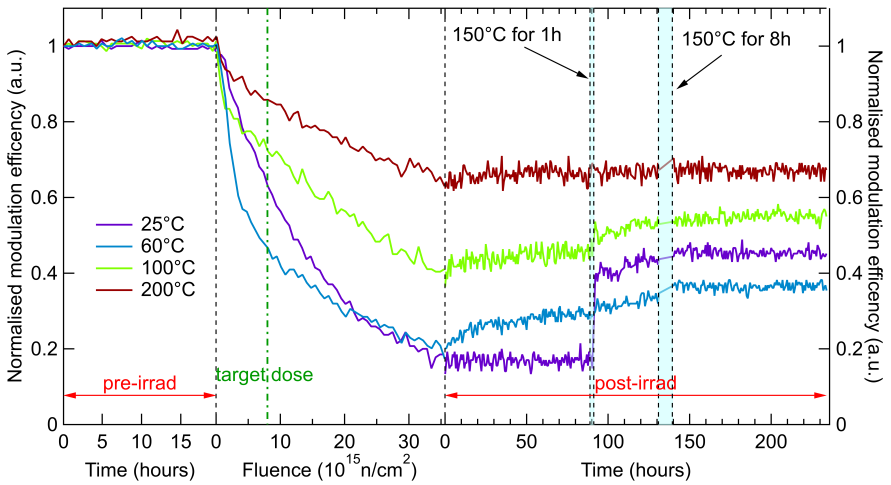

Figure 6.6: Normalised modulation efficiencies of low doping ring modulators operated at different temperatures between the 25°C and 200°C while irradiated with 20 MeV neutron beam. During the post-irradiation phase, thermal annealing of the ionising radiation was done. (RM7 at 25°C, RM13 at 60°C, RM8 at 100°C, RM9 at 200°C)

modulation efficiency.

Following the deactivation of the neutron beam, measurements continued at the same temperatures. Similar to the high-doping ring modulators, all ring modulators were subjected to two heating cycles at 150°C, lasting 1 and 8 hours, respectively. The first heating cycle occurred after 90 hours of post-irradiation, and the second after 130 hours. The purpose of this heating was to anneal ionising radiation damage, as well as some of the unstable defects induced by non-ionising radiation. The most significant annealing was observed in ring modulators operated at 25°C and 60°C, recovering 30% and 20% of their initial modulation efficiency, respectively. Ring modulators at higher temperatures experienced annealing during irradiation, and therefore, the post-irradiation annealing was minimal.

6.1.3 Modulator comparison

Two different modulator types, possessing identical geometric parameters in terms of their cross-section, such as a W_{Dop} width of 100 nm, the same etching depth, and doping concentration, are compared under identical conditions, specifically at room temperature up to the same fluence. Throughout the irradiation, both modulators exhibited comparable levels of degradation with nearly identical slopes. This observation emphasises that radiation hardness is not essentially tied to the modulator type.

However, the inability to apply heating to Mach-Zehnder modulators places them at a disadvantage compared to ring modulators. In the post-irradiation process, subjecting the ring modulator to only a one-hour heating cycle at 150°C induced a significant annealing effect, restoring 30% of its initial modulation efficiency and leaving the modulator with just under 50% of the pre-irradiation value. In contrast, the Mach-Zehnder modulator exhibited only 20% of the pre-irradiation efficiency at the end of the test. Moreover, the design of ring modulators allows the utilisation of higher doping concentrations compared to Mach-Zehnder modulators, and the integration of micro-heaters, which both can enhance radiation hardness. Consequently, considering all mentioned above, ring modulators appear as the more favourable choice for radiation-hard SiPh modulators.

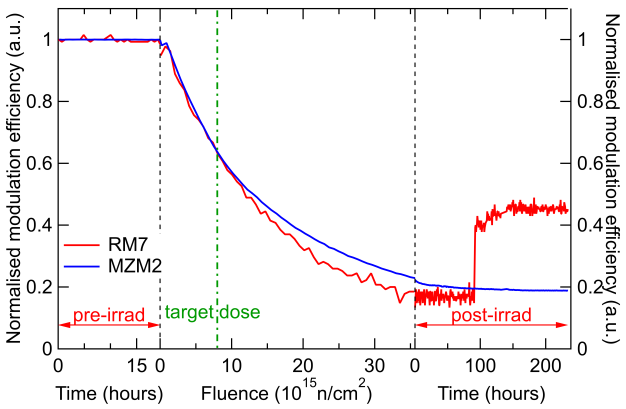

Figure 6.7: Comparison of normalised modulation efficiencies of low doping ring modulator and Mach-Zehnder modulator with the same cross-section while operated at room temperature.

6.1.4 Summary of the neutron test on modulators

Under non-ionising particle irradiation, high-doping ring modulators demonstrated only a 10% reduction in modulation efficiency after reaching the targeted dose of 1.6×10^{16} n(1 MeV)/cm^2 and 20-25% after the maximum fluence of 3.6×10^{16} n(20 MeV)/cm^2. In contrast, Mach-Zehnder modulators have shown more degradation, exhibiting approximately 60% of initial modulation efficiencies after the target dose. Ring modulators with low doping showed the same level of degradation as Mach-Zehnder modulators. Damage associated with non-ionising radiation in SiPh modulators was shown to be less pronounced than damage caused by ionising radiation.

6.2 Photodiodes

In May 2021, a 34-hour neutron test was conducted on germanium photodiodes located on Scheme #2 of PICv2. Throughout the test, the SiPh board remained positioned 1.9 cm away from the filter plate, resulting in a distance of 3.4 cm between the SiPh board and the target. The beam diameter at this specified distance from the target was determined to be 2.4 cm. The fluence rate, assumed to be uniform across the entire chip, was calculated to be 8.64×10^{14} n/cm^2/h. The total fluence to which the devices on the PICv2 were exposed was 2.93×10^{16} n/cm^2. Along with the neutrons, a total of approximately 2.2×10^{-14} kGy/n/cm^2 of TID from γ-rays was present, resulting in a total of 645 kGy. Considering previous evidence indicating that ionising radiation does not induce degradation in Ge photodiodes, the presence of ionising radiation can be considered negligible in this context.

The experimental setup employed in this test is illustrated in Figure 6.8. The primary optical source in the experiment was a *Thorlabs* SLED with a central wavelength of 1550 nm, an optical bandwidth of 90 nm, and an optical power of 2 mW. The SLED was controlled by a *Pilot PC 500* laser diode controller. The light from the SLED was amplified using a *LEA Photonics* Erbium-Doped Fibre Amplifier (EDFA). As remote control of the EDFA amplification was not feasible, a *JDSU mVOA-A2* attenuator was incorporated into the optical chain to provide an additional degree of freedom. The transmitted light was subsequently depolarised and divided using an 8-way splitter. Five fibres were directed to five photodiodes, while one fibre was reserved for an optical shunt. The remaining two fibres were not utilised. The light passing through the optical shunt was measured using an *Agilent 8163B* Optical Power Meter.

In order to establish electrical connections with the PIC, two *Keithley 2410 Source Meters* and a multichannel electrical switch (*Keysight 34970A*) were employed. One source meter was designated for the assessment of the electrical properties of the photodiodes, while the other was utilised to apply a constant reverse bias voltage of 1 V (i.e. idle voltage). The electrical switch was configured to enable each channel to alternate between the measurement and idle states. While one device operated in the measurement regime, all other devices remained in the idle state. In addition to the SiPh devices on the PIC, the PT100 sensor was also connected and measured using the 4-wire measurement method.

All instruments within the setup were interconnected in parallel via GPIB cables and subsequently linked to the computer through a *National Instruments* GPIB-to-USB converter. The procedures for controlling the instruments, as well as the code for data acquisition and the functions for subsequent analyses, were written in Igor Pro. The measurement procedure involved acquiring photocurrents, dark currents of the photodiodes, and shunt optical power. The measurements were automated and repeatedly conducted in an infinite loop during the irradiation. A single

measurement loop for assessing all devices required approximately 1 minute. However, 10-minute idle intervals were incorporated between successive measurements. During these intervals, all photodiodes were subjected to a reverse bias of 1 V.

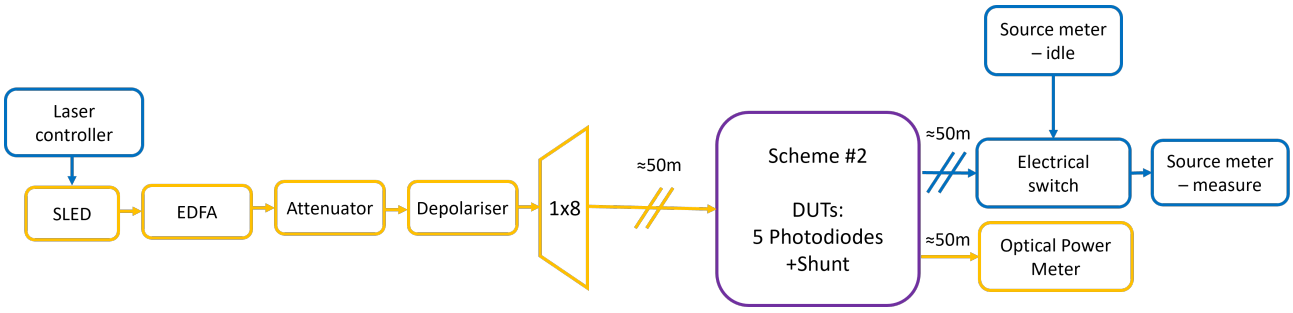

Figure 6.8: Scheme of the setup used for the neutron test conducted in May 2021.

The test contained three distinct phases: pre-irradiation, irradiation, and post-irradiation. In the beginning, measurements were conducted over a 15-hour period to evaluate the stability of the measurement setup. Subsequently, with the closure of the door of the room containing the beamline and the start of the deuteron beam, the second phase of measurements commenced and continued for 34 hours. Upon deactivation of the deuteron beam, the post-irradiation measurements were initiated, and this phase continued for the subsequent five days. The room remained closed during this period due to the radioactive nature of its contents.

Figure 6.9 illustrates the temperature data recorded by the PT100 sensor. Throughout the pre-irradiation measurements, the temperature remained at approximately 22°C. Upon the activation of the beam, a sudden temperature increase to 22.4°C was observed, reaching 22.8°C by the end of the irradiation phase. Following beam deactivation, the temperature gradually reverted to the pre-irradiation level. However, a continuous temperature rise was documented over the following five days. The recorded temperature variations during the entire test remained within 1°C. Consequently, these fluctuations are considered non-significant for the measurements.

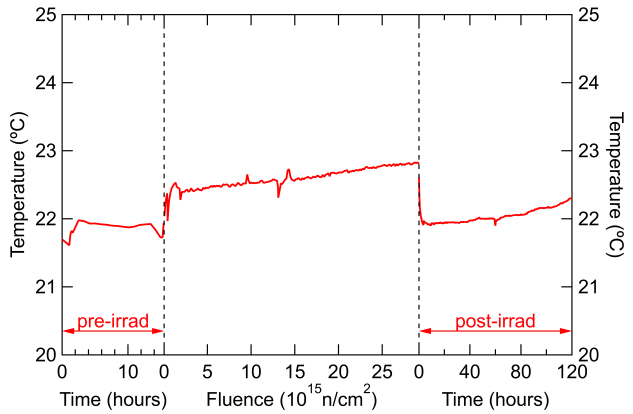

Figure 6.9: Temperature of the DUT board during the pre-irradiation, irradiation, and post-irradiation phase.

6.2.1 Dark current

Section #2 contained five Ge photodiodes, two lateral PIN (LPIN1-2) and three vertical PIN (VPIN1-3) photodiodes. Even though they have small differences in their dimensions and structure,

the photodiodes were provided as building blocks by the foundry and no further information on exact geometry, dimensions, and doping levels is available.

Figure 6.10 displays the dark currents of the Ge photodiodes when subjected to a 1 V reverse bias voltage. Dark current measurements were conducted with the SLED turned off. Pre-irradiation measurements show that four photodiodes exhibit dark currents below 30 nA, while one photodiode (LPIN1) demonstrates a notably higher dark current of 300 nA. With the start of irradiation, the majority of dark currents exhibited a gradual increase, except for LPIN1, which showed a slight reduction in its dark current. At the termination of irradiation and following exposure to the maximum neutron fluence, all dark currents remain below 1 μA. This will not pose a problem for the operation of optical links, as transimpedance amplifier circuits designed for the LHC can handle significantly larger leakage currents [178].

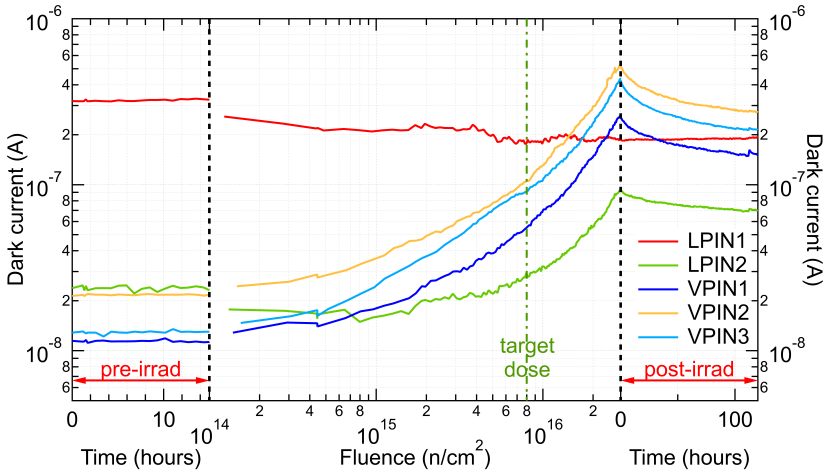

Figure 6.10: Dark currents of Ge photodiodes when being irradiated with a 20-MeV neutron beam.

After the irradiation, the photodiodes underwent continuous monitoring under identical conditions for a duration of five days. During this period, a reduction in dark currents was observed, and approximately 50% of the previously obtained dark current increase was recovered. Notably, LPIN1 exhibited a distinctive behaviour, manifesting neither an increase in the dark current nor any noticeable annealing effect. The anomalous behaviour of LPIN1 could be explained if the recorded dark current was attributed to another form of leakage current different from the typical dark current, thereby making this sample insensitive to displacement damage. However, due to the limited information available concerning the photodiode's structure or production processes, a thorough investigation could not be done.

6.2.2 Responsivity

Figure 6.11 presents the responsivity of Ge photodiodes, biased with 1 V of reverse bias voltage and normalised to pre-irradiation values. The photocurrents used for calculating responsivities were in the order of several hundred of μA, ensuring that the previously demonstrated increase in dark currents did not significantly impact the measurements. Upon activation of the neutron beam, the responsivities of all photodiodes exhibited a constant decrease, with subtle differences becoming apparent after a total neutron fluence of 2.93×10^{16} n/cm^2. Particularly, the lateral PIN photodiodes (LPIN1 and LPIN2) displayed more pronounced degradation, with an approximate 35% reduction in their initial responsivity. In contrast, VPIN2 and VPIN3 appeared to be the most resilient candidates,

retaining 83% of their initial responsivity. After the end irradiation, measurements continued for the subsequent 120 hours, showing a minimal recovery of approximately 5% in all photodiodes.

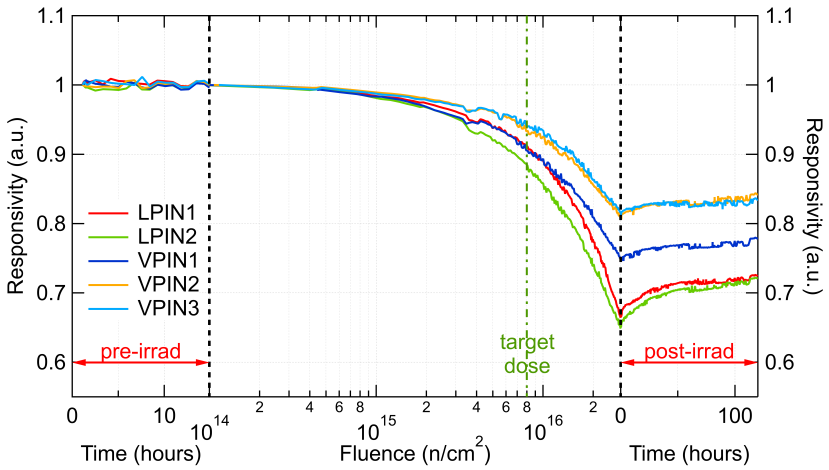

Figure 6.11: Responsivity of Germanium photodiodes in SiPh technology when being irradiated with a 20-MeV neutron beam.

Furthermore, the layout of the PIC was arranged in a way that from the grating couplers to the photodiodes the light travelled through approximately 1 mm of 450 nm wide strip waveguides. A potential contributor to the observed decrease in photocurrents may be variations in optical power reaching the photodiodes. To quantify the loss over the waveguide section resulting from the neutron beam, measurements were conducted on the waveguide shunt. Prior studies have demonstrated that ionising radiation does not significantly impact loss in Si waveguides. However, a notable change in optical power induced by neutrons was evident throughout the irradiation, as illustrated in Figure 6.12. The length of the shunt was 3.2 mm, and the estimated loss in Si waveguide per 1×10^{16} n(1 Mev)/cm^2 of neutron fluence was determined to be 0.13 dB/mm. During the post-irradiation measurements, a small increase in optical power was observed. This increase is a partial cause of the recovery recorded in photodiodes.

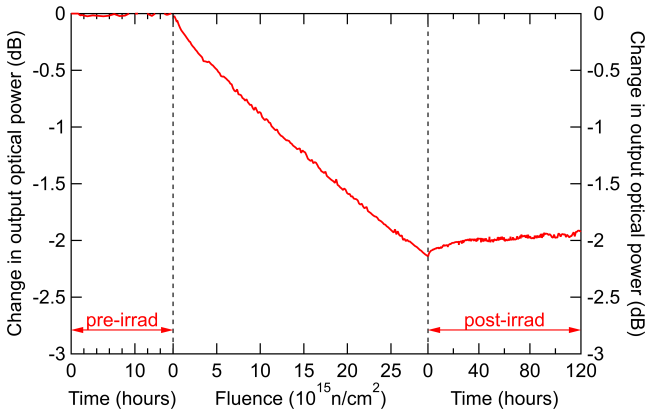

Figure 6.12: Change in optical power at the output of the shunt waveguide long 3.2 cm when irradiated with a neutron beam.

To account for the observed loss, the previously measured responsivities were corrected. The loss, as depicted in Figure 6.12, was appropriately scaled based on the individual lengths of the

waveguides leading to each photodiode and subsequently integrated into the responsivity calculations. Figure 6.13 illustrates the estimated changes in photodiode responsivity when the increase in waveguide loss is considered. With this correction, the decrease in responsivities of LPIN1 and LPIN2 is reduced to less than 25% after reaching the maximum neutron dose of 2.93 $\times$ 10^{16} n/cm^2. The two most robust samples (VPIN2 and VPIN3) exhibited a loss of less than 5% of their initial responsivity, indicating remarkable hardness to non-ionising radiation. Additionally, a subtle recovery is still noticeable in all samples during the post-irradiation period.

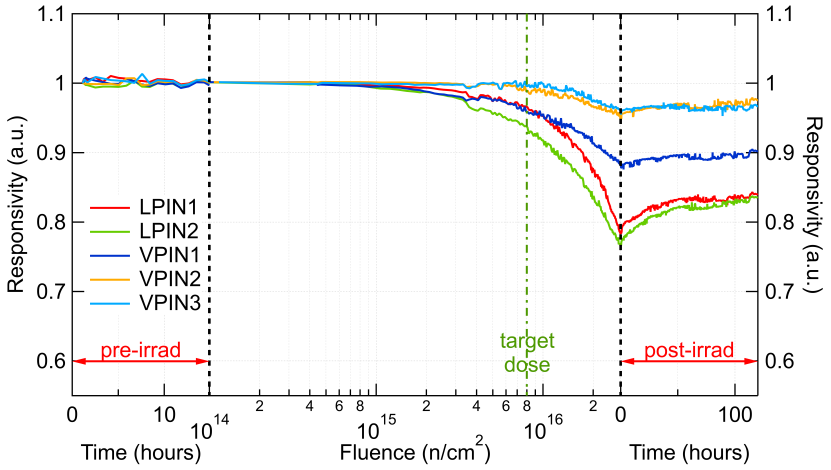

Figure 6.13: Responsivity of Germanium photodiodes in SiPh technology with waveguide loss correction when being irradiated with a neutron beam.

6.2.3 Comparison with other technologies

The photodiodes currently utilised in the current optical links at CERN for the Rx side are discrete InGaAs photodiodes. However, these InGaAs photodiodes have demonstrated insufficient radiation tolerance for the expected radiation levels during the end phase of HL-LHC [179]. Figure 6.14 provides a comparison of the responsivities of discrete InGaAs photodiodes and integrated Ge photodiodes. The results contain photodiodes from both iterations of the PIC, PICv1 and PICv2. All photodiodes were irradiated with 20-MeV neutrons in Louvain-la-Neuve in the separate tests. For the Ge photodiodes on PICv2, results for the best candidate with and without waveguide loss correction are presented, while results for PICv1 are without waveguide loss correction.

The responsivity of the InGaAs photodiode exhibited a more rapid degradation compared to the integrated Ge photodiodes, reaching 65% of its initial responsivity after a neutron fluence of 4.5 $\times$ 10^{15} n/cm^2, the maximum fluence in this test. In contrast, the Ge photodiode on PICv1 retained approximately 80% of its responsivity after a fluence of 7 $\times$ 10^{15} n/cm^2. However, the Ge photodiodes from the PICv2 demonstrated superior performance, maintaining 80% of their initial responsivity even after exposure to a neutron fluence as high as 3 $\times$ 10^{16} n/cm^2. This demonstrates that improvements in production processes by the foundry can enhance the radiation hardness of Ge photodiodes by a factor of four.

The neutron irradiation test results demonstrate that Ge photodiodes exhibit high tolerance to displacement damage, with minimal degradation in terms of responsivity and dark current. However, a substantial increase in waveguide losses was observed during irradiation. Nevertheless, this loss can be reduced by employing shorter waveguides leading to photodiodes or other SiPh

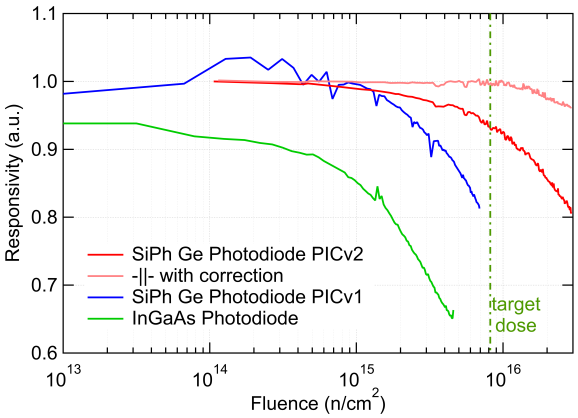

Figure 6.14: Comparison of responsivity of Germanium photodiodes in SiPh technology with discrete InGaAs photodiode.

devices. Even with the observed loss in waveguides, the integrated Ge photodiodes displayed significantly better performance compared to other photodiodes.

6.2.4 Summary of the neutron test on photodiodes

Germanium photodiodes show minimal impact when exposed to non-ionising particles. Even after being subjected to a total fluence four times higher than expected during the last run of the HL-LHC, the top-performing germanium photodiode sample only experiences a slight decrease in responsivity. This marks a significant improvement, considering that discrete InGaAs photodiodes currently used in the LHC can only withstand one-tenth of this neutron fluence.

Integrated waveguide irradiated together with Ge photodiodes experienced optical power loss when subjected to non-ionising particles. The observed loss increases linearly with fluence, at a rate of 0.13 dB/mm per 1×10^{16} n(1 MeV)/cm^2 of neutron fluence. With the compact chip design, this loss can effectively be minimised, making it negligible for the optical link's operation.

Chapter 7

Conclusions

The forthcoming years will witness a series of upgrades of the Large Hadron Collider at CERN. The devices and components currently in use are reaching the end of their lifetime, and they are incapable of meeting the demands imposed by the High Luminosity phase of LHC. The inadequacy of the current components arises primarily from insufficient radiation tolerance, making them incapable of withstanding the entire operational lifespan of the LHC.

This thesis addressed the challenges associated with implementing SiPh optical links in harsh radiation environments. Radiation effects in SiPh modulators, germanium photodiodes and waveguides, all crucial for the operation of the optical links, were investigated. Before the irradiation tests, the characterisation of the aforementioned components was done. Afterwards, multiple SiPh chips were irradiated during three X-ray and two neutron tests to examine the impact of radiation on SiPh devices.

For the first time, SiPh ring modulators were subjected to ionising radiation (X-rays) and non-ionising radiation (neutrons) at ultra-high doses relevant to High-Luminosity Large Hadron Collider operations, precisely 10 MGy and 1.6×10^{16} n(1 MeV)/cm^2, respectively. The administered doses to SiPh Mach-Zehnder modulators and germanium photodiodes exceeded previously reported levels in literature.

Comparative analysis revealed that ring modulators exhibit superior resilience to radiation in comparison to Mach-Zehnder modulators, withstanding target doses of 10 MGy of ionising and 1.6×10^{16} n(1 MeV)/cm^2 of non-ionising radiation. Furthermore, ring modulators at high temperatures exhibit increased resilience to lower dose rates of ionising radiation, in contrast to Mach-Zehnder modulators that experience more pronounced degradation at lower dose rates.

The increased doping concentration in the waveguide core of ring modulators, as well as, the elevated doping concentration in the p-doped slab (contact p++ doping instead of p+ doping), improved their radiation tolerance. Since the ionising irradiation creates the pinch-off region in the p-doped Si, the more free carriers in this type of Si make the phase shifter more resistant to the trapped charge generated by the X-rays. The design of ring modulators permits higher doping concentrations compared to the lower concentrations required for the correct operation of Mach-Zehnder modulators.

The other geometrical parameters of ring modulators, such as ring radius, W_{Dop} length, slab length, trough port gap, and drop port gap, do not have an influence on the radiation hardness of these devices.

The operating temperatures of the SiPh ring modulators showed a significant influence on radiation hardness. At temperatures exceeding 125°C, degradation after 11 MGy was minimal

since the temperature annealing rate was higher than degradation, resulting in stable modulation efficiency. Modulators operated at high temperatures reached a stable state after 2 MGy, maintaining the same efficiency until the maximum dose of 11 MGy. Furthermore, room temperature modulators showed promising results, although the absence of thermal annealing at room temperatures will lead to degradation with a higher Total Ionising Dose. The ring modulators at middle-range temperatures exhibited the most degradation. However, in the post-irradiation period, all ring modulators operated at a temperature higher than 60°C experienced a thermal annealing effect. With closer examination, temperatures as high as 150°C gave full recovery to all RMs regardless of the level of degradation at the end of irradiation. During periods of shutdowns, optical links can be subjected to additional heating, in order to accelerate the recovery of TID damage in ring modulators.

Under neutron beam exposure, high doping ring modulators displayed only 10% less modulation efficiency after the target dose of 1.6×10^{16} n(1 MeV)/cm^2 and 20-25% after the maximum fluence of 3.6×10^{16} n(20 MeV)/cm^2. In contrast, Mach-Zehnder modulators were shown to be less resistant, exhibiting approximately 60% of initial modulation efficiencies after the target dose. This was also the case with the ring modulators with the same doping. Damage associated with non-ionising radiation in SiPh modulators was shown to be less pronounced than damage caused by ionising radiation, as was predicted.

Having in mind other disadvantages of Mach-Zehnder modulators when compared to ring modulators, namely the relatively large footprint (~1 mm), requiring driving voltages of 1.5 to 2 V to achieve enough modulation, and the absence of micro-heaters, ring modulators are considered the better option for SiPh links. Although ring modulators exhibit certain weaknesses, such as increased sensitivity to production processes and temperature variations, these sensitivities can be compensated and exploited positively through the implementation of micro-heaters. In future optical links at CERN, a thermal control loop for stabilisation of their operation is planned as a solution for this problem [180], [181].

Ge photodiodes remained unaffected when irradiated with X-rays. Even though the irradiation with the neutrons left more impact on such devices than X-rays, they were still highly tolerant to radiation damage. After a total fluence that was four times higher than expected in the last run of the HL-LHC, the best-performing germanium photodiode sample shows only a minor decrease (several per cent) in responsivity. This represents a significant advancement, as discrete InGaAs photodiodes currently utilised in the LHC can withstand ten times less neutron fluence. Furthermore, Ge photodiodes on PICv2 displayed the same responsivity as the Ge photodiodes from PICv1 when irradiated to four times less fluence, i.e. the Ge photodiodes from PICv2 are four times more resistant than the ones from PICv1.

Integrated waveguides exhibited resilience to ionising radiation but experienced optical power loss when subjected to non-ionising particles. The measured loss is linear with fluence, measuring 0.13 dB/mm per 1.6×10^{16} n(1 MeV)/cm^2 of neutron fluence. With the compact chip design, this loss can effectively be minimised, making it negligible for the optical link's operation.

Based on the results gathered throughout the experiments, a new SiPh test chip (PICv3) has been designed and sent for fabrication. The design emphasises both 1310 nm and 1550 nm wavelengths, and various devices are configured to be compatible with either wavelength. Given their superior overall results in terms of radiation hardness, ring modulators are prioritised in the new chip and all of them are equipped with integrated micro-heaters. The chip will also feature several designs of Ge photodiodes, as well as waveguides of different lengths and cross-sections. As a potential prototype for future optical links, the chip incorporates several designs of Wavelength Division Multiplexing circuits operated both at C-band and O-band wavelengths. These circuits are intended to be

compatible with the co-integration of Application-Specific Integrated Circuits (ASICs) essential for controlling optical transmitters.

Some further research is necessary to ensure the entire optical links are fully operable. The other types of radiation effects in SiPh devices, such as combined ionising and non-ionising radiation effects (proton beam) or single-event effects, will need to be investigated. Recent studies have revealed the existence of optical single-event transients (OSETs) [105], a new class of effects to be studied in SiPh structures. Moreover, an important concern regarding the operation of ring modulators is the diverse ambient conditions present in different parts of the detectors where these devices will be deployed. As the optical links will be utilised in detectors operating under different thermal conditions, ranging from -30°C to 60°C, specific operational procedures must be developed to ensure ring modulators operate within their optimal temperature range. Additional tests, especially at temperatures below 25°C, should be conducted. Devices should also undergo testing in different humidity levels and an elevated magnetic field environment, as present in LHC experiments.

In conclusion, the work on the SiPh optical links in this thesis has demonstrated that SiPh modulators, specifically SiPh ring modulators together with Ge photodiodes and waveguides, are capable of surviving and operating in radiation-harsh environments such as HL-LHC. With the correct mode of operation, ring modulators will be able to endure even higher levels than currently necessary by HL-LHC and will be competent for use in new accelerators such as the Future Circular Collider [182] at CERN. The results of this research can be useful in other SiPh technology applications besides high-energy physics experiments, including the space industry, where exposure to radiation is expected and optical links are required.

Bibliography

[1] *Home | CERN*. [Online]. Available: https://home.web.cern.ch/ (visited on 15/01/2023).

[2] L. Evans and P. Bryant, „LHC Machine", *Journal of Instrumentation*, vol. 3, no. 08, S08001, Aug. 2008, ISSN: 1748-0221. DOI: 10.1088/1748-0221/3/08/S08001.

[3] O. Brüning, H. Burkhardt and S. Myers, „The large hadron collider", *Progress in Particle and Nuclear Physics*, vol. 67, no. 3, pp. 705–734, Jul. 2012, ISSN: 01466410. DOI: 10.1016/j.ppnp.2012.03.001.

[4] M. Vretenar, J. Vollaire, R. Scrivens, C. Rossi, F. Roncarolo, S. Ramberger, U. Raich, B. Puccio, D. Nisbet, R. Mompo, S. Mathot, C. Martin, L. A. Lopez-Hernandez, A. Lombardi, J. Lettry, J. B. Lallement, I. Kozsar, J. Hansen, F. Gerigk, A. Funken, J. F. Fuchs, N. Dos Santos, M. Calviani, M. Buzio, O. Brunner, Y. Body, P. Baudrenghien, J. Bauche and T. Zickler, „Linac4 design report", CERN, Geneva, Tech. Rep., 2020. DOI: 10.23731/CYRM-2020-006.

[5] K. H. Reich, „The CERN Proton Synchrotron Booster", *IEEE Transactions on Nuclear Science*, vol. 16, no. 3, pp. 959–961, Jun. 1969, ISSN: 0018-9499, 1558-1578. DOI: 10.1109/TNS.1969.4325414.

[6] G. Brianti, „The CERN synchrotrons", 1997. DOI: 10.5170/CERN-1997-004.29. [Online]. Available: https://cds.cern.ch/record/340514.

[7] L. A. Dyks, D. Posthuma de Boer, A. Ross, M. Backhouse, S. Alden, G. L. D' Alessandro and D. Harryman, „The Superconducting Super Proton Synchrotron", Tech. Rep. DOI: 10.17181/CERN.3DI5.3YUS. [Online]. Available: https://cds.cern.ch/record/2681200.

[8] CMS Collaboration, „Observation of a new boson at a mass of 125 GeV with the CMS experiment at the LHC", *Physics Letters B*, vol. 716, no. 1, pp. 30–61, Sep. 2012, ISSN: 0370-2693. DOI: 10.1016/j.physletb.2012.08.021.

[9] ATLAS Collaboration, „Observation of a new particle in the search for the Standard Model Higgs boson with the ATLAS detector at the LHC", *Physics Letters B*, vol. 716, no. 1, pp. 1–29, Sep. 2012, ISSN: 0370-2693. DOI: 10.1016/j.physletb.2012.08.020.

[10] F. Landua, *The CERN accelerator complex layout in 2022*. 2022, Journal Abbreviation: CERN accelerators. [Online]. Available: https://cds.cern.ch/record/2813716.

[11] CMS Collaboration, „The CMS experiment at the CERN LHC", *Journal of Instrumentation*, vol. 3, no. 08, S08004, Aug. 2008, ISSN: 1748-0221. DOI: 10.1088/1748-0221/3/08/S08004.

[12] T. Sakuma, *Cutaway diagrams of CMS detector*, 2019. DOI: 10.1088/1742-6596/513/2/022032. [Online]. Available: https://cds.cern.ch/record/2665537.

[13] S. R. Davis, *Interactive Slice of the CMS detector*, CMS-OUTREACH-2016-027, 2016. [Online]. Available: https://cds.cern.ch/record/2205172.

[14] S. Cittolin, A. Rácz and P. Sphicas, *CMS The TriDAS Project: Technical Design Report, Volume 2: Data Acquisition and High-Level Trigger*, ser. Technical design report. CMS. Geneva: CERN, 2002. [Online]. Available: https://cds.cern.ch/record/578006.

[15] G. Oliver, „Using Flex in High-Speed Applications", *The PCB Magazine*, Mar. 2014.

[16] Kingfisher International, *Optical Loss & Testing Overview*. [Online]. Available: https://kingfisherfiber.com/application-notes/optical-loss-testing-overview/ (visited on 07/02/2023).

[17] L. Amaral, S. Dris, A. Gerardin, T. Huffman, C. Issever, A. J. Pacheco, M. Jones, S. Kwan, S. .-C. Lee, Z. Liang, T. Liu, Z. Meng, A. Prosser, S. Padadopoulos, I. Papakonstanstinou, C. Sigaud, S. Silva, C. Soos, P. Stejskal, J. Troska, F. Vasey, P. Vichoudis, T. Weidberg, A. Xiang and J. Ye, „The versatile link, a common project for super-LHC", *Journal of Instrumentation*, vol. 4, no. 12, P12003–P12003, Dec. 2009, ISSN: 1748-0221. DOI: 10.1088/1748-0221/4/12/P12003.

[18] F. Vasey, D. Hall, T. Huffman, S. Kwan, A. Prosser, C. Soos, J. Troska, T. Weidberg, A. Xiang and J. Ye, „The Versatile Link common project: feasibility report", *Journal of Instrumentation*, vol. 7, no. 01, p. C01075, Jan. 2012, ISSN: 1748-0221. DOI: 10.1088/1748-0221/7/01/C01075.

[19] L. Olanterä, S. Détraz, A. Kraxner, C. Scarcella, C. Sigaud, C. Soos, J. Troska and F. Vasey, „Radiation Hard Optical Link Developments at CERN", in *2017 17th European Conference on Radiation and Its Effects on Components and Systems (RADECS)*, ISSN: 1609-0438, Oct. 2017, pp. 1–6. DOI: 10.1109/RADECS.2017.8696160.

[20] J. Troska, S. S. E. Nasr-Storey, S. Détraz, L. Olanterä, P. Stejskal, C. Sigaud, C. Soós and F. Vasey, „Laser and photodiode environmental evaluation for the Versatile Link project", *Journal of Instrumentation*, vol. 8, no. 02, pp. C02053–C02053, Feb. 2013, ISSN: 1748-0221. DOI: 10.1088/1748-0221/8/02/C02053.

[21] F. Vasey, „The Versatile Link Application Note", Nov. 2015.

[22] P. Moreira, A. Marchioro and Kloukinas, „The GBT: A proposed architecure for multi-Gb/s data transmission in high energy physics", *Proceedings of the Topical Workshop on Electronics for Particle Physics,*, pp. 332–336, 2007. DOI: 10.5170/CERN-2007-007.332.

[23] CERN, *High Luminosity LHC Project*. [Online]. Available: https://hilumilhc.web.cern.ch/content/hl-lhc-project (visited on 15/01/2023).

[24] CMS Collaboration, *Technical proposal for the upgrade of the CMS detector through 2020*, ser. Technical proposal. 2011, ISBN: 978-92-9083-362-8.

[25] CMS Collaboration, *CMS Technical Design Report for the Phase 1 Upgrade of the Hadron Calorimeter*, ser. Technical design report. CMS 10. 2012, ISBN: 978-92-9083-381-9.

[26] CMS Collaboration, *CMS Technical Design Report for the Pixel Detector Upgrade*, ser. Technical design report. CMS 11. 2012, ISBN: 978-92-9083-380-2.

[27] CMS Collaboration, *CMS Technical Design Report for the Level-1 Trigger Upgrade*, ser. Technical design report. CMS 12. 2013, ISBN: 978-92-9083-390-1.

[28] CMS Collaboration, *Technical Proposal for the Phase-II Upgrade of the CMS Detector*, ser. Technical proposal 15.2. CERN, 2015, ISBN: 978-92-9083-416-8.

[29] CMS Collaboration, *The Phase-2 Upgrade of the CMS Tracker*, ser. Technical design report. CMS. 2017.

[30] CMS Collaboration, *The Phase-2 Upgrade of the CMS Endcap Calorimeter*, ser. Technical design report. CMS. 2017, ISBN: 978-92-9083-459-5.

[31] CMS Collaboration, *A MIP Timing Detector for the CMS Phase-2 Upgrade*, ser. Technical design report. CMS. 2019, ISBN: 978-92-9083-523-3.

[32] CMS Collaboration, *The Phase-2 Upgrade of the CMS Beam Radiation Instrumentation and Luminosity Detectors*, ser. Technical design report. CMS. 2021.

[33] M. Aleksa, J. Blomer, B. Cure, M. Campbell, C. D'Ambrosio, D. Dannheim, M. Doser, F. Faccio, P. Farthouat, C. Gargiulo, P. Janot, C. Joram, M. Krammer, L. Linssen, P. Mato Vila, P. Rodrigues Simoes Moreira, L. Musa, E. Oliveri, A. Onnela, H. Pernegger, P. Riedler, C. Rembser, G. Stewart, H. Ten Kate and F. Vasey, „Strategic R&D Programme on Technologies for Future Experiments", CERN, Geneva, Tech. Rep., 2018. DOI: 10.17181/CERN.5PQI.KDL2.

[34] G. Battistoni, T. Boehlen, F. Cerutti, P. W. Chin, L. S. Esposito, A. Fassò, A. Ferrari, A. Lechner, A. Empl, A. Mairani, A. Mereghetti, P. G. Ortega, J. Ranft, S. Roesler, P. R. Sala, V. Vlachoudis and G. Smirnov, „Overview of the FLUKA code", *Annals of Nuclear Energy*, vol. 82, pp. 10–18, Aug. 2015, ISSN: 0306-4549. DOI: 10.1016/j.anucene.2014.11.007.

[35] T. T. Böhlen, F. Cerutti, M. P. W. Chin, A. Fassò, A. Ferrari, P. G. Ortega, A. Mairani, P. R. Sala, G. Smirnov and V. Vlachoudis, „The FLUKA Code: Developments and Challenges for High Energy and Medical Applications", *Nuclear Data Sheets*, vol. 120, pp. 211–214, Jun. 2014, ISSN: 0090-3752. DOI: 10.1016/j.nds.2014.07.049.

[36] CMS Collaboration, *CMS FLUKA Study V.1.0.0.0*. [Online]. Available: https://twiki.cern.ch/twiki/bin/view/CMSPublic/FLUKAstudyV1000 (visited on 26/01/2023).

[37] C. Soós, S. Détraz, L. Olanterä, C. Sigaud, J. Troska, F. Vasey and M. Zeiler, „Versatile Link PLUS transceiver development", *Journal of Instrumentation*, vol. 12, no. 03, pp. C03068–C03068, Mar. 2017, ISSN: 1748-0221. DOI: 10.1088/1748-0221/12/03/C03068.

[38] C. Soos, F. L. Bottom, S. Detraz, A. Kraxner, L. Olantera, C. Scarcella, C. Sigaud, J. Troska and F. Vasey, „Thermal Characterisation of the Versatile Link+ Transceiver", in *Proceedings of Topical Workshop on Electronics for Particle Physics — PoS(TWEPP2018)*, Antwerp, Belgium, May 2019, p. 060. DOI: 10.22323/1.343.0060.

[39] J. Troska, A. Brandon-Bravo, S. Detraz, A. Kraxner, L. Olantera, C. Scarcella, C. Sigaud, C. Soos and F. Vasey, „The VTRx+, an Optical Link Module for Data Transmission at HL-LHC", in *Proceedings of Topical Workshop on Electronics for Particle Physics — PoS(TWEPP-17)*, Santa Cruz, California, Mar. 2018, p. 048. DOI: 10.22323/1.313.0048.

[40] P. Moreira, „The LpGBT Project, Status and Overview", *ACES 2016 - Fifth Common ATLAS CMS Electronics Workshop for LHC Upgrades*, Mar. 2016.

[41] L. Olantera, J. Blanc, S. Detraz, A. Fetzer, A. Kraxner, C. Scarcella, C. Sigaud, C. Soos, J. Troska, F. Vasey, P. Gui, L. Fang, A. Prosser and A. Weidberg, „Versatile Link+ Transceiver Production Readiness", in *Proceedings of Topical Workshop on Electronics for Particle Physics — PoS(TWEPP2019)*, Santiago de Compostela - Spain, Mar. 2020, p. 055. DOI: 10.22323/1.370.0055.

[42] S. Orfanelli, „The CMS Inner Tracker electronics system development", *Journal of Instrumentation*, vol. 17, no. 08, p. C08003, Aug. 2022, ISSN: 1748-0221. DOI: 10.1088/1748-0221/17/08/C08003.

[43] G. Lutz, „Silicon radiation detectors", *Nucl. Instrum. Meth. A*, vol. 367, pp. 21–33, 1995. DOI: 10.1016/0168-9002(95)00791-1.

[44] A. Heggelund, S. Huiberts, O. Dorholt, A. Read, O. Rohne, H. Sandaker, M. Lauritzen, B. Stugu, A. Kok, O. Koybasi, M. Povoli, M. Bomben, J. Lange and A. Rummler, „Radiation hard 3D silicon pixel sensors for use in the ATLAS detector at the HL-LHC", *Journal of Instrumentation*, vol. 17, no. 08, P08003, Aug. 2022, ISSN: 1748-0221. DOI: 10.1088/1748-0221/17/08/P08003.

[45] S. Seidel, „Silicon strip and pixel detectors for particle physics experiments", *Physics Reports*, vol. 828, pp. 1–34, 2019, Silicon strip and pixel detectors for particle physics experiments, ISSN: 0370-1573. DOI: 10.1016/j.physrep.2019.09.003.

[46] M. Streshinsky, R. Ding, Y. Liu, A. Novack, C. Galland, A. E.-J. Lim, P. G.-Q. Lo, T. Baehr-Jones and M. Hochberg, „The Road to Affordable, Large-Scale Silicon Photonics", *Optics and Photonics News*, vol. 24, no. 9, pp. 32–39, Sep. 2013, ISSN: 1541-3721. DOI: 10.1364/OPN.24.9.000032.

[47] N. Margalit, C. Xiang, S. M. Bowers, A. Bjorlin, R. Blum and J. E. Bowers, „Perspective on the future of silicon photonics and electronics", *Applied Physics Letters*, vol. 118, no. 22, p. 220 501, May 2021, ISSN: 0003-6951, 1077-3118. DOI: 10.1063/5.0050117.

[48] D. Patterson, I. D. Sousa and L.-M. Achard, „The future of packaging with silicon photonics", *Chip Scale Review*, 2017.

[49] M. Streshinsky, R. Ding, Y. Liu, A. Novack, Y. Yang, Y. Ma, X. Tu, E. K. S. Chee, A. E.-J. Lim, P. G.-Q. Lo, T. Baehr-Jones and M. Hochberg, „Low power 50 Gb/s silicon traveling wave Mach-Zehnder modulator near 1300 nm", *Optics Express*, vol. 21, no. 25, pp. 30 350–30 357, Dec. 2013, ISSN: 1094-4087. DOI: 10.1364/OE.21.030350.

[50] J. M. Fedeli, R. Orobtchouk, C. Seassal and L. Vivien, „Integration issues of a photonic layer on top of a CMOS circuit", in *Proceedings of SPIE - The International Society for Optical Engineering*, vol. 6125, 2006, 61250H. DOI: 10.1117/12.642672.

[51] C. Kopp, S. Bernabé, B. B. Bakir, J.-M. Fedeli, R. Orobtchouk, F. Schrank, H. Porte, L. Zimmermann and T. Tekin, „Silicon Photonic Circuits: On-CMOS Integration, Fiber Optical Coupling, and Packaging", *IEEE Journal of Selected Topics in Quantum Electronics*, vol. 17, no. 3, pp. 498–509, May 2011, Conference Name: IEEE Journal of Selected Topics in Quantum Electronics, ISSN: 1558-4542. DOI: 10.1109/JSTQE.2010.2071855.

[52] C. Scarcella, S. Detraz, M. Lalović, L. Marcon, L. Olanterä, T. Prousalidi, U. Sandven, C. Sigaud, C. Soós and J. Troska, „System development of silicon photonics links for CERN experiments and accelerators", *Journal of Instrumentation*, vol. 18, no. 03, p. C03002, Mar. 2023, Publisher: IOP Publishing, ISSN: 1748-0221. DOI: 10.1088/1748-0221/18/03/C03002.

[53] S. L. Partridge, „Silicon-on-insulator technology", *IEEE Proceedings (Computers and Digital Techniques)*, vol. 133, no. 3, pp. 106–116, May 1986, ISSN: 2053-7948. DOI: 10.1049/ip-e.1986.0014.

[54] J.-P. Colinge, *Silicon-on-Insulator Technology: Materials to VLSI*. 2012, ISBN: 978-1-4419-9106-5. DOI: 10.1007/978-1-4419-9106-5.

[55] R. Soref and J. Larenzo, „All-silicon active and passive guided-wave components for 1.3 and 1.6 μm", *IEEE Journal of Quantum Electronics*, vol. 22, no. 6, pp. 873–879, Jun. 1986, ISSN: 1558-1713. DOI: 10.1109/JQE.1986.1073057.

[56] K. Asakawa, Y. Sugimoto and S. Nakamura, „Silicon photonics for telecom and data-com applications", en, *Opto-Electronic Advances*, vol. 3, no. 10, pp. 20 001 101–20 001 126, 2020, ISSN: 2096-4579. DOI: 10.29026/oea.2020.200011.

[57] C. Doerr, „Silicon photonic integration in telecommunications", *Frontiers in Physics*, vol. 3, 2015, ISSN: 2296-424X. [Online]. Available: https://www.frontiersin.org/articles/10.3389/fphy.2015.00037 (visited on 16/02/2023).

[58] K. Yamada, T. Tsuchizawa, H. Nishi, R. Kou, T. Hiraki, K. Takeda, H. Fukuda, Y. Ishikawa, K. Wada and T. Yamamoto, „High-performance silicon photonics technology for telecommunications applications", *Science and Technology of Advanced Materials*, vol. 15, no. 2, p. 024 603, Apr. 2014, ISSN: 1468-6996. DOI: 10.1088/1468-6996/15/2/024603.

[59] Z. Zhou, R. Chen, X. Li and T. Li, „Development trends in silicon photonics for data centers", *Optical Fiber Technology*, vol. 44, pp. 13–23, Aug. 2018, ISSN: 1068-5200. DOI: 10.1016/j.yofte.2018.03.009.

[60] S. Bernabé, Q. Wilmart, K. Hasharoni, K. Hassan, Y. Thonnart, P. Tissier, Y. Désières, S. Olivier, T. Tekin and B. Szelag, „Silicon photonics for terabit/s communication in data centers and exascale computers", *Solid-State Electronics*, vol. 179, p. 107 928, May 2021, ISSN: 0038-1101. DOI: 10.1016/j.sse.2020.107928.

[61] T. Rudolph, „Why I am optimistic about the silicon-photonic route to quantum computing", *APL Photonics*, vol. 2, no. 3, p. 030 901, Mar. 2017, ISSN: 2378-0967. DOI: 10.1063/1.4976737.

[62] J. Wang, F. Sciarrino, A. Laing and M. G. Thompson, „Integrated photonic quantum technologies", *Nature Photonics*, vol. 14, no. 5, pp. 273–284, May 2020, ISSN: 1749-4893. DOI: 10.1038/s41566-019-0532-1.

[63] G.-D. Kim, H.-S. Lee, C.-H. Park, S.-S. Lee, B. T. Lim, H. K. Bae and W.-G. Lee, „Silicon photonic temperature sensor employing a ring resonator manufactured using a standard CMOS process", *Optics Express*, vol. 18, no. 21, pp. 22 215–22 221, Oct. 2010, ISSN: 1094-4087. DOI: 10.1364/OE.18.022215.

[64] L. Chrostowski, S. Grist, J. Flueckiger, W. Shi, X. Wang, E. Ouellet, H. Yun, M. Webb, B. Nie, Z. Liang, K. C. Cheung, S. A. Schmidt, D. M. Ratner and N. A. F. Jaeger, „Silicon photonic resonator sensors and devices", in *Laser Resonators, Microresonators, and Beam Control XIV*, vol. 8236, SPIE, Feb. 2012, pp. 387–402. DOI: 10.1117/12.916860.

[65] E. Luan, H. Shoman, D. M. Ratner, K. C. Cheung and L. Chrostowski, „Silicon Photonic Biosensors Using Label-Free Detection", *Sensors*, vol. 18, no. 10, p. 3519, Oct. 2018, ISSN: 1424-8220. DOI: 10.3390/s18103519.

[66] E. Luan, „Improving the performance of silicon photonic optical resonator-based sensors for biomedical applications", Ph.D. dissertation, University of British Columbia, 2020. DOI: 10.14288/1.0389559.

[67] T. Fukui, Y. Kohno, R. Tang, Y. Nakano and T. Tanemura, „Single-Pixel Imaging Using Multimode Fiber and Silicon Photonic Phased Array", *Journal of Lightwave Technology*, vol. 39, no. 3, pp. 839–844, Feb. 2021, ISSN: 1558-2213. DOI: 10.1109/JLT.2020.3008968.

[68] C. Rogers, A. Y. Piggott, D. J. Thomson, R. F. Wiser, I. E. Opris, S. A. Fortune, A. J. Compston, A. Gondarenko, F. Meng, X. Chen, G. T. Reed and R. Nicolaescu, „A universal 3D imaging sensor on a silicon photonics platform", *Nature*, vol. 590, no. 7845, pp. 256–261, Feb. 2021, ISSN: 1476-4687. DOI: 10.1038/s41586-021-03259-y.

[69] A. L. Lentine, C. T. DeRose, P. S. Davids, N. J. D. Martinez, W. A. Zortman, J. A. Cox, A. Jones, D. C. Trotter, A. T. Pomerene, A. L. Starbuck, D. J. Savignon, T. Bauer, M. Wiwi and P. B. Chu, „Silicon photonics platform for national security applications", in *2015 IEEE Aerospace Conference*, Mar. 2015, pp. 1–9. DOI: 10.1109/AERO.2015.7119249.

[70] J. K. Doylend and S. Gupta, „An overview of silicon photonics for LIDAR", in *Silicon Photonics XV*, vol. 11285, SPIE, Feb. 2020, pp. 109–115. DOI: 10.1117/12.2544962.

[71] C. V. Poulton, A. Yaacobi, D. B. Cole, M. J. Byrd, M. Raval, D. Vermeulen and M. R. Watts, „Coherent solid-state LIDAR with silicon photonic optical phased arrays", *Optics Letters*, vol. 42, no. 20, pp. 4091–4094, Oct. 2017, ISSN: 1539-4794. DOI: 10.1364/OL.42.004091.

[72] R. G. Hunsperger, *Integrated Optics*. New York, NY: Springer New York, 2009, ISBN: 978-0-387-89774-5. DOI: 10.1007/b98730.

[73] S. Pathak, „Chapter 7 - Photonics Integrated Circuits", in *Nanoelectronics*, ser. Advanced Nanomaterials, Elsevier, Jan. 2019, pp. 219–270, ISBN: 978-0-12-813353-8. DOI: 10.1016/B978-0-12-813353-8.00008-7.

[74] A. Snyder and W. Young, „Modes of optical waveguides", *Journal of The Optical Society of America*, vol. 68, pp. 297–309, Mar. 1978. DOI: 10.1364/JOSA.68.000297.

[75] K. K. Lee, D. R. Lim, L. C. Kimerling, J. Shin and F. Cerrina, „Fabrication of ultralow-loss Si/SiO_2 waveguides by roughness reduction", *Optics Letters*, vol. 26, no. 23, p. 1888, Dec. 2001, ISSN: 0146-9592, 1539-4794. DOI: 10.1364/OL.26.001888.

[76] F. Grillot, L. Vivien, S. Laval, D. Pascal and E. Cassan, „Size influence on the propagation loss induced by sidewall roughness in ultrasmall SOI waveguides", *IEEE Photonics Technology Letters*, vol. 16, no. 7, pp. 1661–1663, Jul. 2004, ISSN: 1941-0174. DOI: 10.1109/LPT.2004.828497.

[77] S. Laval, E. Cassan, L. Vivien and F. Grillot, „Influence of waveguide geometry on scattering loss effects in submicron strip silicon-on-insulator waveguides", *IET Optoelectronics*, vol. 2, no. 1, pp. 1–5, Feb. 2008, ISSN: 1751-8768, 1751-8776. DOI: 10.1049/iet-opt:20070001.

[78] Y. A. Vlasov and S. J. McNab, „Losses in single-mode silicon-on-insulator strip waveguides and bends", *Optics Express*, vol. 12, no. 8, p. 1622, 2004, ISSN: 1094-4087. DOI: 10.1364/OPEX.12.001622.

[79] L. Cheng, S. Mao, Z. Li, Y. Han and H. Fu, „Grating Couplers on Silicon Photonics: Design Principles, Emerging Trends and Practical Issues", *Micromachines*, vol. 11, no. 7, p. 666, Jul. 2020, ISSN: 2072-666X. DOI: 10.3390/mi11070666.

[80] W. Bogaerts and D. Vermeulen, „Off-Chip Coupling", in *Handbook of Silicon Photonics*, vol. 20130577, Apr. 2013, pp. 97–138, ISBN: 978-1-4398-3610-1. DOI: 10.1201/b14668-4.

[81] R. Soref and B. Bennett, „Electrooptical effects in silicon", *IEEE Journal of Quantum Electronics*, vol. 23, no. 1, Jan. 1987, Conference Name: IEEE Journal of Quantum Electronics, ISSN: 1558-1713. DOI: 10.1109/JQE.1987.1073206.

[82] L. Vivien and L. Pavesi, *Handbook of Silicon Photonics*, ser. Series in Optics and Optoelectronics. Taylor & Francis, 2013, ISBN: 978-1-4398-3610-1.

[83] H. H. Li, „Refractive index of silicon and germanium and its wavelength and temperature derivatives", *Journal of Physical and Chemical Reference Data*, vol. 9, no. 3, pp. 561–658, Jul. 1980, ISSN: 0047-2689, 1529-7845. DOI: 10.1063/1.555624.

[84] E. Kasper and J. Yu, Eds., *Silicon-Based Photonics*. New York: Jenny Stanford Publishing, Nov. 2020, ISBN: 978-1-315-15651-4. DOI: 10.1201/9781315156514.

[85] S. Liu, J. Feng, Y. Tian, H. Zhao, L. Jin, B. Ouyang, J. Zhu and J. Guo, „Thermo-optic phase shifters based on silicon-on-insulator platform: state-of-the-art and a review", *Frontiers of Optoelectronics*, vol. 15, no. 1, p. 9, Dec. 2022, ISSN: 2095-2759, 2095-2767. DOI: 10.1007/s12200-022-00012-9.

[86] S. Chung, M. Nakai and H. Hashemi, „Low-power thermo-optic silicon modulator for large-scale photonic integrated systems", *Optics Express*, vol. 27, no. 9, p. 13 430, Apr. 2019, ISSN: 1094-4087. DOI: 10.1364/OE.27.013430.

[87] H. C. Huang and T. C. Lo, „Simulation and analysis of silicon electro-optic modulators utilizing the carrier-dispersion effect and impact-ionization mechanism", *Journal of Applied Physics*, vol. 74, no. 3, pp. 1521–1528, Aug. 1993, Publisher: American Institute of Physics, ISSN: 0021-8979. DOI: 10.1063/1.354851.

[88] G. T. Reed and C. Jason Png, „Silicon optical modulators", *Materials Today*, vol. 8, no. 1, pp. 40–50, Jan. 2005, ISSN: 13697021. DOI: 10.1016/S1369-7021(04)00678-9.

[89] N. Pendam and C. P. Vardhani, „Design of optical Mach–Zehnder interferometer phase shifter in silicon-on-insulator", *Pramana*, vol. 92, no. 3, p. 30, Mar. 2019, ISSN: 0304-4289, 0973-7111. DOI: 10.1007/s12043-018-1703-1.

[90] G. T. Reed, D. J. Thomson, F. Y. Gardes, Y. Hu, J.-M. Fedeli and G. Z. Mashanovich, „High-speed carrier-depletion silicon Mach-Zehnder optical modulators with lateral PN junctions", *Frontiers in Physics*, vol. 2, 2014, ISSN: 2296-424X. DOI: 10.3389/fphy.2014.00077.

[91] *Integrated Ring Resonators*, ser. Springer Series in Optical Sciences. Springer, 2007, vol. 127, ISBN: 978-3-540-68786-3. DOI: 10.1007/978-3-540-68788-7.

[92] J. Gamba, „The Role of Transport Phenomena in Whispering Gallery Mode Optical Biosensor Performance", PhD Thesis, California Institute of Technology, Pasadena, California, 2011.

[93] H. Ye and J. Yu, „Germanium epitaxy on silicon", *Science and Technology of Advanced Materials*, vol. 15, no. 2, p. 024 601, Mar. 2014, ISSN: 1468-6996. DOI: 10.1088/1468-6996/15/2/024601.

[94] V. Reboud, A. Gassenq, J. Hartmann, J. Widiez, L. Virot, J. Aubin, K. Guilloy, S. Tardif, J. Fédéli, N. Pauc, A. Chelnokov and V. Calvo, „Germanium based photonic components toward a full silicon/germanium photonic platform", *Progress in Crystal Growth and Characterization of Materials*, vol. 63, no. 2, pp. 1–24, Jun. 2017, ISSN: 09608974. DOI: 10.1016/j.pcrysgrow.2017.04.004.

[95] T.-Y. Liow, K.-W. Ang, Q. Fang, J.-F. Song, Y.-Z. Xiong, M.-B. Yu, G.-Q. Lo and D.-L. Kwong, „Silicon Modulators and Germanium Photodetectors on SOI: Monolithic Integration, Compatibility, and Performance Optimization", *IEEE Journal of Selected Topics in Quantum Electronics*, vol. 16, no. 1, pp. 307–315, Jan. 2010, ISSN: 1558-4542. DOI: 10.1109/JSTQE.2009.2028657.

[96] L. Colace and G. Assanto, „Germanium on Silicon for Near-Infrared Light Sensing", *IEEE Photonics Journal*, vol. 1, no. 2, pp. 69–79, Aug. 2009, ISSN: 1943-0655. DOI: 10.1109/JPHOT.2009.2025516.

[97] Y. Ishikawa, J. Osaka and K. Wada, „Germanium photodetectors in silicon photonics", in *2009 IEEE LEOS Annual Meeting Conference Proceedings*, ISSN: 1092-8081, Oct. 2009, pp. 367–368. DOI: 10.1109/LEOS.2009.5343099.

[98] N.-N. Feng, P. Dong, D. Zheng, S. Liao, H. Liang, R. Shafiiha, D. Feng, G. Li, J. E. Cunningham, A. V. Krishnamoorthy and M. Asghari, „Vertical p-i-n germanium photodetector with high external responsivity integrated with large core Si waveguides", *Optics Express*, vol. 18, no. 1, p. 96, Jan. 2010, ISSN: 1094-4087. DOI: 10.1364/OE.18.000096.

[99] G. Dehlinger, S. Koester, J. Schaub, J. Chu, Q. Ouyang and A. Grill, „High-speed Germanium-on-SOI lateral PIN photodiodes", *IEEE Photonics Technology Letters*, vol. 16, no. 11, pp. 2547–2549, Nov. 2004, Conference Name: IEEE Photonics Technology Letters, ISSN: 1941-0174. DOI: 10.1109/LPT.2004.835631.

[100] C. Claeys and E. Simoen, *Radiation Effects in Advanced Semiconductor Materials and Devices*, R. M. Osgood, R. Hull and J. Parisi, Eds. Springer Berlin Heidelberg, 2002, vol. 57, ISBN: 978-3-642-07778-4. DOI: 10.1007/978-3-662-04974-7.

[101] T. Turflinger, „Single-event effects in analog and mixed-signal integrated circuits", *IEEE Transactions on Nuclear Science*, vol. 43, no. 2, pp. 594–602, Apr. 1996, Conference Name: IEEE Transactions on Nuclear Science, ISSN: 1558-1578. DOI: 10.1109/23.490903.

[102] H. An, D. Li, X. Wen, S. Yang, C. Zhang, J. Wang and Z. Cao, „Experimental Comparison of the Single-Event Effects of Single-Photon and Two-Photon Absorption under a Pulsed Laser", *Applied Sciences*, vol. 12, no. 18, p. 9132, Sep. 2022, ISSN: 2076-3417. DOI: 10.3390/app12189132.

[103] R. Velazco and F. J. Franco, „Single Event Effects on Digital Integrated Circuits: Origins and Mitigation Techniques", in *2007 IEEE International Symposium on Industrial Electronics*, Jun. 2007, pp. 3322–3327. DOI: 10.1109/ISIE.2007.4375148.

[104] L. D. Ryder, K. L. Ryder, A. L. Sternberg, J. A. Kozub, E. X. Zhang, D. Linten, K. Croes, R. A. Weller, R. D. Schrimpf, S. M. Weiss and R. A. Reed, „Single-Event Transient Response of Vertical and Lateral Waveguide-Integrated Germanium Photodiodes", *IEEE Transactions on Nuclear Science*, vol. 68, no. 5, pp. 801–806, May 2021, ISSN: 1558-1578. DOI: 10.1109/TNS.2021.3060349.

[105] G. N. Tzintzarov, A. Ildefonso, J. W. Teng, M. Frounchi, A. Djikeng, P. Iyengar, P. S. Goley, A. Khachatrian, J. Hales, R. Bahr, S. P. Buchner, D. Mcmorrow and J. D. Cressler, „Optical Single-Event Transients Induced in Integrated Silicon-Photonic Waveguides by Two-Photon Absorption", *IEEE Transactions on Nuclear Science*, vol. 68, no. 5, pp. 785–792, May 2021, ISSN: 1558-1578. DOI: 10.1109/TNS.2021.3051802.

[106] R. C. Boggs, E. Richards, L. W. Massengill and T. D. Loveless, „An Electro-Optical Simulation Methodology for the Analysis of Single-Event Radiation Effects in Photonic Devices", en, in *2019 SoutheastCon*, Huntsville, AL, USA: IEEE, Apr. 2019, pp. 1–5, ISBN: 978-1-72810-137-8. DOI: 10.1109/SoutheastCon42311.2019.9020662.

[107] G. Borghello, „Ionizing radiation effects in nanoscale CMOS technologies exposed to ultra-high doses", Ph.D. dissertation, Udine U., 2018. [Online]. Available: https://cds.cern.ch/record/2680840 (visited on 14/11/2023).

[108] J. R. Schwank, „Basic mechanisms of radiation effects in the natural space radiation environment", Jun. 1994. [Online]. Available: https://www.osti.gov/biblio/10158182.

[109] F. McLean and T. Oldham, „Basic Mechanisms of Radiation Effects in Electronic Materials and Devices", Tech. Rep., 1987. [Online]. Available: https://apps.dtic.mil/sti/citations/ADA186936.

[110] M. Bagatin and S. Gerardin, *Ionizing Radiation Effects in Electronics*. CRC Press, 2018, ISBN: 978-1-4987-2263-6.

[111] T. Oldham and F. McLean, „Total ionizing dose effects in MOS oxides and devices", *IEEE Transactions on Nuclear Science*, vol. 50, no. 3, pp. 483–499, Jun. 2003, ISSN: 0018-9499, 1558-1578. DOI: 10.1109/TNS.2003.812927.

[112] H. E. Boesch and F. B. McLean, „Hole Transport and Trapping in Field Oxides", *IEEE Transactions on Nuclear Science*, vol. 32, no. 6, pp. 3940–3945, Dec. 1985, Conference Name: IEEE Transactions on Nuclear Science, ISSN: 1558-1578. DOI: 10.1109/TNS.1985.4334047.

[113] J. R. Schwank, M. R. Shaneyfelt, D. M. Fleetwood, J. A. Felix, P. E. Dodd, P. Paillet and V. Ferlet-Cavrois, „Radiation Effects in MOS Oxides", *IEEE Transactions on Nuclear Science*, vol. 55, no. 4, pp. 1833–1853, Aug. 2008, ISSN: 1558-1578. DOI: 10.1109/TNS.2008.2001040.

[114] D. M. Fleetwood, „Effects of hydrogen transport and reactions on microelectronics radiation response and reliability", *Microelectronics Reliability*, vol. 42, no. 4, pp. 523–541, Apr. 2002, ISSN: 0026-2714. DOI: 10.1016/S0026-2714(02)00019-7.

[115] L. Tsetseris, D. Fleetwood, R. Schrimpf, X. Zhou, I. Batyrev and S. Pantelides, „Hydrogen effects in MOS devices", *Microelectronic Engineering*, vol. 84, no. 9-10, pp. 2344–2349, Sep. 2007, ISSN: 01679317. DOI: 10.1016/j.mee.2007.04.076.

[116] F. B. McLean, „A Framework for Understanding Radiation-Induced Interface States in SiO2 MOS Structures", *IEEE Transactions on Nuclear Science*, vol. 27, no. 6, pp. 1651–1657, Dec. 1980, Conference Name: IEEE Transactions on Nuclear Science, ISSN: 1558-1578. DOI: 10.1109/TNS.1980.4331084.

[117] S. Rashkeev, C. Cirba, D. Fleetwood, R. Schrimpf, S. Witczak, A. Michez and S. Pantelides, „Physical model for enhanced interface-trap formation at low dose rates", *IEEE Transactions on Nuclear Science*, vol. 49, no. 6, pp. 2650–2655, Dec. 2002, Conference Name: IEEE Transactions on Nuclear Science, ISSN: 1558-1578. DOI: 10.1109/TNS.2002.805387.

[118] S. Rashkeev, D. Fleetwood, R. Schrimpf and S. Pantelides, „Proton-induced defect generation at the Si-SiO2 interface", *IEEE Transactions on Nuclear Science*, vol. 48, no. 6, pp. 2086–2092, Dec. 2001, Conference Name: IEEE Transactions on Nuclear Science, ISSN: 1558-1578. DOI: 10.1109/23.983177.

[119] P. M. Lenahan, „What can electron paramagnetic resonance tell us about the Si/SiO2 system?", *Journal of Vacuum Science & Technology B: Microelectronics and Nanometer Structures*, vol. 16, no. 4, p. 2134, Jul. 1998, ISSN: 0734211X. DOI: 10.1116/1.590301.

[120] J. H. Stathis and E. Cartier, „Atomic hydrogen reactions with P b centers at the (100) Si/ SiO 2 interface", *Physical Review Letters*, vol. 72, no. 17, pp. 2745–2748, Apr. 1994, ISSN: 0031-9007. DOI: 10.1103/PhysRevLett.72.2745.

[121] L.-Å. Ragnarsson and P. Lundgren, „Electrical characterization of Pb centers in (100)Si–SiO2 structures: The influence of surface potential on passivation during post metallization anneal", *Journal of Applied Physics*, vol. 88, no. 2, pp. 938–942, Jul. 2000, ISSN: 0021-8979, 1089-7550. DOI: 10.1063/1.373759.

[122] P. Lenahan, N. Bohna and J. Campbell, „Radiation-induced interface traps in MOS devices: capture cross section and density of states of Pb1 silicon dangling bond centers", *IEEE Transactions on Nuclear Science*, vol. 49, no. 6, pp. 2708–2712, Dec. 2002, Conference Name: IEEE Transactions on Nuclear Science, ISSN: 1558-1578. DOI: 10.1109/TNS.2002.805357.

[123] J. P. Campbell and P. M. Lenahan, „Density of states of Pb1 Si/SiO2 interface trap centers", *Applied Physics Letters*, vol. 80, no. 11, pp. 1945–1947, Mar. 2002, ISSN: 0003-6951, 1077-3118. DOI: 10.1063/1.1461053.

[124] V. S. Vavilov, *Effects of Radiation on Semiconductors*. Boston, MA: Springer US, 1965, ISBN: 978-1-4899-2722-4. DOI: 10.1007/978-1-4899-2720-0.

[125] M. L. Reed and J. D. Plummer, „Chemistry of Si-SiO $_2$ interface trap annealing", *Journal of Applied Physics*, vol. 63, no. 12, pp. 5776–5793, Jun. 1988, ISSN: 0021-8979, 1089-7550. DOI: 10.1063/1.340317.

[126] D. Fleetwood, W. Warren, J. Schwank, P. Winokur, M. Shaneyfelt and L. Riewe, „Effects of interface traps and border traps on MOS postirradiation annealing response", *IEEE Transactions on Nuclear Science*, vol. 42, no. 6, pp. 1698–1707, Dec. 1995, ISSN: 1558-1578. DOI: 10.1109/23.488768.

[127] V. Danchenko, U. D. Desai and S. S. Brashears, „Characteristics of Thermal Annealing of Radiation Damage in MOSFET's", *Journal of Applied Physics*, vol. 39, no. 5, pp. 2417–2424, Apr. 1968, ISSN: 0021-8979, 1089-7550. DOI: 10.1063/1.1656570.

[128] D. B. Brown, D. I. Ma, C. M. Dozier and M. C. Peckerar, „Thermal Annealing of Radiation Induced Defects: A Diffusion-Limited Process?", *IEEE Transactions on Nuclear Science*, vol. 30, no. 6, pp. 4059–4063, Dec. 1983, ISSN: 1558-1578. DOI: 10.1109/TNS.1983.4333081.

[129] D. Fleetwood, S. Miller, R. Reber, P. McWhorter, P. Winokur, M. Shaneyfelt and J. Schwank, „New insights into radiation-induced oxide-trap charge through thermally-stimulated-current measurement and analysis (MOS capacitors)", *IEEE Transactions on Nuclear Science*, vol. 39, no. 6, pp. 2192–2203, Dec. 1992, ISSN: 1558-1578. DOI: 10.1109/23.211421.

[130] J. R. Schwank and W. R. Dawes, „Irradiated Silicon Gate MOS Device Bias Annealing", *IEEE Transactions on Nuclear Science*, vol. 30, no. 6, pp. 4100–4104, Dec. 1983, ISSN: 1558-1578. DOI: 10.1109/TNS.1983.4333089.

[131] J. Kroll, P. Allport, A. Chisholm, D. Dudáš, V. Fadeyev, W. George, L. Gonella, I. Kopsalis, J. Kvasnička, V. Latoňová, J. Lomas, F. Martinez-Mckinney, M. Mikeštíková, X. Shi, P. Tůma, M. Ullan and Y. Unno, „Effect of irradiation and annealing performed with bias voltage applied across the coupling capacitors on the interstrip resistance of ATLAS ITk silicon strip sensors", *Nuclear Instruments and Methods in Physics Research Section A: Accelerators, Spectrometers, Detectors and Associated Equipment*, vol. 1047, p. 167 726, Feb. 2023, ISSN: 01689002. DOI: 10.1016/j.nima.2022.167726.

[132] Y. Chen and T. Noguchi, „A laser annealing process for high-performance power MOSFETs", in *2014 International Workshop on Junction Technology (IWJT)*, May 2014, pp. 1–4. DOI: 10.1109/IWJT.2014.6842026.

[133] G. S. Ristić, „Thermal and UV annealing of irradiated pMOS dosimetric transistors", *Journal of Physics D: Applied Physics*, vol. 42, no. 13, p. 135 101, Jun. 2009, ISSN: 0022-3727. DOI: 10.1088/0022-3727/42/13/135101.

[134] S. Seif El Nasr-Storey, F. Boeuf, C. Baudot, S. Detraz, J. M. Fedeli, D. Marris-Morini, L. Olantera, G. Pezzullo, C. Sigaud, C. Soos, J. Troska, F. Vasey, L. Vivien, M. Zeiler and M. Ziebell, „Modeling TID Effects in Mach-Zehnder Interferometer Silicon Modulator for HL-LHC Data Transmission Applications", *IEEE Transactions on Nuclear Science*, vol. 62, no. 6, pp. 2971–2978, Dec. 2015, ISSN: 1558-1578. DOI: 10.1109/TNS.2015.2499041.

[135] K. Nordlund, S. J. Zinkle, A. E. Sand, F. Granberg, R. S. Averback, R. E. Stoller, T. Suzudo, L. Malerba, F. Banhart, W. J. Weber, F. Willaime, S. L. Dudarev and D. Simeone, „Primary radiation damage: A review of current understanding and models", *Journal of Nuclear Materials*, vol. 512, pp. 450–479, Dec. 2018, ISSN: 00223115. DOI: 10.1016/j.jnucmat.2018.10.027.

[136] H. Spieler, *Semiconductor Detector Systems*. Oxford: Claredon Press, 2005.

[137] J. Srour and J. McGarrity, „Radiation effects on microelectronics in space", *Proceedings of the IEEE*, vol. 76, no. 11, pp. 1443–1469, Nov. 1988, Conference Name: Proceedings of the IEEE, ISSN: 1558-2256. DOI: 10.1109/5.90114.

[138] M. Huhtinen, „Simulation of non-ionising energy loss and defect formation in silicon", *Nuclear Instruments and Methods in Physics Research Section A: Accelerators, Spectrometers, Detectors and Associated Equipment*, vol. 491, no. 1-2, pp. 194–215, Sep. 2002, ISSN: 01689002. DOI: 10.1016/S0168-9002(02)01227-5.

[139] G. N. Taylor, F. Fares, S. J. Bates, C. Furetta, M. Glaser, F. Lemeilleur, E. Leon-Florian, C. Gößling, B. Kaiser, A. Rolf, R. Wunstorf, H. Feick, E. Fretwurst, G. Lindström, M. Moll and A. Chilingarov, „Radiation induced bulk damage in silicon detectors", *Nuclear Instruments and Methods in Physics Research Section A: Accelerators, Spectrometers, Detectors and Associated Equipment*, Development and Application of Semiconductor Tracking Detectors, vol. 383, no. 1, pp. 144–154, Dec. 1996, ISSN: 0168-9002. DOI: 10.1016/S0168-9002(96)00668-7.

[140] C. J. Dale, P. W. Marshall, G. P. Summers, E. A. Wolicki and E. A. Burke, „Displacement damage equivalent to dose in silicon devices", *Applied Physics Letters*, vol. 54, no. 5, pp. 451–453, Jan. 1989, ISSN: 0003-6951, 1077-3118. DOI: 10.1063/1.100949.

[141] A. Akkerman, J. Barak, M. B. Chadwick, J. Levinson, M. Murat and Y. Lifshitz, „Updated NIEL calculations for estimating the damage induced by particles and gamma-rays in Si and GaAs", *Radiation Physics and Chemistry*, vol. 62, no. 4, pp. 301–310, Oct. 2001, ISSN: 0969-806X. DOI: 10.1016/S0969-806X(01)00207-9.

[142] M. Lazo, D. Woodall and P. McDaniel, „Silicon and Silicon dioxide neutron damage functions", United States, Tech. Rep., 1987, SAND87-0098, pp. 85–104. [Online]. Available: http://inis.iaea.org/search/search.aspx?orig_q=RN:22038475.

[143] ASTM International, *Standard Practice for Characterizing Neutron Fluence Spectra in Terms of an Equivalent Monoenergetic Neutron Fluence for Radiation-Hardness Testing of Electronics*, ASTM E722-85, 1993. DOI: 10.1520/E0722-19. [Online]. Available: https://www.astm.org/e0722-19.html.

[144] M. Moll, „Radiation Damage in Silicon Particle Detectors", PhD Thesis, University of Hamburg, 1999. [Online]. Available: https://mmoll.web.cern.ch/thesis/pdf/moll-thesis.pdf.

[145] *Homepage | EP-ESE Electronic Systems for Experiments*. [Online]. Available: https://ep-ese.web.cern.ch/ (visited on 28/06/2023).

[146] *imec*. [Online]. Available: https://www.imec-int.com/en (visited on 28/06/2023).

[147] M. Zeiler, „Radiation-hard Silicon Photonics for Future High Energy Physics Experiments", PhD Thesis, Dublin City University, Jun. 2017.

[148] M. Zeiler, S. Detraz, L. Olantera, C. Sigaud, C. Soos, J. Troska and F. Vasey, „Comparison of the radiation hardness of silicon Mach-Zehnder modulators for different DC bias voltages", in *2016 IEEE Nuclear Science Symposium, Medical Imaging Conference and Room-Temperature Semiconductor Detector Workshop (NSS/MIC/RTSD)*, Oct. 2016, pp. 1–2. DOI: 10.1109/NSSMIC.2016.8069867.

[149] M. Zeiler, S. Detraz, L. Olantera, S. S. E. Nasr-Storey, C. Sigaud, C. Soos, J. Troska and F. Vasey, „Radiation hardness evaluation and phase shift enhancement through ionizing radiation in silicon Mach-Zehnder modulators", in *2016 16th European Conference on Radiation and Its Effects on Components and Systems (RADECS)*, Sep. 2016, pp. 1–4. DOI: 10.1109/RADECS.2016.8093130.

[150] A. Kraxner, S. Detraz, L. Olantera, C. Scarcella, C. Sigaud, C. Soos, C. Stile, J. Troska and F. Vasey, „Radiation tolerance enhancement of silicon photonics for HEP applications", in *Proceedings of Topical Workshop on Electronics for Particle Physics — PoS(TWEPP2018)*, Antwerp, Belgium: Sissa Medialab, May 2019, p. 150. DOI: 10.22323/1.343.0150.

[151] *Silicon photonic ICs for prototyping and volume production | imec*. [Online]. Available: https://www.imec-int.com/en/silicon-photonic-ICs-prototyping (visited on 05/07/2023).

[152] M. Pantouvaki, S. A. Srinivasan, Y. Ban, P. De Heyn, P. Verheyen, G. Lepage, H. Chen, J. De Coster, N. Golshani, S. Balakrishnan, P. Absil and J. Van Campenhout, „Active Components for 50 Gb/s NRZ-OOK Optical Interconnects in a Silicon Photonics Platform", *Journal of Lightwave Technology*, vol. 35, no. 4, pp. 631–638, Feb. 2017, ISSN: 1558-2213. DOI: 10.1109/JLT.2016.2604839.

[153] M. Zeiler, S. S. El Nasr-Storey, S. Detraz, A. Kraxner, L. Olantera, C. Scarcella, C. Sigaud, C. Soos, J. Troska and F. Vasey, „Radiation Damage in Silicon Photonic Mach–Zehnder Modulators and Photodiodes", *IEEE Transactions on Nuclear Science*, vol. 64, no. 11, pp. 2794–2801, Nov. 2017, ISSN: 0018-9499, 1558-1578. DOI: 10.1109/TNS.2017.2754948.

[154] H. Yu and W. Bogaerts, „An Equivalent Circuit Model of the Traveling Wave Electrode for Carrier-Depletion-Based Silicon Optical Modulators", *Journal of Lightwave Technology*, vol. 30, no. 11, pp. 1602–1609, Jun. 2012, ISSN: 1558-2213. DOI: 10.1109/JLT.2012.2188779.

[155] *Hybrid SA microélectronique, Chez-le-Bart, 2025, Switzerland*. [Online]. Available: https://www.hybrid.swiss/ (visited on 28/07/2023).

[156] P. Dong, R. Shafiiha, S. Liao, H. Liang, N.-N. Feng, D. Feng, G. Li, X. Zheng, A. V. Krishnamoorthy and M. Asghari, „Wavelength-tunable silicon microring modulator", *Optics Express*, vol. 18, no. 11, p. 10 941, May 2010, ISSN: 1094-4087. DOI: 10.1364/OE.18.010941.

[157] *Ansys Lumerical HEAT | 3D Heat Transport Solver*. [Online]. Available: https://www.ansys.com/products/photonics/heat (visited on 06/08/2023).

[158] M. Zeiler, S. Detraz, L. Olantera, G. Pezzullo, S. S. El Nasr-Storey, C. Sigaud, C. Soos, J. Troska and F. Vasey, „Design of Si-photonic structures to evaluate their radiation hardness dependence on design parameters", *Journal of Instrumentation*, vol. 11, no. 01, pp. C01040–C01040, Jan. 2016, ISSN: 1748-0221. DOI: 10.1088/1748-0221/11/01/C01040.

[159] C. T. DeRose, D. C. Trotter, W. A. Zortman, A. L. Starbuck, M. Fisher, M. R. Watts and P. S. Davids, „Ultra compact 45 GHz CMOS compatible Germanium waveguide photodiode with low dark current", *Optics Express*, vol. 19, no. 25, p. 24 897, Dec. 2011, ISSN: 1094-4087. DOI: 10.1364/OE.19.024897.

[160] X. Zhao, G. Wang, H. Lin, Y. Du, X. Luo, Z. Kong, J. Su, J. Li, W. Xiong, Y. Miao, H. Li, G. Guo and H. H. Radamson, „High Performance p-i-n Photodetectors on Ge-on-Insulator Platform", *Nanomaterials*, vol. 11, no. 5, p. 1125, Apr. 2021, ISSN: 2079-4991. DOI: 10.3390/nano11051125.

[161] *EP-ESE irradiation system*. [Online]. Available: https://espace.cern.ch/project-xrayese/_layouts/15/start.aspx#/default.aspx (visited on 28/08/2023).

[162] A. Kraxner, S. Detraz, L. Olantera, C. Scarcella, C. Sigaud, C. Soos, J. Troska and F. Vasey, „Investigation of the Influence of Temperature and Annealing on the Radiation Hardness of Silicon Mach–Zehnder Modulators", *IEEE Transactions on Nuclear Science*, vol. 65, no. 8, pp. 1624–1631, Aug. 2018, ISSN: 0018-9499, 1558-1578. DOI: 10.1109/TNS.2018.2823863.

[163] S. E. Nasr-Storey, S. Détraz, L. Olanterä, C. Sigaud, C. Soós, G. Pezzullo, J. Troska, F. Vasey and M. Zeiler, „Neutron and X-ray irradiation of silicon based Mach-Zehnder modulators", *Journal of Instrumentation*, vol. 10, no. 03, pp. C03040–C03040, Mar. 2015, ISSN: 1748-0221. DOI: 10.1088/1748-0221/10/03/C03040.

[164] S. Seif El Nasr-Storey, F. Boeuf, C. Baudot, S. Detraz, J. M. Fedeli, D. Marris-Morini, L. Olantera, G. Pezzullo, C. Sigaud, C. Soos, J. Troska, F. Vasey, L. Vivien, M. Zeiler and M. Ziebell, „Effect of Radiation on a Mach–Zehnder Interferometer Silicon Modulator for HL-LHC Data Transmission Applications", *IEEE Transactions on Nuclear Science*, vol. 62, no. 1, pp. 329–335, Feb. 2015, ISSN: 1558-1578. DOI: 10.1109/TNS.2015.2388546.

[165] *ObeliX - irradiation system*. [Online]. Available: https://espace.cern.ch/project-xrayese/ObeliX/Forms/AllItems.aspx (visited on 28/08/2023).

[166] *Igor Pro | Igor Pro by WaveMetrics*. [Online]. Available: https://www.wavemetrics.com/products/igorpro (visited on 09/09/2023).

[167] M. Zeiler, S. Detraz, L. Olantera, C. Sigaud, C. Soos, J. Troska and F. Vasey, „A system-level model for high-speed, radiation-hard optical links in HEP experiments based on silicon Mach-Zehnder modulators", *Journal of Instrumentation*, vol. 11, no. 12, pp. C12059–C12059, Dec. 2016, ISSN: 1748-0221. DOI: 10.1088/1748-0221/11/12/C12059.

[168] X. Xiao, H. Xu, X. Li, Z. Li, T. Chu, Y. Yu and J. Yu, „High-speed, low-loss silicon Mach–Zehnder modulators with doping optimization", *Optics Express*, vol. 21, no. 4, p. 4116, Feb. 2013, ISSN: 1094-4087. DOI: 10.1364/OE.21.004116.

[169] G. Borghello, F. Faccio, E. Lerario, S. Michelis, S. Kulis, D. M. Fleetwood, R. D. Schrimpf, S. Gerardin, A. Paccagnella and S. Bonaldo, „Dose-Rate Sensitivity of 65-nm MOSFETs Exposed to Ultrahigh Doses", *IEEE Transactions on Nuclear Science*, vol. 65, no. 8, pp. 1482–1487, Aug. 2018, ISSN: 0018-9499, 1558-1578. DOI: 10.1109/TNS.2018.2828142.

[170] S. Witczak, R. Lacoe, J. Osborn, J. Hutson and S. Moss, „Dose-rate sensitivity of modern nMOSFETs", *IEEE Transactions on Nuclear Science*, vol. 52, no. 6, pp. 2602–2608, Dec. 2005, Conference Name: IEEE Transactions on Nuclear Science, ISSN: 1558-1578. DOI: 10.1109/TNS.2005.860709.

[171] P. S. Goley, G. N. Tzintzarov, S. Zeinolabedinzadeh, A. Ildefonso, K. Motoki, R. Jiang, E. X. Zhang, D. M. Fleetwood, L. Zimmermann, M. Kaynak, S. Lischke, C. Mai and J. D. Cressler, „Total Ionizing Dose Effects in 70-GHz Bandwidth Photodiodes in a SiGe Integrated Photonics Platform", *IEEE Transactions on Nuclear Science*, vol. 66, no. 1, pp. 125–133, Jan. 2019, Conference Name: IEEE Transactions on Nuclear Science, ISSN: 1558-1578. DOI: 10.1109/TNS.2018.2885327.

[172] *Neutron Irradiation Facility (NIF)*. [Online]. Available: https://uclouvain.be/en/research-institutes/irmp/neutron-irradiation-facility-nif.html (visited on 10/12/2023).

[173] *CRC - Cyclotron Resource Centre*. [Online]. Available: https://uclouvain.be/en/research-institutes/irmp/crc.html (visited on 11/12/2023).

[174] G. Gregoire, „Tests of electronic devices and semi-conductor detectors under high neutron flux", *Journal of Physics: Conference Series*, vol. 41, no. 1, p. 21, May 2006, ISSN: 1742-6596. DOI: 10.1088/1742-6596/41/1/002.

[175] J P Meulders, P Leleux, P C Macq and C Pirart, „Fast neutron yields and spectra from targets of varying atomic number bombarded with deuterons from 16 to 50 MeV (for radiobiology and radiotherapy)", *Physics in Medicine & Biology*, vol. 20, no. 2, pp. 235–243, Mar. 1975, ISSN: 0031-9155, 1361-6560. DOI: 10.1088/0031-9155/20/2/005.

[176] G. Berger, *Irradiation Facilities at CYCLONE (HIF – LIF – NIF)*, 6th LHC Radiation Workshop 29-30 November 2007, 2007.

[177] S. S. E. Nasr-Storey, „Radiation-hard Optoelectronics for LHC detector upgrades", PhD Thesis, University of Bristol, Jun. 2016.

[178] M. Menouni, P. Gui and P. Moreira, „The GBTIA, a 5 Gbit/s Radiation-Hard Optical Receiver for the SLHC Upgrades", in *Proceedings of the Topical Workshop on Electronics for Particle Physics,*, 2009, pp. 326–330. DOI: 10.5170/CERN-2009-006.326.

[179] L. Olantera, F. Bottom, A. Kraxner, S. Detraz, M. Menouni, P. Moreira, C. Scarcella, C. Sigaud, C. Soos, J. Troska and F. Vasey, „Radiation Effects on High-Speed InGaAs Photodiodes", *IEEE Transactions on Nuclear Science*, vol. 66, no. 7, pp. 1663–1670, Jul. 2019, ISSN: 0018-9499, 1558-1578. DOI: 10.1109/TNS.2019.2902624.

[180] T. Prousalidi, A. Bulling, M. Court, S. Detraz, M. Lalović, L. Marcon, L. Olanterä, S. Orfanelli, U. Sandven, C. Scarcella, C. Sigaud, C. Soós and J. Troska, „Towards optical data transmission for high energy physics using silicon photonics", *Journal of Instrumentation*, vol. 17, no. 05, p. C05004, May 2022, ISSN: 1748-0221. DOI: 10.1088/1748-0221/17/05/C05004.

[181] T. Prousalidi, C. Scarcella, A. Ahmed, S. Detraz, M. Lalović, L. Olanterä, A. Pandey, C. Sigaud, C. Soós, J. Troska and H. Avramopoulos, „System Development of Radiation-Tolerant Silicon Photonics Transceivers for High Energy Physics Applications", *IEEE Transactions on Nuclear Science*, vol. 70, no. 10, pp. 2373–2380, Oct. 2023, ISSN: 1558-1578. DOI: 10.1109/TNS.2023.3310059.

[182] *Overview | Future Circular Collider*. [Online]. Available: https://fcc.web.cern.ch/overview (visited on 21/01/2024).

Biography

Milana Lalović was born on 31.08.1994. in Sarajevo, Bosnia and Herzegovina. In 2013, she started her studies at the University of Belgrade, School of Electrical Engineering. She graduated in 2017 with a major in Physical Electronics, specialising in Nanoelectronics, Optoelectronics, and Laser Techniques, with an average grade of 8.85. Her bachelor's thesis titled "Realisation of all-optical NOR gate based on injection-locking in laser diodes" was defended on 04.07.2017., under the supervision of Associate Professor Dr. Marko Krstić, with a grade of 10. Milana then pursued master's studies in Nanoelectronics and Photonics at the University of Belgrade, School of Electrical Engineering, starting in October 2017. She excelled in all exams, maintaining an average grade of 10. On 14.09.2018., she defended her master's thesis, "All-optical switches based on cross-phase and gain modulation in semiconductor optical amplifiers," under the supervision of Professor Dr. Jasna Crnjanski. In October 2018, Milana enrolled in doctoral studies in Nanoelectronics and Photonics at the University of Belgrade, School of Electrical Engineering. She successfully completed all required exams and met the obligations outlined in the doctoral studies plan, accumulating the necessary 120 ECTS credits.

As of 01.03.2020, Milana was employed as a doctoral student at the European Organisation for Nuclear Research (CERN) in Switzerland, where she was conducting scientific research in the field of silicon photonics. During her PhD, she presented her work at two international conferences, Radiations Effects on Components and Systems (RADECS21) and Topical Workshop on Electronics for Particle Physics (TWEPP22). Milana has published two papers as the first author in journals of international significance (M20), the IEEE Transactions on Nuclear Science and the Journal of Instrumentation. Additionally, she has contributed as a co-author to six other research papers published in journals of international significance (M20) and two papers published in the proceedings of international scientific conferences (M30).

Изјава о ауторству

Име и презиме аутора Милана Лаловић

Број индекса 5004/2018

Изјављујем

да је докторска дисертација под насловом

Утицаји зрачења на оптичке линкове засноване на силицијумској фотоници

(енг. Radiation effects in silicon photonics optical links)

- резултат сопственог истраживачког рада;
- да дисертација у целини ни у деловима није била предложена за стицање друге дипломе према студијским програмима других високошколских установа;
- да су резултати коректно наведени и
- да нисам кршио/ла ауторска права и користио/ла интелектуалну својину других лица.

Потпис аутора

У Београду, 01.02.2024.

Милана Лаловић

Изјава о истоветности штампане и електронске верзије докторског рада

Име и презиме аутора Милана Лаловић

Број индекса 5004/2018

Студијски програм Електротехника и рачунарство, модул Наноелектроника и фотоника

Наслов рада Утицаји зрачења на оптичке линкове засноване на силицијумској фотоници

Ментор проф. др Пеђа Михаиловић, редовни професор

Изјављујем да је штампана верзија мог докторског рада истоветна електронској верзији коју сам предао/ла ради похрањивања у **Дигиталном репозиторијуму Универзитета у Београду**.

Дозвољавам да се објаве моји лични подаци везани за добијање академског назива доктора наука, као што су име и презиме, година и место рођења и датум одбране рада.

Ови лични подаци могу се објавити на мрежним страницама дигиталне библиотеке, у електронском каталогу и у публикацијама Универзитета у Београду.

Потпис аутора

У Београду, 01.02.2024.

Милана Лаловић

Изјава о коришћењу

Овлашћујем Универзитетску библиотеку „Светозар Марковић“ да у Дигитални репозиторијум Универзитета у Београду унесе моју докторску дисертацију под насловом:

Утицаји зрачења на оптичке линкове засноване на силицијумској фотоници

(енг. Radiation effects in silicon photonics optical links)

која је моје ауторско дело.

Дисертацију са свим прилозима предао/ла сам у електронском формату погодном за трајно архивирање.

Моју докторску дисертацију похрањену у Дигиталном репозиторијуму Универзитета у Београду и доступну у отвореном приступу могу да користе сви који поштују одредбе садржане у одабраном типу лиценце Креативне заједнице (Creative Commons) за коју сам се одлучио/ла.

1. Ауторство (CC BY)

2. Ауторство – некомерцијално (CC BY-NC)

3. Ауторство – некомерцијално – без прерада (CC BY-NC-ND)

4. Ауторство – некомерцијално – делити под истим условима (CC BY-NC-SA)

5. Ауторство – без прерада (CC BY-ND)

6. Ауторство – делити под истим условима (CC BY-SA)

(Молимо да заокружите само једну од шест понуђених лиценци.
Кратак опис лиценци је саставни део ове изјаве).

Потпис аутора

У Београду, 01.02.2024.

Милана Маловић

1. **Ауторство.** Дозвољавате умножавање, дистрибуцију и јавно саопштавање дела, и прераде, ако се наведе име аутора на начин одређен од стране аутора или даваоца лиценце, чак и у комерцијалне сврхе. Ово је најслободнија од свих лиценци.

2. **Ауторство – некомерцијално.** Дозвољавате умножавање, дистрибуцију и јавно саопштавање дела, и прераде, ако се наведе име аутора на начин одређен од стране аутора или даваоца лиценце. Ова лиценца не дозвољава комерцијалну употребу дела.

3. **Ауторство – некомерцијално – без прерада.** Дозвољавате умножавање, дистрибуцију и јавно саопштавање дела, без промена, преобликовања или употребе дела у свом делу, ако се наведе име аутора на начин одређен од стране аутора или даваоца лиценце. Ова лиценца не дозвољава комерцијалну употребу дела. У односу на све остале лиценце, овом лиценцом се ограничава највећи обим права коришћења дела.

4. **Ауторство – некомерцијално – делити под истим условима.** Дозвољавате умножавање, дистрибуцију и јавно саопштавање дела, и прераде, ако се наведе име аутора на начин одређен од стране аутора или даваоца лиценце и ако се прерада дистрибуира под истом или сличном лиценцом. Ова лиценца не дозвољава комерцијалну употребу дела и прерада.

5. **Ауторство – без прерада.** Дозвољавате умножавање, дистрибуцију и јавно саопштавање дела, без промена, преобликовања или употребе дела у свом делу, ако се наведе име аутора на начин одређен од стране аутора или даваоца лиценце. Ова лиценца дозвољава комерцијалну употребу дела.

6. **Ауторство – делити под истим условима.** Дозвољавате умножавање, дистрибуцију и јавно саопштавање дела, и прераде, ако се наведе име аутора на начин одређен од стране аутора или даваоца лиценце и ако се прерада дистрибуира под истом или сличном лиценцом. Ова лиценца дозвољава комерцијалну употребу дела и прерада. Слична је софтверским лиценцама, односно лиценцама отвореног кода.